UC Berkeley
UC Berkeley Electronic Theses and Dissertations

Title
Applications of Magnetic Particle Imaging

Permalink
https://escholarship.org/uc/item/38h1x3zb

Author
Zhou, Xinyi Yedda

Publication Date
2019

Peer reviewed|Thesis/dissertation

eScholarship.org Powered by the California Digital Library
University of California

Applications of Magnetic Particle Imaging

by

Xinyi Yedda Zhou

A dissertation submitted in partial satisfaction of the

requirements for the degree of

Joint Doctor of Philosophy
with University of California, San Francisco

in

Bioengineering

in the

Graduate Division

of the

University of California, Berkeley

Committee in charge:

Professor Steven M. Conolly, Chair
Professor John Clarke
Professor Peder Larson

Summer 2019

Applications of Magnetic Particle Imaging

Copyright 2019
by
Xinyi Yedda Zhou

Abstract

Applications of Magnetic Particle Imaging

by

Xinyi Yedda Zhou

Joint Doctor of Philosophy
with University of California, San Francisco in Bioengineering

University of California, Berkeley

Professor Steven M. Conolly, Chair

Magnetic particle imaging (MPI) is an emerging tracer imaging modality with high sensitivity and ideal image contrast. MPI uses low-frequency magnetic fields to image the spatial distribution of superparamagnetic iron oxide (SPIO) tracers. There is ideal image contrast because background tissue (bone, muscle, blood, fat) produces no MPI signal. Moreover, there is zero depth attenuation of low-frequency magnetic fields in tissue, allowing for quantitative imaging. In this dissertation, I describe several new preclinical imaging applications which take advantage of the unique physics of MPI: lung perfusion imaging, white blood cell tracking, and enzyme-responsive nanocarriers.

Pulmonary embolism (PE), a blood clot in the lung, is usually diagnosed with CT pulmonary angiography. However, patients with poor renal function are not able to tolerate the high iodine dose. The MPI tracer is kidney-safe because it clears through the liver and spleen instead of the kidneys. Moreover, imaging around air-tissue interfaces such as those in the lung do not result in imaging artifacts (unlike in magnetic resonance imaging) because of the comparably low gradient homogeneity needed. Hence, MPI has ideal properties for a kidney-safe alternative lung perfusion imaging method. In Chapter 2, I show fabrication and optimization of the first MPI lung perfusion imaging agent, MAA-SPIO, and *in vivo* lung perfusion images in a rat. I quantitatively track the biodistribution and clearance of the tracer over time. Additionally, I show that the lung perfusion imaging method can be paired with a method for lung ventilation imaging using aerosolized SPIOs. This allows for imaging of both the lung capillaries and lung airways.

In Chapter 3, I discuss MPI white blood cell imaging. This technique is of particular interest for tracking autologous cell-based immunotherapies, such as chimeric antigen receptor T cells (CAR-T). Moreover, the natural homing abilities of the WBCs can localize difficult-to-find infections, such as osteomyelitis, and a similar technique is used in nuclear medicine. However, MPI allows for effective long-term cell tracking because no radionuclide tag is used. I demonstrate dynamic imaging of MPI tracer-tagged white blood cells (WBC)

administered to *in vivo* mice, and initial work on tracking these WBCs in a mouse model of inflammation.

In Chapter 4, I demonstrate proof-of-concept work on a concept for enzyme-responsive nanocarriers. Tracers that can visualize and respond to the function of biological and cellular processes would allow for more specific disease diagnoses. I show that aggregated SPIOs have a quenched MPI signal as compared to stably-dispersed SPIOs, and that SPIOs can be encapsulated in a liposomal formulation. In the platform described, the enzyme hydrolyzes the SPIO-containing liposomes, and MPI signal quenching is observed. These projects represent novel work in diverse categories of MPI applications research, showcasing the strengths of the unique physics of MPI.

To

everyone I have named in my very expansive acknowledgements, but also to all the friends who have been with me every step of the way:
Lunch crew: S.W., S.J., K.W., C.F.
Climbing pals: D.F., J.Y., B.M, S.P.
Housemates: H.L., Y.L., M.W., A.A., Z.W., K.H., P.M.
Ph.D. compatriots from UMD: A.A., H.W., T.R.
Longtime friends: K.Z., R.P., C.Z.
The QG gaggle & BEAST.
The cat and the spider.
And to W.C. and N.K., who I have spoken to every week (and often more) for the past five years (and before). Here's to many, many more.

Contents

List of Figures

List of Tables

Acknowledgments

There are a truly expansive number of people that have enabled this Ph.D. First, thanks to my Ph.D. advisor, Prof. Steve M. Conolly, who has always come through for me and demonstrated an extraordinary effort to support all lab members in all aspects – our research, academics, careers, and personal lives. Next, thanks to my dissertation committee, which of course includes Steve, but also Prof. Peder Larson and Prof. John Clarke, and my qualifying exam committee members Prof. Phil B. Messersmith and Prof. Dorian Liepmann, for their always thoughtful and enthusiastic mentorship. I have much appreciated the astute questions and cogent research insights, as well as the very helpful career advice. I would also like to thank Steve, Prof. Phil Messersmith and Prof. Rikky Muller for several particularly excellent graduate classes spanning imaging, systems engineering, medical devices, nanomaterials and how to write an NIH-style grant, all of which were topics new to me when I began graduate school.

To my graduate student mentees (and peers and friends) K. L. Barry Fung, Caylin Colson, and Quincy Huynh, and to my undergraduate mentees Kenneth E. Jeffris and David Mai, our shared learning and living and fun are my greatest motivation. The respect, kindness and support we have always striven to give more of to each other is what has been most meaningful to me and given me the most happiness in my Ph.D. To labmates Prashant Chandrasekharan, Ph.D., Elaine Y. Yu, Ph.D., Paul Keselman, Ph.D., Bo Zheng, Ph.D., Yao Lu, Ph.D., Benjamin Fellows, Ph.D., Zhi Wei Tay, Ph.D., Daniel Hensley, Ph.D., Ryan Orendorff, Ph.D., Friso Heslinga, Yueting Shi, Kuan Lu, Ph.D., Patrick W. Goodwill, Ph.D., and to alumni I never got to work directly with but have worked with your theories, hardware, software – Laura Croft, Ph.D., Emine Saritas, Ph.D., Gary Lee, Ph.D. – and to Steve, who is in the lab as much as any of us, thank you for the fun of the shared intellectual conversations and incredible research. It is a testament to the tight-knit nature of the Conolly lab that almost everyone I am listing is an alum (as is the nature of being a senior grad student) and yet I have spoken to almost all of you in the past two months. I also want to thank my friend and former housemate Hojae Lee here – she has brainstormed new ideas and debugged experiments with me, checked my calculations, looked over my qualifying exam presentation and proposal (and that of my mentees' as well!), taught me how to do a dissection, shared relevant literature – in short, she is an honorary Conolly lab member and an exemplary researcher and friend.

Thanks also to our many collaborators, including Payam Nahid, MD, Thienkhai Vu, MD, Ph.D., Larry Fong, MD, Cordula Grüttner, Ph.D. at Micromod Partikeltechnologie, Erika Vreeland, Ph.D. at Imagion Biosystems and the Schaffer Lab for readily enabling many of our projects. There are also many facilities, labs and people that have provided additional support and equipment for my research: the Biomolecular Nanotechnology Center (BNC) run by Paul Lum (who is also a fount of engineering, industry and life wisdom that has cheered and comforted me, as have the instant noodles), the Berkeley Preclinical Imaging Center (BPIC) run by Prof. Michael Wendland, the Stem Cell Culture Facility (SSCF) run by Mary West, Ph.D., the Cell Culture Facility (CCF) run by Alison Killilea, Ph.D., Mike

Bentley and Chris Hardin in Stanley Hall receiving (who always brought our many deliveries with good cheer and encouraged me when I was having a tough day in lab), the Office of Laboratory Animal Care, the Liepmann Lab, Francis Lab, Healy Lab, Messersmith Lab, Xu Lab, Herr Lab, Kristin Olson, Robert Frawley, and Claris Garzon.

I'd also like to thank our funding sources: the NIH, the NSF-GRFP fellowship, CIRM, TRDRP, the Lloyd fellowship and the public that ultimately provides this funding. As a Ph.D. student at UC Berkeley, a B.S. student at the University of Maryland College Park, and a K12 student in the Montgomery County Maryland school system, I have had the pleasure of a world class, fully public school education.

In this realm, much credit must be given to those who empowered me towards entry into graduate school, including my family and the Mathematics, Science and Computer Science Magnet program at Montgomery Blair High School. I was enabled to seek research experiences, and Prof. Valerie V. Hu gave me my first opportunity to perform research in high school. That summer, falling asleep at my desk as I slogged through research papers for the first time, designing and running RT-qPCR after RT-qPCR experiment day after day, I understood for the first time lifelong passion and understood that mine would be for biomedical research. Her lab and her passion for research, her kindness and incredible insight – all traits shared by her (at the time) graduate students AnhThu Nguyen, Ph.D., and Prof. Tewarit Sarachana – shape my research to this day.

The BioChIP REU enabled my first foray into bioengineering research in college, and Frankie Myers, Ph.D., Seung-Min Park, Ph.D., and Prof. Ofer Rog were excellent mentors in the how to's of getting into a top-tier Ph.D. program. A poster on the BioChIP work with my partner Elisa Wasson was also the ticket to my next step, gaining me the notice of Prof. William E. Bentley. The warmth, constant influx of new ideas and collaboration in the Bentley lab were an unparalleled research environment. My graduate student mentor Tanya Tschirhart, Ph.D. taught me so much about how to work and succeed on a long project (the type one does in a Ph.D.), about the type of mentor I would want to be, and about who I would want to be. Last, my undergraduate thesis committee Prof. Bentley, Prof. Gregory Payne and Prof. Ian White were always incredibly supportive and kind. They always saw what I was trying to show them and believed in whatever parts of me I was willing to show wholeheartedly. I hope to give back to give forwards what I have been given, to hear what each person is saying and to give them my full trust and support, to debug and discover and develop, to teach and collaborate and live. A very deep and wide thank you to all.

Chapter 1

Introduction to Applications in Magnetic Particle Imaging

1.1 Attribution

Permission has been granted from the committee chair and coauthors to adapt this work from the previously published paper, Magnetic particle imaging for radiation-free, sensitive and high-contrast vascular imaging and cell tracking, by Xinyi Y Zhou, Zhi Wei Tay, Prashant Chandrasekharan, Elaine Y Yu, Daniel W Hensley, Ryan Orendorff, Kenneth E Jeffris, David Mai, Bo Zheng, Patrick W Goodwill and Steven M Conolly [160].

1.2 Introduction to MPI

Magnetic particle imaging (MPI) is a new tracer imaging technique first introduced by Philips, Hamburg [37]. MPI directly images the location and concentration of superparamagnetic iron oxide nanoparticle (SPIO) tracers with time-varying magnetic fields and has remarkably high sensitivity and contrast. Several SPIOs are clinically approved and currently on the market, including Feraheme (ferumoxytol), which is FDA approved for treatment of anemia in chronic kidney disease (CKD) patients [86]. Outside of the United States, SPIOs are available for patient imaging (Resovist), sentinel lymph node localization (Sienna) and hyperthermia (NanoTherm) applications [112, 138, 153]. Safe, radiation-free scanning in MPI combined with high-contrast, high-sensitivity imaging gives MPI fundamental advantages in vascular imaging and cell-tracking, which we discuss in this review.

The physics of MPI relies on the electronic magnetization of SPIOs [37]. When an excitation field is applied to SPIOs in the field-of-view (FOV), the magnetic dipoles reorient rapidly in response. Much like in MRI, the change in magnetization can be visualized via Faraday's law with a receiver coil. Unlike MRI, the change is of electronic magnetization, rather than nuclear magnetization. This results in a higher sensitivity for MPI, as the electronic magnetization of iron is 22 million times stronger than that of the nuclear magnetization of water at 7 Tesla [120]. To localize this signal, a large gradient field is used, as shown in Fig. 1.1. Outside of a small region with a near zero field, termed the field free region (FFR), the gradient locks SPIOs in place even if the excitation field is applied. Inside the FFR, the SPIOs reorient in response to the excitation field. By rastering this FFR across each point in the FOV, an image is created.

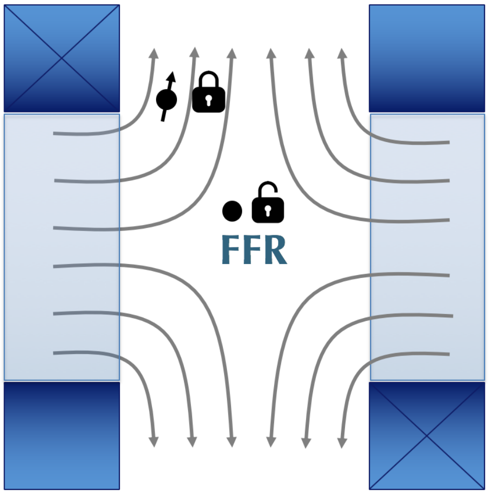

Figure 1.1: **The Field Free Region (FFR).** The FFR allows signal localization in MPI. SPIOs outside of the FFR are locked in place and cannot generate signal in an inductive pickup coil, while SPIOs inside the FFR are free to move.

MPI sensitivity can be as low as nanograms of iron (corresponding to as few as ∼200 cells for cell tracking applications), and resolution can be as fine as ∼1 mm [106, 100]. These specifications were obtained on academic prototype scanners. Commercial preclinical MPI scanners were only recently introduced by Bruker GmbH and Magnetic Insight Inc, and specifications are steadily improving. Theoretical work predicts that a human MPI scanner could have picogram sensitivity in a 1 second scan [36] and technical improvements have been made approaching this goal [45]. MPI has no view limitations, and it works robustly even in the lungs and bones, where MRI and Ultrasound routinely fail. Indeed, researchers have demonstrated proof-of-concept studies for MPI imaging of lung perfusion and ventilation [159, 6, 96]. MPI also has no depth limitations, unlike optical imaging methods. Many molecular reporters employed in cell culture studies and small animals employ optical fluorescence or bioluminescence probes, which are fundamentally limited by optical scattering and attenuation to surface applications. Last, unlike radiotracers, the SPIOs reporter half life is essentially infinite, enabling researchers to track the location of labeled cells even three months after introduction to a murine model [158]. This may be enabling since Nuclear Medicine reporters last for only hours (FDG 2 hours half life, Tc-99m 6 hours, In-111 2.8 days) while many pathophysiologic processes require weeks to manifest. Finally, MPI obtains a dose-limited sensitivity that is already competitive with Nuclear

Medicine method on prototype MPI scanners. In the next sections, I discuss applications development in MPI.

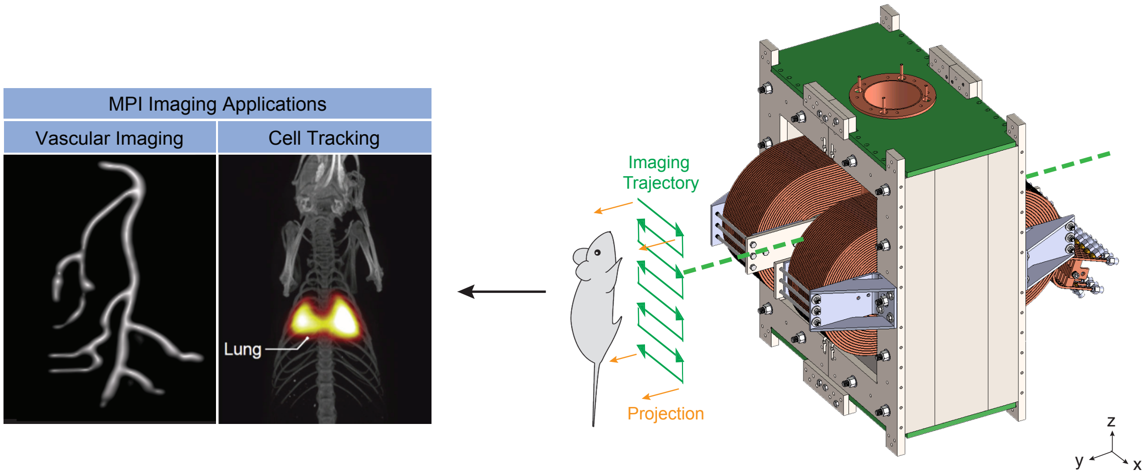

Figure 1.2: **MPI Imaging Applications today.** Broadly, MPI researchers have pursued vascular imaging and cell tracking. In vascular imaging, researchers have used both tracers that passively highlight the physiology of interest, or are specifically targeted via an antibody or other moiety. In cell tracking, researchers have imaged several types of stem cells, and more recently interest has grown in imaging immune cells for infection imaging, immunotherapy tracking and early-stage cancer detection. Scanner schematic adapted with permission from [156]. Copyright 2017 American Chemical Society.

Vascular imaging phantom image courtesy of Justin Konkle. Stem cell tracking image courtesy of Bo Zheng. Image fusion of MPI (color) and CT (grey).

1.3 Vascular Imaging

The earliest applications of MPI focused on vascular imaging with untargeted SPIOs, such as 3D imaging of a beating mouse heart using Resovist [154]. This early work emphasized some of the inherent advantages of MPI – three-dimensional, high-contrast and fast imaging. Both imaging speed and circulation time of the MPI tracers are crucial for vascular applications.

SPIOs used in MPI typically have a hydrodynamic diameter between 50-100 nm, and they remain in the bloodstream until cleared by the reticuloendothelial system [48]. Circulation time varies from minutes to hours depending on the nanoparticle coating. Early MPI researchers typically relied on ferucarbutran (also known as Resovist or VivoTrax), which is a cyclodextrin coated SPIO originally designed as a MRI liver imaging agent to highlight

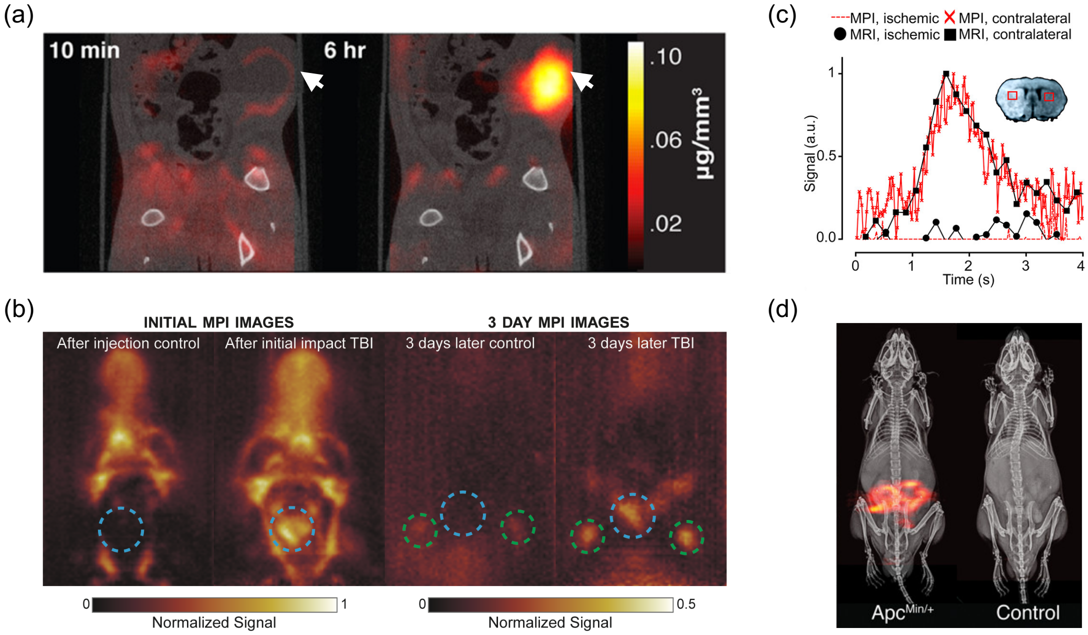

Figure 1.3: **Selected MPI vascular imaging applications.** *(a) Cancer imaging of rats.* MPI/CT of a human breast tumor xenograft shows enhanced image contrast 6 h after SPIO injection. Arrows indicate tumor volume. Adapted with permission from [155]. Copyright 2017 American Chemical Society. *(b) Traumatic brain injury (TBI) imaging of rats.* Blue dotted circle indicates impact site. Green circles indicate lymph nodes. The TBI rat has significant signal from the hemorrhage, as well as signal inside the lymph nodes, unlike the control [99]. Copyright Institute of Physics and Engineering in Medicine. Adapted with permission of IOP Publishing. All rights reserved. *(c) Stroke imaging of mice.* MRI and MPI signals were plotted over time for certain selected regions of interest: filled black circles, MRI signal ischemic hemisphere; filled black squares, MRI signal healthy hemisphere; red dotted line, MPI signal ischemic hemisphere; red crosses, MPI signal healthy hemisphere). The concentrationtime curves of the MPI and MRI showed similar progression and reduced wash-out of the contrast agents into the ischemic hemisphere. Reprinted with permission from [87]. Copyright 2017 American Chemical Society. *(d) GI bleed imaging of mice.* Dynamic projection MPI and subtraction MPI images, both co-registered to X-ray anatomical reference, allow detection and quantification of GI bleed in a ApcMin/+ mouse model predisposed to GI polyp development. Reprinted with permission from [156]. Copyright 2017 American Chemical Society.

cancerous lesions [154]. It targets the liver within minutes [112]. The Krishnan group at University of Washington developed SPIOs with 2-fold better spatial resolution compared to Ferucarbutran and extended the circulation time of MPI SPIOs to 2+ hours in mice and 4+ hours in rats using polyethylene glycol coatings [66, 63]. Alternative approaches to increasing MPI tracer circulation time include loading SPIOs into red blood cells [106, 91, 130]. These long-circulating tracers are crucial for applications like cancer imaging via the enhanced permeability and retention (EPR) effect [155], brain imaging for traumatic brain injury (TBI) and stroke via visualizing cerebral blood volume and cerebral blood flow [87, 99], and gastrointestinal (GI) bleed imaging [156]. Each of these applications shown in Fig. 1.3 requires imaging over hours or days, and hence long circulating SPIO tracers offer MPI an advantage over nuclear medicine techniques, in which radionuclide decay limits the imaging time course. As an example, longer circulation time enables blood volume and blood perfusion studies in the brain, which could aid in stroke diagnosis and treatment planning. We can also appreciate the information available from the high resolution of MPI optimized tracers. For instance, in Fig. 1.3a at 10 minutes the initial wash-in of nanoparticles into the tumor margins is visible. This subtle rim enhancement is discernible hours before the SPIOs have highlighted the entire tumor at the 6 hour time point.

Recently, groups have employed both biochemical and biomechanical targeting moieties on SPIO surfaces to highlight pathophysiologies. Biochemical active targeting to cancers includes using lactoferrin to highlight brain glioma [5, 141], while biomechanical targeting includes labeling macroaggregated albumin (MAA) with SPIOs to evaluate lung perfusion or directly administering nebulized SPIOs to the lung airways [159, 96, 6]. Unlike radiotracers, SPIO signal is stable over time, obviating the need for preparation immediately before patient use. The convenience and image quality of 3D MPI with targeted SPIOs will enable MPI scans as a compelling alternative to FDG-PET or Tc99m-V/Q scintigraphy for diagnosing cancer and pulmonary embolism, respectively. Future work in vascular imaging will continue in this vein to highlight specific pathophysiologies and harness the increasing resolution of MPI technology to highlight previously hidden perfusion behavior.

1.4 Cell Tracking

In recent years, stem cell tracking has gained research traction as a theranostic technique. Successful stem cell therapy requires verification that stem cells reach their intended destination, remain there over time and maintain viability to eventually create functional tissues or organs. MPI tracking of stem cells, shown in Fig. 1.4, has been demonstrated to quantitatively image the biodistribution of intravenously administered stem cells in rats, neural implants of stem cells in rats, and neural implants of stem cells in mice [157, 158, 14]. Of note is that the study tracking the biodistribution of intravenously administered stem cells was able to robustly image the presence of stem cells in the lungs, an area which is traditionally difficult for MRI and Ultrasound due to artifacts caused by air-tissue interfaces. Moreover, the neural implant work imaged stem cells over 87 days, a study which would not be possible with the clinical tracer modalities today due to the need for radioactively decaying tracers. These early studies on stem cell lines have sparked further interest in the field of MPI stem

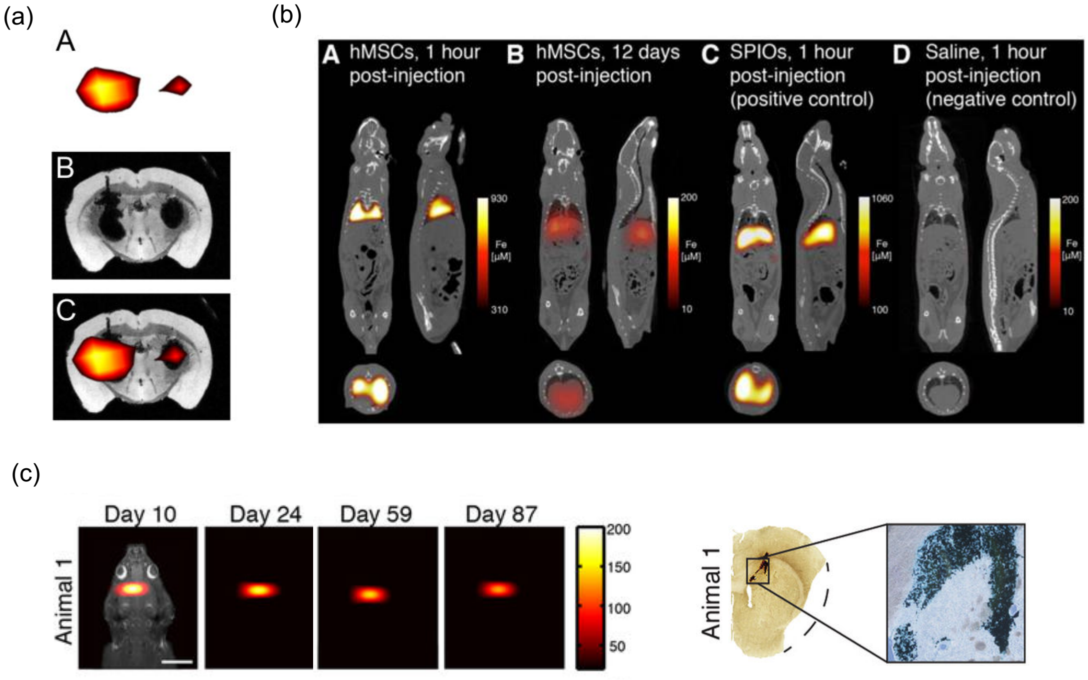

Figure 1.4: **Selected MPI cell tracking applications.** *(a) Stem cell implant imaging in mice.* MPI (A), MRI (B) and corresponding overlay MPI/MRI (C) of a mouse brain transplanted with 1×10^5 (left hemisphere) or 5×10^4 (right hemisphere) SPIO-labeled mesenchymal stem cells. Reproduced from [14] under the CC BY-NC-ND license (http://creativecommons.org/licenses/by-nc-nd/4.0/). *b) Stem cell injection imaging in rats. 3D MPI-CT imaging of intravenously injected human mesenchymal stem cells (hMSCs) and SPIO control.* (A) MPI imaging of hMSC tail vein injections <1 hr post-injection shows substantial hMSC localization to lung. (B) At 12 days, hMSC tail vein injections show significant total clearance and liver migration. (C) MPI imaging of SPIO-only tail vein injections less than one hour post-injection shows immediate uptake in liver and spleen. (D) Control injections of isotonic saline show no detectable MPI signal. Reproduced with permission from [157] under the Creative Commons Attribution (CC BY-NC) License (https://creativecommons.org/licenses/by-nc/4.0/). *(c) Long-term stem cell implant imaging in rats.* (LEFT) Longitudinal MPI imaging of 5×10^5 SPIO-labeled human NPCs implanted in the forebrain cortex over 87 days. Scale bar 1 cm. Color intensity in ng/mm^2. (RIGHT) Postmortem Prussian blue (PB) staining confirms presence of iron-labeled cells at administration site. Adapted with permission from [157] under the Creative Commons CC BY License (https://creativecommons.org/licenses/by/4.0/).

cell tracking, leading to work demonstrating that MPI can be used to image pancreatic islet transplants in mice and work developing new nanoparticle agents for multimodal imaging of stem cells, including via MPI [149, 80]. These studies demonstrated up to 200-cell sensitivity, which is far more sensitive than other medical imaging modalities [95]. Last, recent progress has been made in correlating MPI relaxation times to stem cell viability *in vivo* [30]. This technique relies on analyzing the harmonic spectra of the MPI signal (Magnetic Particle Spectroscopy - MPS) to determine if the SPIOs are still within the cell or have been released to the outside after cell death. With new particle and arbitrary excitation design [134], it may be possible to further distinguish stem-like states versus apoptotic or non-stem states.

Researchers have recently explored MPI for tracking prelabeled white blood cells (WBCs), which could emerge as a radiation-free alternative to infection imaging via traditional WBC-In111 scintigraphy (Gaudet *et al.*, Zhang *et al.*, Chandrasekharan *et al.*, World Molecular Imaging Conference, Philadelphia, September 2017). Preliminary work has shown that MPI can track cultured macrophages in both healthy and middle cerebral artery occlusion (MCAO) stroke mice, and tumor-associated macrophages in a 4T1 mouse model of metastatic cancer. Future work in MPI cell tracking is expected to extend these imaging studies to theranostic applications, such as tracking stem cell migration for disease treatment, or immune cell migration for immunotherapy treatment of cancers.

We note that the theranostic potential of MPI extends far beyond guiding cell-based treatments. Although this review focuses on MPI imaging applications, extensive work has also been performed demonstrating the utility of MPI for ionizing radiation-free surgical guidance [119, 49, 111, 22] and therapeutic guidance, such as with magnetic hyperthermia [69, 54, 73, 72, 132].

1.5 Tracer Development

In the early days of MPI, researchers had to rely on SPIOs designed for T2* or T1-weighted MRI contrast agents [150]. Since MRI and MPI see SPIOs with completely different physics, the MPI performance of these SPIOs was not ideal. Dramatic improvements in sensitivity and image resolution have been enabled through tailoring of SPIOs to MPIs unique physics [23, 28, 26]. Both theory and experiment have shown that 5-20 nm core sizes show poor resolution [4, 41, 110]. Larger core sizes (>27 nm) do not perform as well as the optimal range of 20-26 nm, due to relaxation blurring [135]. While 1-2 mm resolution is comparable to nuclear medicines resolution, a dramatic improvement in spatial resolution (100 microns) would obviate perhaps the last technical weakness of MPI. Since image resolution is improved both by either better SPIOs or higher scanner gradients, these MPI-tailored SPIOs could dramatically reduce scanner cost. A ten-fold improvement in SPIO magnetic resolution could reduce the cost of a clinical MPI scanner by nearly one-hundred-fold. Hence, high-resolution SPIOs remain an exciting and crucial area in MPI research to enable safe and cost-effective human MPI.

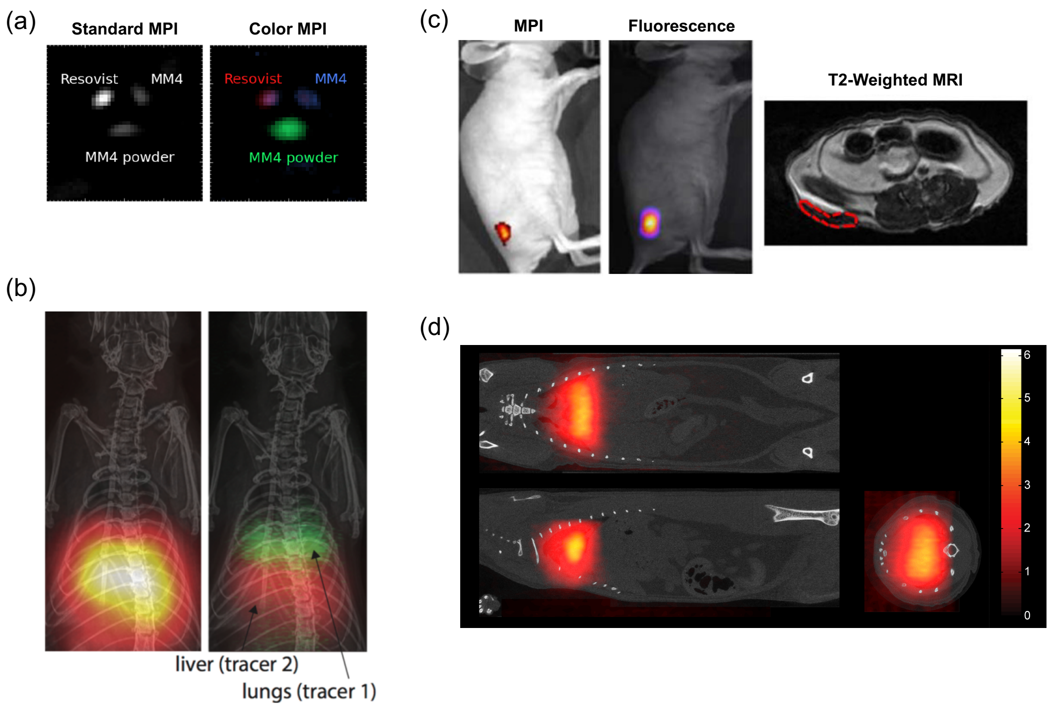

Figure 1.5: **Recent progress in tracer technologies.** *(a) In vitro tri-color MPI.* Three different MPI tracers are indistinguishable in a standard MPI reconstruction algorithm, but can be distinguished after applying a multi-color reconstruction algorithm. Adapted with permission from [108] under the Creative Commons Attribution 3.0 license (http://creativecommons.org/licenses/by/3.0). *(b) In vivo dual-color MPI.* Rat lung and liver are targeted with two nanoparticles with different relaxation behavior. In standard MPI, the organs are indistinguishable, but after the colorizing algorithm the organs can be distinguished based on the relaxation behavior of the SPIOs within. Image courtesy of Daniel Hensley. *(c) Multi-modal Janus iron oxide MPI tracers.* SPIO tracers can be designed for multi-modality imaging. Mice were subcutaneously implanted with nanoparticle-labeled cells and imaged under MPI, fluorescence and T2-weighted MRI. Adapted with permission from [126]. Copyright 2017 American Chemical Society. *(d) Lung perfusion imaging with MAA-SPIO.* Large macroaggregated albumin conjugated to SPIOs are biomechanically trapped in the rat lung, allowing imaging of blood perfusion through the lungs [159]. Institute of Physics and Engineering in Medicine. Adapted with permission of IOP Publishing. All rights reserved.

Beyond improving MPI signal and resolution, harnessing MPI physics to provide molecular contrast is an exciting research area. Color MPI extracts information about SPIO relaxation to distinguish between nanoparticles with different relaxation dynamics and opens the door to multiplexing in MPI, similar to fluorescence multiplexing [108]. This work has recently been extended to *in vivo* imaging, as shown in Fig. 1.5 (Hensley *et al.*, World Molecular Imaging Conference, Philadelphia, September 2017).

Relaxation mechanisms include Néel and Brownian, which are strongly influenced by the viscosity of the medium. In general, smaller particles exhibit mainly Néel behavior and are unaffected by the media viscosity or by binding. Larger particles exhibit mainly Brownian behavior and are very sensitive to media viscosity and to binding. Small relaxation changes can be detected via color MPI, but even standard MPI can detect large relaxation changes [33]. MPI has seen only limited research into targeted nanoparticle coatings that target specific pathophysiologies [126, 142]. It will be exciting to see the vast area of nanomedicine research applied to MPI-targeted SPIOs for high specificity and sensitivity diagnosis of disease with zero ionizing radiation.

1.6 Author's Work in Context

In this dissertation, I discuss several novel applications of magnetic particle imaging, encompassing these three main categories of applications development in MPI. First, I discuss the development of lung ventilation/perfusion (V/Q) imaging with MPI. I developed and tested *in vivo* rats the first lung perfusion MPI imaging agent (termed MAA-SPIOs), which was the first systemically administered MPI tracer targeted to a specific organ other than clearance organs. I also describe a method to pair the perfusion study with a previously developed method for MPI ventilation imaging, in which aerosolized SPIOs are delivered to rodent airways. The MPI V/Q scans described are analogous to the nuclear medicine V/Q scans, which are commonly used clinically to diagnose pulmonary embolism. The perfusion study is targeted to the lung capillaries and therefore is a type of vascular imaging application. Next, I discuss the development of MPI white blood cell (WBC) imaging, in which MPI is used to track white blood cells throughout the body. This type of cell tracking analogous to nuclear medicine WBC scans, which are commonly used to detect osteomyelitis and other difficult-to-localize infections. Last, I discuss a method for phospholipase detection via MPI relaxometry. This tracer development work demonstrates the potential to provide metabolic information via liposome SPIOs, pushing the envelope of contrast mechanisms available in MPI.

Chapter 2

Lung Perfusion MPI Imaging

2.1 Attribution

Permission has been granted from the committee chair and coauthors to adapt this work from the previously published paper, First *in vivo* magnetic particle imaging of lung perfusion in rats, by Xinyi Y Zhou, Kenneth E Jeffris, Elaine Y Yu, Bo Zheng, Patrick W Goodwill, Payam Nahid and Steven M Conolly [159].

2.2 Motivation

Pulmonary embolism (PE) is the third leading cause of cardiovascular mortality in North America, affecting 21-69 people per 100,000 per year [116, 71]. It is often fatal when untreated, carrying a 30% mortality rate, which improves to 8% with timely treatment. It occurs not only in patients comorbid with other conditions such as obesity or a history of surgery, but also in otherwise healthy patients after long-distance air travel or pregnancy [129, 52]. It is the leading cause of maternal mortality in developed countries [15]. Because patients can present with non-specific symptoms such as chest pain and/or shortness of breath, definitive diagnosis of PE remains difficult for clinicians. Up to 35% of patients initially suspected of having PE are ruled out, and conversely, many cases of PE are only diagnosed post-mortem [19].

Imaging studies are therefore necessary for the clinician to make a differential diagnosis of PE. CT pulmonary angiography (CTPA) and ventilation/perfusion (V/Q) scans are the two diagnostic imaging approaches most commonly used for clinical PE diagnosis [34, 116]. Both methods have good sensitivity and specificity when used in conjunction with other criteria. The use of CTPA is increasing despite its higher radiation dose (as much as tenfold as compared to V/Q) due to its superior spatial resolution and its ability to suggest alternative diagnoses if no clot is apparent [25, 122]. Moreover, V/Q scans, like many other nuclear medicine scans, are often only available during daytime, weekday hours compared to the widespread all-hours availability of CT in emergency departments [116].

V/Q consists of two individual scans that investigate lung performance during ventilation (V) in both inhalation and exhalation phases, and blood perfusion (Q) into pulmonary capillaries. In the ventilation scan, the patient inhales a radionuclide gas or aerosol, such as Xenon-133, and the lungs are then imaged using a gamma camera to show areas in the lungs with airflow blockages [127]. In the perfusion scan, ^{99m}Tc-MAA is injected intravenously, and the filling of the capillaries and any perfusion defects are visualized using a gamma camera [10]. ^{99m}Tc-MAA is macroaggregated albumin (MAA) chelated to the radionuclide tracer ^{99m}Technetium. MAA targets the lung because at a size range of $10 - 90\,\mu\text{m}$, it is trapped in the first capillary bed reached after IV injection, i.e., the lungs, which have $6\,\mu\text{m}$ average lumen diameter [123, 143].

In order to improve resolution and diagnostic accuracy, V/Q can incorporate single-photon emission computed tomography (SPECT) imaging to produce 3-D images that highlight perfusion defects much more accurately and consistently [114]. V/Q scans are preferred when the injection of iodine is a safety concern, such as for chronic kidney disease (CKD) patients or patients with contrast allergies [71]. V/Q is also preferred in pregnant patients due to ionizing radiation concerns and because it is more likely to be diagnostic [15].

The other major medical imaging modalities of ultrasound and MRI are poor diagnostically in the lung and thus rarely used clinically when PE is suspected [139, 104]. The ultrasound transmit wave does not penetrate the lung due to near-total reflection at the first air-tissue interface. In MRI, T_2* of lung tissue is very short due to the ± 5 ppm magnetic field disturbance outside the air-filled alveoli; fortunately, new approaches with ultrashort-TE pulse sequences and Gadolinium contrast have largely mitigated this challenge. However, the use of Gadolinium is contraindicated in patients with CKD and new studies have raised concerns about the accumulation of Gadolinium in the brain tissues of healthy patients [115, 92]. Hence, lung MRI remains uncommon in a clinical setting.

Magnetic particle imaging (MPI) is an emerging tracer imaging modality with high sensitivity and ideal image contrast, using low-frequency magnetic fields to image the spatial distribution of superparamagnetic iron oxide (SPIO) tracers. There is ideal image contrast because background tissue (bone, muscle, blood, fat) produces no MPI signal. Moreover, there is zero depth attenuation of low-frequency magnetic fields in tissue, allowing for quantitative imaging. The scanner and parameters used for data collection in this publication utilizes a field-free point (FFP) and has a sensitivity of approximately 80 ng Fe in a gradient-determined voxel [157]. However, MPI sensitivity varies from microgram to nanogram amounts ([106]) of iron because it is dependent on the tracer in addition to specific scanner geometry and scan parameters. Tradeoffs for increased sensitivity include resolution and scan time [100]. Gleich's theoretical work suggests that a human MPI scanner could have picogram sensitivity in a 1 second scan [36].

Some of the SPIOs used in MPI experiments have already been clinically approved as MRI contrast agents [150]. These tracers clear through the liver and spleen and are degraded in these organs; the iron is taken up by iron storage proteins such as ferritin and hemoglobin [81]. However, MPI-optimized tracers with improved MPI resolution and SNR are different than MRI-optimized tracers and much more characterization must be done to fully evaluate

	V/Q Scan	**CTPA**	**MPI Q Scan**
Sensitivity	91.7%	100%	TBD
Specificity	92.9%	92.9%	TBD
Radiation Dose	0.21-2.4 mSv	4.2-19.9 mSv	Zero
Contrast Agent/Tracer	^{133m}Xe gas (V) ^{99m}Tc-MAA (Q)	iodine	SPIOs
Dose	1.4 mL ^{99m}Tc-MAA	100 mL (30 g iodine)	5 mg/kg (< 0.5 g)
Target Population	Contrast allergy, renal insufficiency	Healthy patients	Healthy patients
Availability	Up to 3-4 hour wait (tracer prep)	24/7	24/7

Table 2.1: **Comparison of MPI to Current Modalities for PE Diagnosis.** While the sensitivity and specificity of MPI for PE diagnosis is yet to be tested, MPI has several ideal characteristics for PE detection. Note that up to 25% of patients may have a sensitivity to iodine or weak kidneys, resulting in a need for a CTPA alternative [78, 129, 120, 60, 94, 7, 38, 20].

the pharmacokinetics and clearance of these new tracers [23, 28, 27].

MPI has a comparative advantage over several modalities in lung imaging because there are no air-tissue interface artifacts nor ionizing radiation. While MRI requires parts-per-million levels of magnetic field homogeneity, MPI requires only a few percent field homogeneity for the drive field. Hence, the MPI signal in lung capillaries is *completely unaffected* by the ± 5 ppm magnetic field disturbance produced by nearby air-filled aveoli, which can cause severe artifacts in conventional MRI. MPI also carries safety advantages over CT and V/Q for PE diagnosis since the lungs are particularly vulnerable to radiation dose. A perfusion scan using ^{99m}Tc-MAA delivers a typical radiation dose of 100-250 MBq or 0.21-2.4 mSv for the complete V/Q scan [114]. For reference, a a dental X-ray delivers 0.005 mSv. Because the MPI tracer and scanning process use no ionizing radiation, it is one of the safest tracer imaging modalities to date and has potential for clinical translation [44, 107]. A summary of the characteristics of the common clinical diagnostic scans to diagnose V/Q and the characteristics of MPI are shown in Table 2.1.

Previously, Nishimoto [96] demonstrated promise for MPI in lung imaging with the first *in vivo* MPI ventilation studies in mice using a nebulized microsprayer to deliver Resovist to the lungs. Here, we report a method for preparing a novel MPI lung perfusion imaging agent, macroaggregated albumin-SPIOs (MAA-SPIOs), and demonstrate its efficacy and biodistribution for *in vivo* MPI lung perfusion imaging in rats. We combine this method for lung perfusion imaging with the previously demonstrated method for lung ventilation imaging, facilitating the first MPI V/Q images.

2.3 Methods

MPI Lung Perfusion Imaging

Preparation of SPIO-Labeled MAA

Macroaggregated albumin preparation was adapted from methods in Hunt et al. [57] and Sajid et al. [118]. Biotinylated bovine serum albumin (bBSA) was purchased from Pierce Biotechnology (Rockford, IL, USA) and multicore streptavidin-functionalized perimag (formerly known as nanomag-MIP) iron oxide nanoparticles were purchased from micromod Partikeltechnologie GmbH (Rostock, Germany). Perimag SPIOs are synthesized through coprecipitation and have a polydisperse cluster morphology with a mean effective magnetic diameter of 19 nm; they are described fully in [23]. For transmission electron microscopy, perimag particles were deposited onto a carbon film copper TEM grid from Electron Microscopy Sciences (Hatfield, PA, USA) and imaged using a 120 kV FEI Tecnai 12 transmission electron microscope (FEI, Hillsboro, OR). 1.5 mg/mL bBSA and 0.1 mg/mL perimag in pH 5.4, 0.1 M acetate buffer were stirred for 10 minutes, then heated with stirring at 1150 rpm for 20 minutes in a 70 C hot water bath. The mixture was cooled at room temperature with stirring for 10 minutes, pushed through a 70 µm filter and finally spun down at 2000 relative centrifugal force (rcf) and resuspended in 1 mL saline.

Using a hemocytometer and images taken with an Olympus IX70 inverted optical microscope, the polydispersity of MAA-SPIO was determined using a custom Matlab (Mathworks) script. For measurements of size stability, MAA-SPIOs were stored in saline at 4 C and counted every day for four days after initial preparation. Roughly 200-300 MAA-SPIO particles out of the entire sample were counted each time.

Animal clearance experiments of MAA-SPIOs

All animal procedures were conducted according to the National Research Council's Guide for the Care and Use of Laboratory Animals and approved by UC Berkeley's Animal Care and Use Committee. Female Fischer 344 rats at 25 weeks old, weighing on average 154 g, were used for *in vivo* imaging. All animals were fed on an *ad libitum* diet of Teklad Rodent Diet 2018 (Harlan, Indianapolis, IL). Briefly, three groups of rats anesthetized under isoflurane (4% for induction and 3.5% for maintenance, 1.5 L/min flow) received tail vein injections by hand with a maximum total volume of 1 mL of sterile phosphate buffered saline (PBS) and either a perimag or MAA-labeled perimag bolus at a dose of 0.4 mg Fe/kg. Roughly 700,000 MAA particles were in each dose of MAA-SPIO, with approximately 1.4×10^5 SPIO particles per MAA-SPIO. Imaging was started 10 minutes post-injection unless otherwise stated in the figure. CT was performed post-mortem.

MPI Lung Perfusion Imaging

A custom-built 3D MPI scanner with 7 T/m field free point gradient and ∼1.5 mm full-width-at-half-maximum resolution was used for imaging, as previously described in [120, 157]. The system used drive field frequency of 20.05 kHz and excitation strength of 40 mTpp, with 10 minute scan time for a 4×4×10.6 cm field-of-view (FOV) for the time course scans in Fig. 2.6, and 4×3.75×10.6 cm FOV for all other MPI scans. Live animals were imaged under isoflurane anesthesia (2%, 1.5 L/min) with respiratory gating to reduce breathing artifacts. In the gating process, a pneumatic breath pad is placed on the animal to track animal breathing movement. Imaging only proceeds in the period when the animal is done with each breath; this minimizes movement artifacts. The measurement time reflects the total scan time with gating. MPI images were reconstructed using an x-space MPI reconstruction and rendered in this paper as maximum intensity projections (MIPs) [40, 41, 85]. MIPs were generated by projecting the voxel with the highest value on every slice throughout the volume into a 2D image. MIPs were chosen because it is difficult to show the full biodistribution of the particles in a single slice because the organs are located in different depths throughout the body. Six perimag SPIO point sources from 1 to 10 µg were used to construct a calibration curve ($R^2 = 0.94$). Note that the quantification may be less accurate after the MAA-SPIOs travel past the lungs due to the MAA-SPIOs degrading and being taken up into the microenvironment of phagosomes [137, 81]. Images were visually coregistered to CT skeletal references taken on a RS9-80 Micro CT scanner (GE) with 17-minute acquisition time and 93 µm isotropic resolution. All data acquisition, control, data processing and visualization were performed with MATLAB. MAA-SPIO clearance half-life from the lung was calculated by summing the signal in a region-of-interest around the lung and applying an exponential fit over the time course.

Organ Excision and Imaging

To confirm the location of tracers 10 minutes post-injection, animals were sacrificed and dissected. The lungs, liver, heart, and spleen of these animals were removed and imaged using MPI as previously described.

MPI Lung Ventilation Imaging

Aerosol Inhalation Setup

SPIOs (PerimagTM, micromod Partikeltechnologie GmbH, Rostock, Germany) was added to the aerosol mix in order to track the aerosol in vivo with magnetic particle imaging. In short, the nebulizer was connected in line between the y-junction and the output of the rodent ventilator device to inject the aerosol into the ventilation airstream to be inhaled by the rodent. SPIONs were mixed into 1x phosphate buffered saline to a final concentration of 5 mg/mL (1.7 mg iron / mL). Due to the low concentration, the aerodynamic properties of the aerosol droplets should be negligibly affected by addition of SPIONs ($< 0.5\%$ weight change).

Roughly 0.3 mg/kg of SPIONs were delivered into the rodents via aerosol inhalation and MPI scans were acquired at multiple time points up to 13 days after to evaluate clearance from the lung. Aerosol was generated by a vibrating mesh nebulizer (AeronebTM Lab Nebulizer Unit, Small VMD, Kent Scientific Corporation, Connecticut, USA) and the ventilator has tunable stroke volume and rate (Model 683 Small Animal Ventilator, Harvard Apparatus, Holliston, MA, USA).

MPI Lung Ventilation Imaging

The scanning methods described for MPI lung perfusion imaging above were closely adapted for lung ventilation imaging. However, animals were imaged on the UC Berkeley 6.3 T/m field-free-line (FFL) [156] instead of on the FFP scanner. The FFL produces 2D projection images instead of 3D images, and can image the same FOV in 1/5th of the time. Both scanners have a drive field frequency of 20.225 kHz and an excitation strength of 40 mTpp.

MPI Ventilation/Perfusion Imaging

The animal first received the MAA-SPIO lung perfusion agent and MPI imaging immediately thereafter. After waiting 24 hours for MAA-SPIOs to clear to the liver and spleen, the animal received aerosolized SPIOs and ventilation imaging. Scans were performed on the UC Berkeley 6.3 T/m FFL scanner as described earlier.

2.4 Results

MPI Lung Perfusion Imaging

Fabrication and Characterization of MAA-SPIOs

Using a combination of biotin-streptavidin binding and non-specific aggregation of albumin in acetate buffer through heating, we prepared macroaggregated albumin conjugated to a SPIO tracer (MAA-SPIOs), as shown in Fig. 2.1.

Optimization of the size and morphology of MAA is shown in Fig. 2.2. After an appropriate protocol to produce MAA was identified, streptavidin-coated SPIOs were incorporated into the solution of (biotin-coated) BSA. Characterization of the optimized MAA-SPIOs is shown in Fig. 2.3. By light microscopy, MAA-SPIOs had a particle distribution with 98% of particles <70 µm in length with no particles >83 µm observed. A representative micrograph is seen in Fig. 2.3(a). Note that the perimag SPIO clusters, visualized through transmission electron microscopy in Fig. 2.3(b), are several orders of magnitude smaller and therefore have little effect on MAA size. The mean MAA particle size was 25 µm with a standard deviation of 13 µm. A histogram of 327 particles counted on a hemocytometer is shown in Fig. 2.3(c). MAA-SPIOs were stable and maintained a similar size distribution over five days, with mean particle size 27 µm with a standard deviation of 13 µm on day 5, as shown in

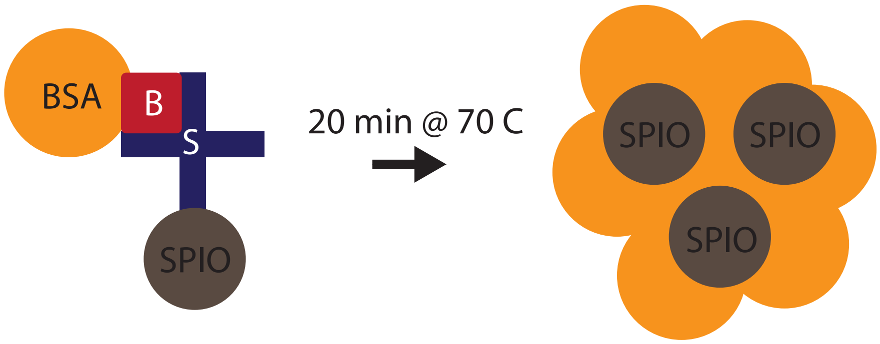

Figure 2.1: **Preparation of MAA-SPIOs.** Biotinylated albumin is conjugated to streptavidin-functionalized SPIOs, then heated with stirring to form macroaggregates. B = biotin, S = streptavidin, BSA = bovine serum albumin, SPIO = superparamagnetic iron oxide nanoparticle.

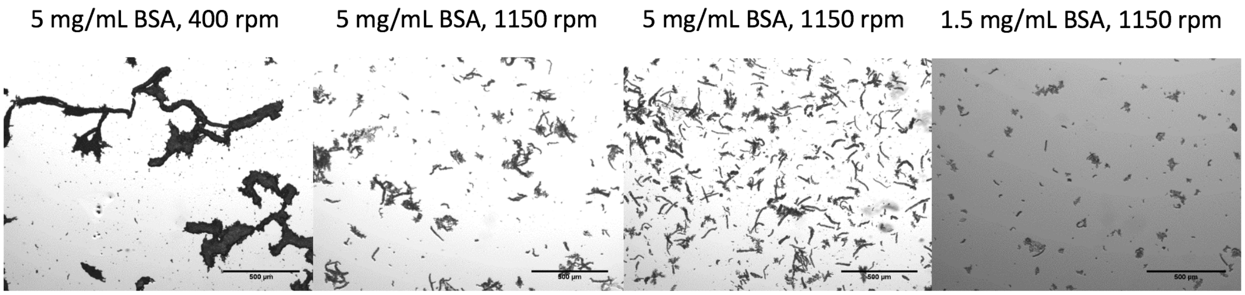

Figure 2.2: **Optimization of Macroaggregated Albumin Size.** Solutions of bovine serum albumin (BSA) at different concentrations and different stir speeds were heated for 20 minutes at 70 C, resulting in variable aggregate sizes and morphologies.

Fig. 2.3(d). The morphology and size distribution is comparable to that of commercial MAA kits, for which "more than 90% of the particles are between 10 and 70 micrometers, while the typical average size is 20 to 40 micrometers; none is greater than 150 micrometers." [60, 97] Note that the MAA-SPIO fabrication process does not degrade the MPI signal intensity, as shown in 2.3(e). The phantom shape is slightly different since the large MAA-SPIOs settle down and compact in the test tube, but the overall iron concentration was found to be the same.

Based on the particle sizes, it is expected that following intravenous injection, the particles will be entrapped in the pulmonary capillary bed because the particles are larger than the 6 µm of the typical rat capillary. Note that average human lung capillaries are also roughly 6 µm in diameter, hence a similar principle could be used to design MAA-SPIOs for human studies [123, 143].

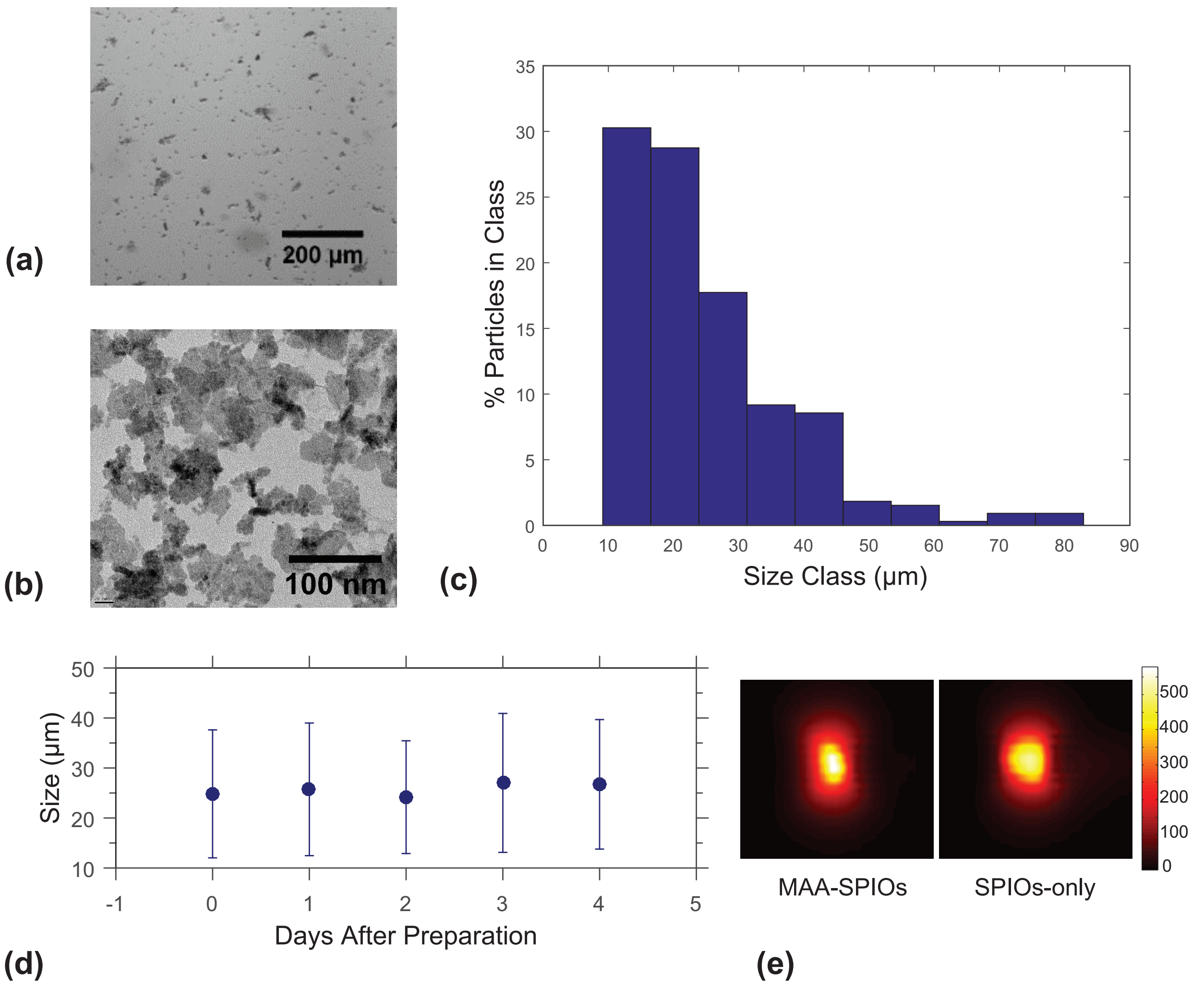

Figure 2.3: **Characterization of of MAA-SPIOs.** (a) Brightfield image of MAA-SPIOs. 200 µm scale bar. (b) TEM image of perimag SPIO clusters. 100 nm scale bar. (c) Histogram of MAA-SPIO size distribution (of 327 particles measured). (d) Size stability of MAA-SPIOs in saline over five days (∼200-300 particles measured each day). (e) MPI scans of roughly 2 million MAA-SPIO and equivalent iron concentration SPIO only phantoms, each in 80 µL water. Colorbar for both scans in µg Fe/cm^3.

In Vivo Imaging of Lung Perfusion in Rats

The hypothesis that lungs will entrap MAA-SPIOs following intravenous injection is confirmed via magnetic particle imaging (MPI). Fig. 2.4(a) shows that MAA-SPIOs are visible in MPI and effectively target the lung perfusion within 10 minutes after a venous injection. SPIOs only localize to the liver and spleen as expected, shown in Fig. 2.4(b). The rapid clearance of the SPIO control is expected since perimag is coated with dextran, a coating

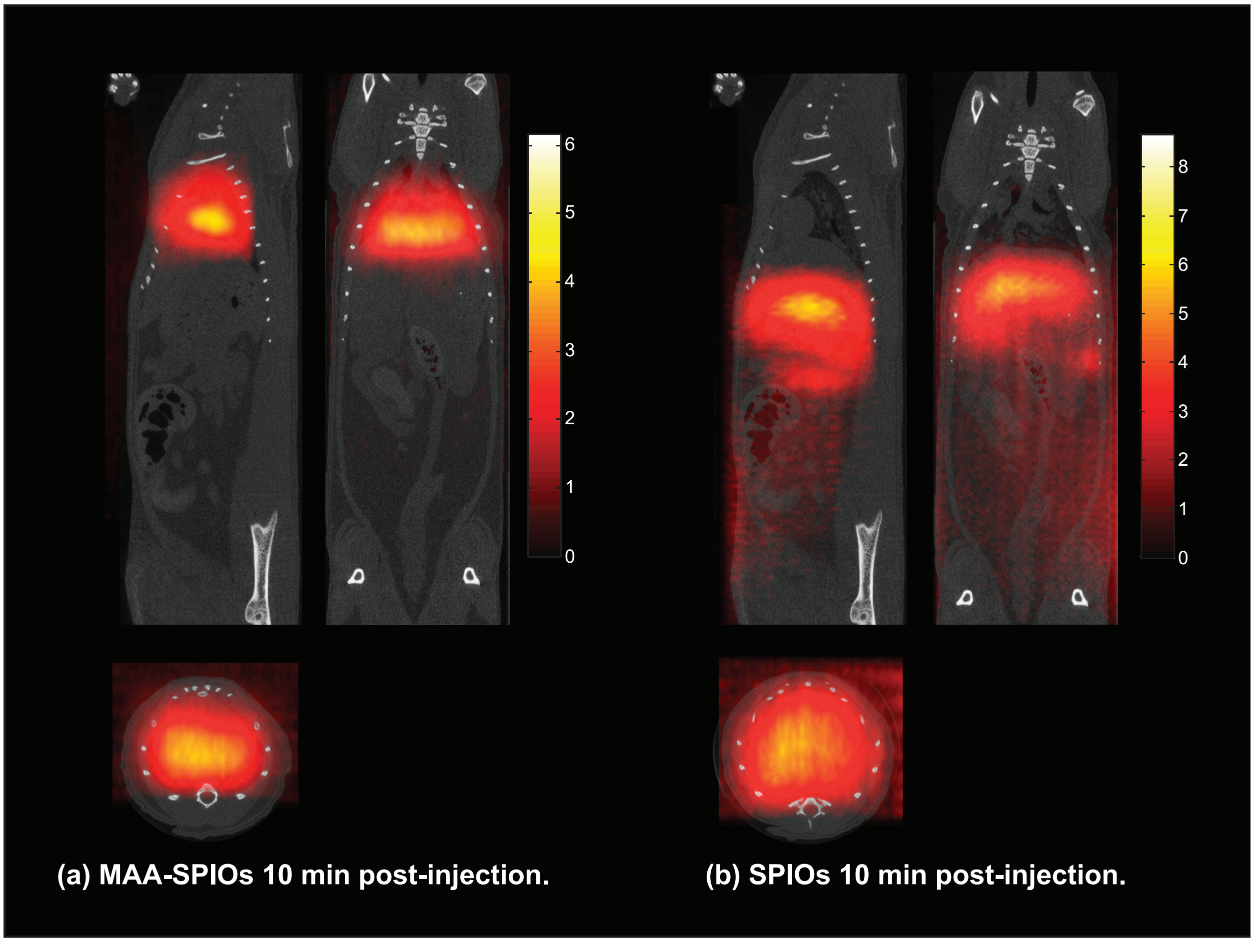

(a) MAA-SPIOs 10 min post-injection.

(b) SPIOs 10 min post-injection.

Figure 2.4: **3D MPI MAA-SPIO scans *in vivo* rats 10 minutes after IV injection, with coronal, sagittal and axial MIPs shown.** (a) 700,000 MAA-SPIOs, with approximately 1.4×10^5 SPIO particles per MAA cluster (0.4 mg Fe/kg), effectively target to the lung vasculature within 10 minutes by lodging in the lung capillary due to MAA-SPIO particle size larger than capillary diameter. (b) SPIOs (0.4 mg Fe/kg) alone do not target to the lung and instead immediately clear to the liver and spleen in 10 minutes. Streaking artifacts are apparent due to imperfect respiratory gating. Coregistration to CT. Colorbar in µg Fe/cm^3.

that has been shown to impart very short blood circulation times [125].

Ex vivo scans of excised organs, shown in Fig. 2.5(a) confirm that the MAA-SPIOs localize to the lungs, with 80% of the signal seen in the lungs vs. only 20% in the liver, and a 9:1 lung to liver maximum signal intensity ratio. In comparison, dissected control rats given an SPIO-only injection, seen in Fig. 2.5(b) show signal only in the liver and spleen.

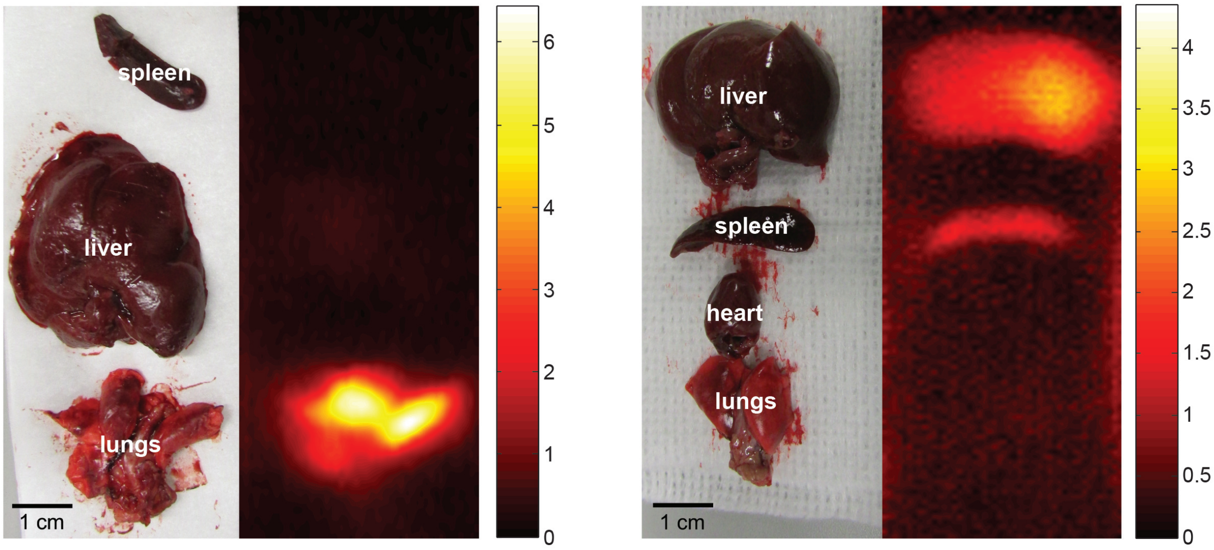

(a) MAA-SPIOs

(b) SPIOs-only

Figure 2.5: **3D MPI scans of excised organs, displayed as MIPs.** (a) Organs excised from animal injected with 700,000 MAA-SPIOs, and approximately $1.4{\times}10^5$ SPIO particles per MAA cluster (0.4 mg Fe/kg), and sacrificed 10 minutes after injection. (b) Organs excised from animal injected with SPIOs only (0.4 mg Fe/kg) and sacrificed 10 minutes after injection. Colorbar in µg Fe/cm^3.

Clearance of MAA-SPIOs from Lungs to Liver and Spleen

As shown in MPI images coregistered with CT in Fig. 2.6, MAA-SPIOs travel to the lungs within 10 minutes and are visible only in the lungs for one hour. Because the MAA is fragile due to the non-specific aggregation method, erosion and fragmentation reduce the particle size, allowing it to pass through the pulmonary capillary bed over time. This is seen in Fig. 2.6 showing that the fragmented MAA-SPIOs were accumulated by the reticuloendothelial system, localizing in the liver and spleen, and were no longer present in the lungs after one day. The half-life of MAA-SPIO elimination from the lung was approximately 4.8 hours, compared to 2-4 hours for commercial ^{99m}Tc-MAA [60, 97, 90]. The total signal appears to drop between 30 min and 1 hour because as the initial MAA-SPIO dose spreads throughout the body, the contrast in the lungs decreases. This effect is exacerbated in the MIPs since the volume of the liver is considerably larger than that of the lungs.

MPI Lung Ventilation Imaging

Animals were intubated and administered aerosolized SPIOs as per the setup shown in Fig. 2.7. The MPI time course study in Fig. 2.8 shows the initial deposition in the lungs and the mucociliary clearance of the SPIOs into the gastrointestinal tract. Due to the

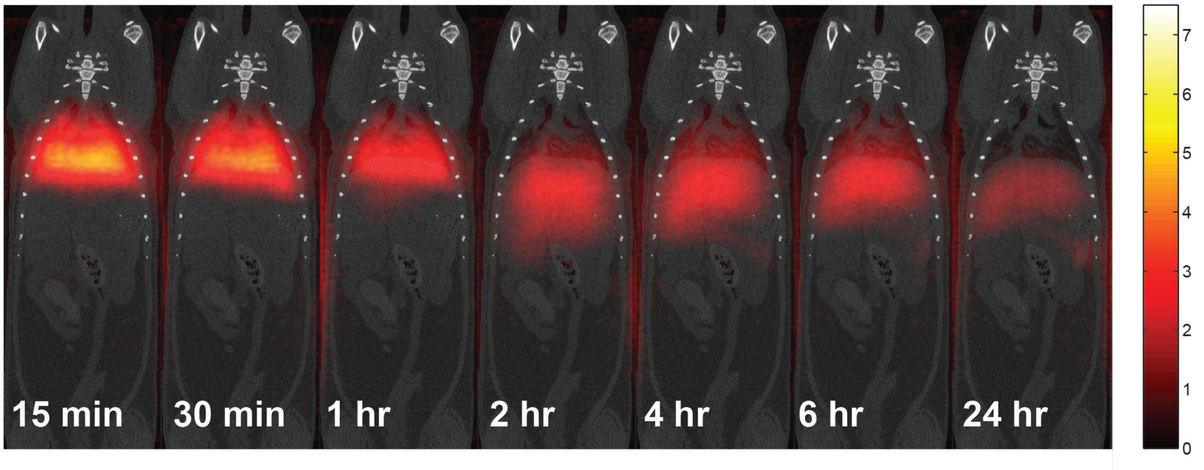

Figure 2.6: **3D MPI MAA-SPIO scans in vivo rats over 24 hours, displayed as MIPs.** 700,000 MAA-SPIOs, with approximately 1.4×10^5 SPIO particles per MAA cluster (0.4 mg Fe/kg), effectively target to the lung vasculature by lodging in the lung capillary due to MAA-SPIO particle size larger than capillary diameter. MAA-SPIOs fragment over time and clear to the liver and spleen over 24 hrs. MPI scans are coregistered to CT scans. Colorbar in µg Fe/cm^3.

large hydrodynamic size of the SPIOs (130 nm hydrodynamic size), there is expected to be negligible penetration of the blood-lung barrier. At the 20 min time point, SPIOs were clearly localized in the lungs. At the 15 day time point, SPIOs were observed in the lower gastrointestinal tract. Over the course of 15 days, the MPI signal in the lungs gradually decreased as the SPIOs were cleared from the lungs. Further data from our group confirming the mucociliary clearance pathway of inhaled SPIOs are published in Tay *et al.* (2018) [133]. The feces were collected and a two-compartment model showed that as the MPI signal in the lungs decreased, the MPI signal in the excreta increased.

MPI Lung Ventilation/Perfusion Imaging

Current MPI techniques cannot distinguish between SPIOs in the airways and SPIOs in the lung capillaries. Based on the long clearance time of inhaled SPIOs (days) as compared to the rapid clearance time (hours) of MAA-SPIOs, we decided to first image the rat lung capillaries with MAA-SPIOs, then wait for clearance over 24 hours before ventilation imaging. The procedure and resulting images are shown in Fig. 2.9. While streaks of MPI signal near the lungs are often due to gating artifacts, as is the case with the streaks on the left edge of the imaging, the vertical streak in the middle is the trachea. This was confirmed by by a longer FOV image (not shown) showing very high deposition of aerosolized SPIOs in the throat and a continuous column of SPIOs from the the throat to the lungs. The uneven deposition in the left and right sides of the lung shows one challenge of aerosol delivery via endotracheal

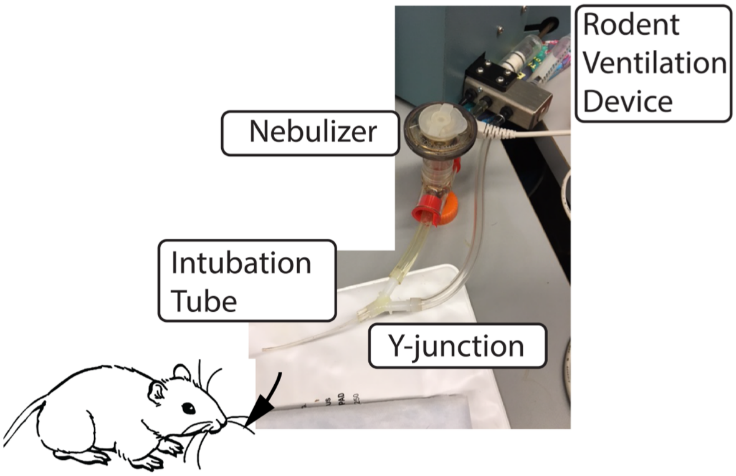

Figure 2.7: **Ventilation setup for aerosolized SPIO delivery.** Rats are mechanically ventilated with puffs of aerosolized 10 mg Fe/mL SPIOs. Aerosol droplets are $< 4\,\mu\text{m}$.

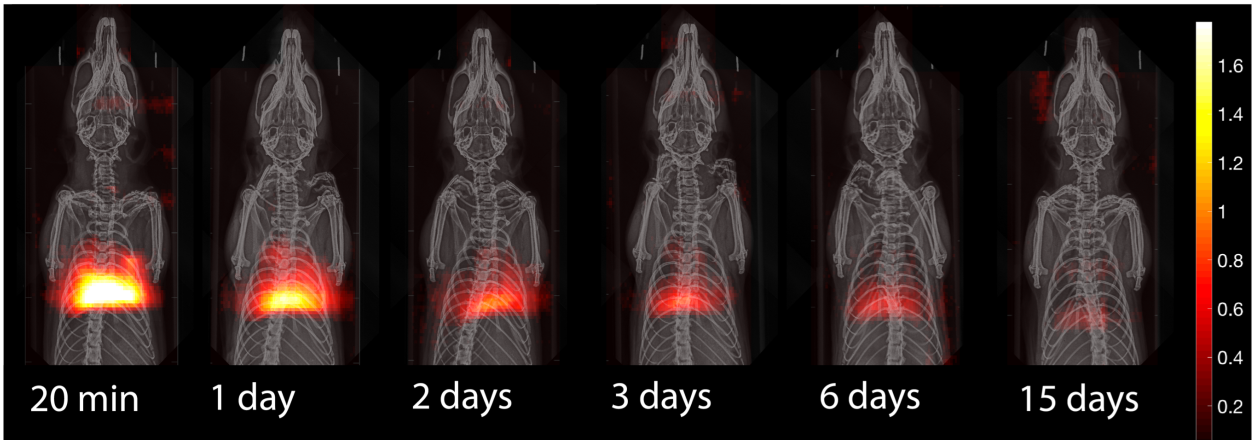

Figure 2.8: **MPI ventilation scans via aerosolized SPIOs over 15 days.** Inhaled SPIOs are seen in the lung airways and clear slowly out of the airways over days via the mucociliary pathway. MPI scans are coregistered to x-rays. Colorbar in µg Fe/mm^2.

intubation, which is excerbated by the small size of rats compared to larger animal models or humans.

2.5 Discussion

MPI lung ventilation/perfusion (V/Q) images are comparable in quality to that of nuclear medicine V/Q: contrast is excellent since there is no tissue background signal in either modal-

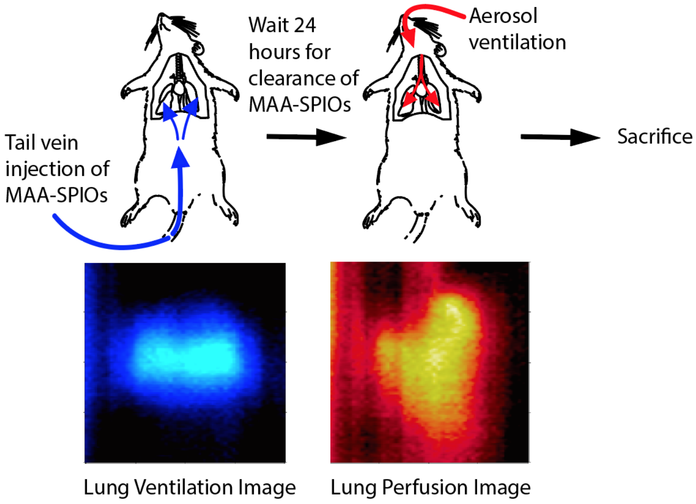

Figure 2.9: **MPI Lung Ventilation/Perfusion Imaging.** The rat first receives MAA-SPIO for MPI lung perfusion imaging. After 24 hours, the rat receives aerosolized SPIOs for MPI lung ventilation imaging. Streaking artifacts on the left edge are apparent as a result of imperfect respiratory gating.

ity, and high sensitivity allows for a 700,000 MAA-SPIO dose, within the range of clinical doses recommended by commercial MAA manufacturers for V/Q scans [60, 90, 97]. Both MPI and V/Q have relatively lower spatial resolution – roughly 1.5 mm and 3 mm respectively – compared to the <0.5 mm spatial resolution available for the latest CT scanners, but V/Q and CTPA have similar diagnostic power for PE because nuclear medicine provides superior contrast [41, 17, 78]. Regardless, MPI resolution can and is being improved rapidly with the continued development of MPI-optimized SPIOs, higher gradient scanners, and computational approaches such as frequency based MPI and deconvolution [8, 41, 42, 27, 46, 109]. Because an improvement in resolution implies a reduction in voxel size and therefore a reduction in signal per unit volume, clinicians will have to carefully balance the tradeoffs of resolution and SNR for each imaging application.

The novel MPI lung perfusion imaging agent, MAA-SPIO, shows promise for mimicking the pharmacokinetics of commercial MAA. Commercial suppliers report a 20:1 lung to liver ratio of ^{99m}Tc-MAA immediately post-injection in humans, while we report a 9:1 lung to liver ratio in rats [60, 97]. Additionally, commercial supliers report a clearance half-life from the lungs to the liver of approximately 2-4 hours in humans, while we report a 4.8 hour half-life in rats [60, 97, 90]. While results from humans and rats are not directly comparable, since both the SPIOs and radionuclides are several orders of magnitude smaller than the micron-sized MAA particles, we expect that these differences are more due to variations in commercial and in-house MAA manufacture rather than inherent differences in MAA-SPIO and ^{99m}Tc-MAA pharmacokinetics.

Image quality is not the only consideration in determining an appropriate imaging modality for differential diagnosis of PE; speed and safety are also essential. While it is difficult for any imaging modality to match the unparalelled speed and resolution of X-ray CT imaging, patients who require V/Q instead of CTPA because of iodine contraindication can face a 2+ hour wait time due since ^{99m}Tc-MAA must be prepared immediately before use due to the rapid half-lives of nuclear medicine tracers [50, 32]. In contrast, MAA-SPIOs are stable after preparation and we anticipate that MPI scan times will be comparable to MRI for 3D scans and up to two orders of magnitude faster for 2D scans [43, 35, 70]. Moreover, fully electronic methods of scanning the entire FOV can greatly speed up the scan time of MPI, while new reconstruction techniques can allow online-capable reconstruction times [98]. Previously, [154] covered a field of view of 20.4 × 12 × 16.8 mm^3 (to image a beating mouse heart) with temporal resolution of 21.5 ms. The parametric trade-offs in MPI of SNR, resolution and imaging time must be balanced carefully for each imaging application. The superior safety of MPI V/Q imaging for PE diagnosis is notable in two areas: there is zero ionizing radiation (unlike CTPA and nuclear medicine V/Q) and the tracers clear through routes independent of the kidneys (unlike iodine in CTPA), which is safer for patients with poor renal function [86].

This work on MPI lung ventilation/perfusion imaging adds to previous work on MPI preclinical imaging in the torso region, including on lung ventilation, whole body blood pool imaging and whole body stem cell tracking (showing 200 cell sensitivity) [96, 62, 158, 157]. Collectively, the high quality images and range of applications demonstrated in the literature suggest the general utility of MPI for lung imaging. Future work to add functional information to MPI lung imaging via new MPI contrast methods (i.e., “color” MPI) is of particular interest to the field [108, 53].

2.6 Conclusion

We successfully fabricated the first MPI lung perfusion imaging agent, MAA-SPIOs, with comparable morphology, size distribution and *in vivo* biodistribution and clearance compared to the ^{99m}Tc-MAA used in lung perfusion scintigraphy and SPECT studies. MAA-SPIOs carry the advantage of signal stability after preparation, whereas ^{99m}Tc must be conjugated to MAA immediately before use due to the short six-hour half-life of ^{99m}Technetium [50]. Hence, a MAA-SPIO imaging study could rapidly and conveniently be ordered by the clinician.

We demonstrated for the first time high sensitivity and high contrast 3D images of lung perfusion *in vivo* rats using this novel MAA-SPIO agent, confirming the targeting properties of MAA-SPIOs via *ex vivo* MPI scans of excised lung, liver and spleen. The 1.5 mm full-width at half-maximum resolution is comparable to V/Q studies and can be improved to 200 µm by the use of higher gradients, albeit with a direct loss in SNR (and therfore sensitivity), or nanoparticles optimized for MPI [41].

We also paired the perfusion scan with a previously published method for lung ventilation imaging. Inhaled aerosolized SPIOs localize immediately to the lung airways and clear through the mucociliary pathway over days. While MPI cannot currently distinguish between tracers in the airways and tracers in the lung capillaries, we demonstrated that both could still be imaged independently *in vivo* rats. We performed the perfusion study first, then waited 24 hours for the MAA-SPIOs to clear before performing the ventilation study with aerosolized SPIOs. Based on the MAA-SPIO clearance time course shown in Fig. 2.4, the two studies could potentially be performed in a shorter time period with only a two hour wait in between ventilation and perfusion scans. Alternatively, the signal from the initial scan could be subtracted out, with a technique described by our group in Yu *et al.* (2017) [156].

This proof-of-concept study suggests that MPI may be uniquely suited for accurate and safe diagnosis of life-threatening lung conditions such as PE. Importantly, MPI has superior safety characteristics over the current recommended imaging modalities of CTPA and V/Q scintigraphy or SPECT since no ionizing radiation is used. Additionally, SPIO tracers are thought to be better tolerated by patients with poor renal function compared to the CTPA contrast agent iodine [86].

This proof-of-concept work on healthy rats demonstrates promise for pairing MAA-SPIOs and aerosolized SPIOs with the superior safety of MPI imaging to someday offer completely iodine and radiation-free, robust lung ventilation/perfusion images with good convenience, cost and safety.

Chapter 3

MPI White Blood Cell Imaging

3.1 Attribution

The work described on white blood cell tracking was done in collaboration with K. L. Barry Fung, Prashant Chandrasekharan, David Mai, Kenneth E. Jeffris and Steven M. Conolly. The work described on assessing cell viability in MPI was done in collaboration with Caylin Colson, Zhi Wei Tay, Daniel Hensley, K. L. Barry Fung, Elaine Y. Yu, Bo Zheng and Steven M. Conolly.

3.2 Introduction

Inflammation refers broadly to the tissue response to injury, while infection implies the presence of microorganisms in causing the injury [161]. The inflammatory reaction may result from trauma, foreign particles (including microorganisms), ischemia and tumors. Tracking immune activity is of broad utility for diagnostic and treatment decisions in inflammation, as well as for deciphering innate immune cell biology [68].

White blood cell (WBC) imaging is a technique in nuclear medicine for imaging infection and inflammation, most commonly used in cases of suspected osteomyelitis [82]. This technique most frequently refers to when white blood cells are isolated from patient blood, labeled with radionuclides (usually Indium-111 Oxine (In111) or Technetium-99m Hexamethylpropyleneamine Oxine (HMPAO)) and reinjected into the patient for cell tracking, as shown in Fig. 3.1. Hence, the innate homing ability of white blood cells to sites of inflammation is used as a localization mechanism. Other methods that do not require cell isolation are also in use, such as Gallium-67 Citrate (Ga67-Citrate) and Fluorine-18 Fluorodeoxyglucose (18F-FDG). These depend on the physiological uptake of particularly sized imaging agents or biological molecules conjugated to radionuclides. The physiological uptake of In111-WBCs, Ga67-Citrate and 18F-FDG all varies somewhat, and different agents are preferred depending on the location of the suspected pathology.

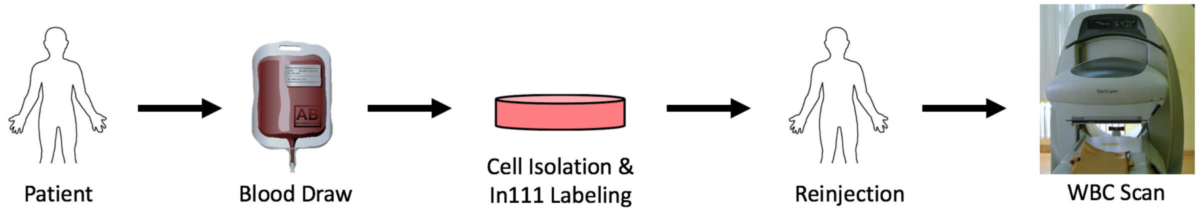

(a) Clinical In-111 WBC imaging procedure.

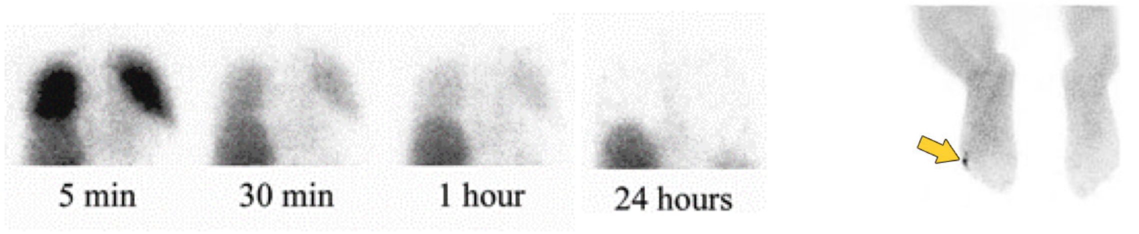

(b) WBC imaging in a healthy adult.

(c) WBC imaging of infected toe.

Figure 3.1: **Clinical WBC Imaging.** (a) Clinical WBC imaging procedure. Blood is drawn from the patient, then WBCs are isolated, labeled with radionuclides, and reinjected into the patient. This process takes 3-4 hours. The patient is generally imaged a day after cell infusion. (b) WBC imaging in a healthy adult [83]. Cells are initially caught in the lungs and clear to the liver and spleen. Hence, patients are generally imaged on the second day so that there are less confounding factors and the cells have time to home to sites of inflammation. (c) WBC imaging of an infected toe. In this example, a toddler has osteomyelitis in a toe of the left foot [152].

Beyond the traditional uses of WBC imaging for imaging of infection and inflammation, interest in imaging therapeutic, engineered WBCs is growing. Development of cell-based therapies, particularly adoptive immunotherapy, has skyrocketed over past several years. Despite dramatic successes, immunotherapies typically remains the final treatment option after surgery, radiation, and chemotherapy are no longer showing marginal benefits. This is due to the uncertain long-term prognosis and risks of toxicity [61, 58]. Toxicities such as cytokine release syndrome – a systemic uncontrolled inflammatory response – or ”on-target/off-tumor” recognition – in which healthy organs are targeted along with the tumor – can be life-threatening [11]. The ability to localize the distribution and viability of the administered cells *in vivo* would help answer questions on the mechanisms behind efficacy and toxicity [65]. Current studies of cell persistence *in vivo* have largely been performed in preclinical models [103] using *in vitro* assays.

While nuclear medicine techniques for white blood cell tracking are the most established, magnetic resonance imaging (MRI) and optical techniques have also been studied extensively. Of these, only MRI is useful for human studies. Due to the fundamental physics limitations of light absorption and scattering, particularly in the fluorescence wavelengths commonly used for cell tracking, light only penetrates several micrometers through tissue [68]. As a result, only surface structures in humans or small animals can be imaged optically. In contrast, the magnetic fields used in MRI are able to penetrate completely through a human body. For MRI cell tracking, the cells are labeled with SPIOs to generate T2* contrast. Either the cells can be prelabeled and infused into the animal or patient, or the SPIOs can be directly injected for uptake by cells *in situ.* The technique can be very sensitive, generating roughly 500-cell sensitivity in certain homogeneous tissues such as the brain [39]. However, the negative contrast mechanism – meaning that labeled cells appear as dark signal dropouts – is problematic in tissues that already appear dark on MRI, such as the lungs. Cell number quantification *in vivo* is therefore difficult and unreliable in many tissue types. Other labeling agents have been explored to generate positive contrast in MRI, such as Gadolinium (Gd) based agents or perfluorocarbons (PFCs) [68]. Concerns have grown about the toxicity of Gd-based agents and the cell labeling process has been challenging. In contrast, the use of PFCs for cell labeling is growing. PFCs are used for ^{19}F MRI as opposed to traditional ^{1}H MRI. While both methods can be performed on the same MRI scanners, ^{19}F MRI produces an image of only the labeled cells since fluorine is not naturally present in biological tissues [128]. Accurate quantitation of cells is therefore straightforward. However, even in recent work the sensitivity of ^{19}F MRI is still limited to 25,000 cells in pellets, and would likely to be lower *in vivo* [88].

Both MRI and MPI carry similar advantages as radionuclide-free modalities: they are safer, more convenient since on-site hot chemistry facilities are not needed, and are enabling for long-term imaging since the non-radioactive tracer does not undergo signal decay. However, MPI cell tracking carries further advantages, in particular an exceptional sensitivity of 200 cells in a voxel [157, 158]. This exceptional sensitivity, coupled with the quantitative nature of MPI and the positive contrast mechanism, makes MPI particularly well-suited for cell tracking. MPI has also been shown to generate different types of contrast depending on the type of nanoparticle used, suggesting the potential to monitor functional aspects of the cell using MPI [21]. This is particularly relevant for the development of live cell therapeutics; for instance, the viability, differentiation status, tumorigenicity and immunogenicity are all aspects of stem cell function essential to their regenerative potential *in vivo* [121].

Broader challenges remain in the non-specific nature of clinical immune cell imaging, and effectively distinguishing infection versus other types of inflammation remains an open research question [124, 117, 84]. Some of the therapeutic cell types in development, such as T-cells, are also relatively difficult to label effectively because of their low phagocytic ability and high division rate [140, 128]. The myriad of open challenges in inflammation imaging and cell tracking suggest that MPI WBC cell tracking is unlikely to be a silver bullet for these applications. Nonetheless, MPI has several compelling characteristics for cell tracking, and hence for white blood cell imaging of inflammation. In particular, the high sensitivity, positive contrast and lack of radioisotopes and ionizing radiation in MPI potentially allows for the tracer image achievable via nuclear medicine with the safety and convenience of MRI.

In this chapter, I describe optimization of MPI WBC labeling in a macrophage cell line with iron oxide nanoparticles, tracking a macrophage cell line *in vivo* healthy mice, and initial work attempting to image inflammation *in vivo* mice and to assess cell viability *in vitro*.

3.3 Methods

Optimization of Macrophage Labeling

NR8383 rat alveolar macrophage cells from ATCC (Rockville, MD) were cultured in Ham's F12K medium (ThermoFisher Scientific, Waltham, MA) supplemented with 15% heat-inactivated fetal bovine serum (ThermoFisher Scientific, Waltham, MA). RAW 264.7 mouse macrophage-like cells from the UCB Cell Culture Facility (Berkeley, CA) were cultured in Dulbecco's Modified Eagle's Medium (Corning, Manassas, VA) supplemented with 10% heat-inactivated fetal bovine serum (ThermoFisher Scientific, Waltham, MA). Cells were incubated overnight with either VivoTrax (Magnetic Insight, Alameda, CA) or perimag-COOH, perimag-NH2, synomag-COOH, synomag-NH2, or synomag-PEG (micromod Partikeltechnologie GMbH, Rostock, Germany) at an iron concentration 100 μg/mL. For dose response experiments, cells were incubated overnight with VivoTrax at an iron concentration of 0, 100, 200 or 1000 μg/mL. Nanoparticle size and zeta potential in DI water were characterized using dynamic light scattering on a Malvern Zetasizer Nano ZS (Malvern Panalytical, Malvern, Worcestershire). Cells were spun down at 0.2 RCF for 3 minutes, the supernatant containing free SPIOs was aspirated out, and the pellet was resuspended in phosphate-buffered saline. 100,000-3,000,000 cells were then spun down into a 40 μL pellet for measurement of MPI signal strength and resolution in UCB's arbitrary waveform relaxometer (AWR) [134]. All measurements were taken with a sinusoidal drive field frequency of 20.225 kHz, an excitation strength of 40 mTpp. A bias field from -60 mT to 60 mT is applied throughout the scan; the resulting point-spread-function (PSF) mimics the line profile through the scan of a point source in a 2D or 3D scanner. Propidium iodine staining (Invitrogen, ThermoFisher Scientific, Waltham, MA) was used to determine cell viability via flow cytometry using the Attune NxT Acoustic Focusing Cytometer (Life Technologies, Carlsbad, CA). Labeled cells were imaged under brightfield microscopy using the Zeiss Axio Observer inverted microscope (Oberkochen, Germany).

MPI Macrophage Tracking in Healthy Mice

RAW 264.7 cells were cultured as described above. Labeling was achieved by incubating the cells overnight with VivoTrax (Magnetic Insight, Alameda, CA) superparamagnetic iron oxide (SPIOs) tracers. Iron labeling was verified with Prussian Blue staining (Sigma-Aldrich, St. Louis, MO). C57BL/6 mice received a tail vein injection of 8 million SPIO-labeled RAW 264.7 cells. All animal procedures were conducted to the National Research Council's Guide for the Care and Use of Laboratory Animals and approved by UC Berkeley's Animal Care and Use Committee. Live animals were imaged under isoflurane anesthesia (2%, 1.5 L/min).

MPI 2D projection time course images were taken with the UCB home-built 6.3 T/m field free line (FFL) scanner over six hours [156]. The FFL is created and shifted electromagnetically. The scanner has a drive field frequency of 20.225 kHz and an excitation strength of 40 mTpp. All images were reconstructed using an x-space MPI reconstruction algorithm [41]. X-rays for anatomical reference were taken using a Kubtec XPERT 40.

Induction and Verification of Inflammation

Inflammation was induced in 6-10 week BALB/c mice using a subcutaneous injection of either 10 μg or 50 μg lipopolysaccharides from Escherichia coli O111:B4 (product # L4391, lot # 088M04067V) Sigma-Aldrich, St. Louis, MO) in the right flank. To validate inflammation, 100 μL of Rediject Inflammation Probe (PerkinElmer, Waltham, MA) was injected intraperitoneally to visualize neutrophil activity and 200 μL of 2.5 mg/mL lucigenin (Cayman Chemicals, Ann Arbor, MI) in 0.9% phosphate buffered saline (PBS) was used to visualize macrophage activity. Neutrophil and macrophage activity were imaged using the IVIS Lumina VivoVision as per Rediject Inflammation Probe manufacturer instructions and as per Tseng and Kung for lucigenin [144].

MPI Macrophage Tracking in Inflamed Mice

RAW 264.7 cells were cultured as described previously and labeled via incubation overnight with perimag-NH2 at a concentration of 250 μg/mL (micromod Partikeltechnologie GMbH, Rostock, Germany). Cell viability assessed with Trypan Blue (ThermoFisher Scientific, Waltham, MA) staining and iron labeling was assessed with the AWR. 7 million cells/100 μL PBS was infused into BALB/c mice. MPI imaging was performed as described earlier in the section on MPI macrophage tracking in healthy mice.

Optical Macrophage Tracking in Inflamed Mice

RAW 264.7 cells were cultured as described previously and labeled with VivoTrack 680 (PerkinElmer, Waltham, MA) as per manufacturer instructions. Three 9 week old BALB/c mice received a subcutaneous injection of 50 μg LPS at a concentration of 1 mg/mL in the right flank. On the same day, 8 million cells in 100 μL PBS at 82% viability by Trypan Blue staining were infused into mice via tail vein injection. Animals were imaged using the IVIS Lumina VivoVision at 6 hrs, 1 day, 2 days and 3 days post-injection with VivoTrack 680 manufacturer suggested imaging settings.

Induction and Measurement of Cell Death

RAW 264.7 cells were cultured as described previously and labeled via an overnight incubation with VivoTrax at a concentration of 100 μg Fe/mL. Cell death was induced by the addition of 0 μM, 1000 μM or 2000 μM etoposide (E1383, Sigma-Aldrich, St. Louis, MO).

Lyophilized etoposide was reconstituted in dimethyl sulfoxide (DMSO) at 4.25M and the stock was diluted into PBS before addition into culture. After harvest, aliquots of each sample were labeled with Annexin V and Propidium Iodide (V13241, ThermoFisher Scientific, Waltham, MA) for flow cytometry measurements of apoptosis and necrosis on the Attune NxT Acoustic Focusing Cytometer (Life Technologies, Carlsbad, CA). The remaining cell samples were spun down into 40 μL pellets for AWR measurements as described earlier.

Additionally, a range of cell-free controls consisting of 5.5 mg Fe/mL stock VivoTrax diluted into different solutions were measured. AWR measurements were performed of 5 μL VivoTrax in 35 μL PBS, DMSO, 0.0425M etoposide diluted in 1% DMSO and 99% PBS, or RAW 264.7 cell culture media. Additionally, AWR measurements were performed of 10 μL VivoTrax in 30 μL of pH 0 solution, pH 14 solution, water or NR8383 media. Last, measurements were performed of 0.5 μL VivoTrax incubated in 39.5 μL of water or NR8383 media at room temperature over four days.

3.4 Results and Conclusion

Two general methods exist for labeling cells for cell tracking. One is prelabeling of cells (also known as *ex vivo* labeling), while the other is *in situ* labeling of cells *in vivo* [68]. In the former method, a population of purified cells is labeled with the tracer or contrast agent, then injected into the animal or patient. This allows for tracking of a known population of cells. In the latter method, the probe is directly injected into the animal or patient, and the probe is taken up by the cells of interest. This method is more convenient, but non-specific uptake may be more prevalent. I focus on the prelabeling method in my dissertation, but both methods are feasible with MPI.

Optimizing Macrophage Labeling

Nanoparticle uptake by cells is known to be influenced by nanoparticle size and charge [51, 64]. Generally, neutral particles show the poorest uptake, while both positively and negatively charged particles are more likely to be phagocytosed. These properties were investigated for several commercial SPIOS using DLS and are shown in Table 3.1. The nanoparticle cores for particles tested are polydisperse iron oxides, primarily magnetite. VivoTrax particles are coated with carboxydextran, while micromod particles are coated with dextran and then additional amine (NH2), carboxyl (COOH) or polyethylene glycol (PEG) groups.

Next, RAW 264.7 and NR8383 cells were labeled with the SPIOs and the MPI signal per cell, iron per cell, resolution change before and after labeling, and cell viability were measured. The two cell lines are both macrophage-like, but RAW 264.7 is mouse-derived and NR8383 is rat-derived. The results for NR8383 cells are seen in Fig. 3.2. With the exception of synomag-COOH, despite the range of hydrodynamic diameters (52-110 nm) and zeta potentials (-4 to 22 mV), the cell uptake is roughly 2-15 pg/cell for all nanoparticles.

Synomag-COOH had the greatest absolute value of zeta potential (-44 mV) and showed by far the highest MPI signal, but the resolution degraded to twice its value before labeling. Note that the iron loading is similar between VivoTrax and synomag-COOH, but the MPI signal for a given mass of iron varies between SPIOs. Resolution is measured as full-width-at-half-maximum (FWHM) of the point spread function (PSF). Further investigation showed that this effect was also seen as soon as synomag-COOH was diluted in cell culture media (data not shown), suggesting that the poor stability of the particles causes immediate aggregation and therefore deterioration of the particle resolution.

Labeling experiments were also repeated with RAW 264.7 cells, as shown in Fig. 3.4. RAW 264.7 cells showed fairly similar uptake patterns, but the amount of synomag-COOH labeling was reduced. This effect may be because RAW 264.7 cells are entirely adherent, while NR8383 cells grow partially adherent to the tissue culture surface and partially in suspension. The cells in suspension have additional surface area in contact with the labeling media, which facilitates nanoparticle uptake. However, it is unclear why this effect only occurs with synomag-COOH. Additionally, the RAW 264.7 cells labeled with VivoTrax and perimag-COOH show roughly 20% lower viability compared to NR8383 cells subject to the same labeling protocol. Peculiarly, synomag-COOH labeled RAW 264.7 show a particularly low viability of 38% compared to 98% viability in synomag-COOH labeled NR8383 cells. We suspect that the extremely high loading of synomag-COOH into NR8383 cells resulted in many dead cells with unusual morphologies, and these cells were gated out of the flow cytometry analysis. Gating is used to exclude debris or clusters of cells from flow cytometry analyses, but may also exclude unusually shaped cells.

Last, a dose response experiment comparing RAW 264.7 labeling when the cells were incubated with different amounts of VivoTrax was performed as shown in Fig. 3.5. Iron loading increases with higher concentrations of VivoTrax, but the cell viability decreases. The resolution also worsens slightly, possibly because SPIOs are more likely to aggregate at higher concentrations.

Under brightfield light microscopy, as shown in Fig. 3.3, the iron uptake of the cells can be visualized as a brown color. We can observe a loose correlation between the intensity of the color and the AWR measurements of iron loading for each SPIO type. Interestingly, microscopy reveals that there is significant variation in individual cell loading, and that there are localized areas of high iron uptake. This effect is particularly pronounced in the cells labeled with synomag-COOH. It is unclear why this effect occurs; potentially, electrostatic interactions between SPIOs may cause clustering of SPIOs, which could then lead to areas of high SPIO uptake.

Overall, we concluded that of the commercial SPIOs tested, most demonstrated a similar ability to label cells while preserving cell viability and particle resolution. We also tested whether 5 μg/mL of the trasfection agent protamine sulfate would influence VivoTrax labeling ability in NR8383 cells, but saw minimal differences in labeling despite the zeta potential change from -26 mV to -19 mV (data not shown).

	Z-Average (d nm)	**Zeta Potential (mV)**	**Polydispersity**
VivoTrax	52	-26	0.21
perimag-NH2	110.1	22.2	0.194
perimag-COOH	74.09	-15.2	0.183
synomag-NH2	48.32	-4.15	0.166
synomag-COOH	28.63	-44	0.038
synomag-PEG	42.12	11.1	0.052

Table 3.1: **Hydrodynamic Diameter and Zeta Potential of Commercial SPIOs.** DLS was used to characterize SPIOs for cell labeling from Magnetic Insight and micromod Partikeltechnologie. The hydrodynamic diameter, zeta potential and polydispersity index were measured.

MPI Macrophage Tracking in Healthy Mice

In Fig. 3.6, the mouse macrophage scan protocol is described and resulting MPI images overlaid onto X-ray anatomical reference are shown. The images show localization of IV-injected macrophages in the lung capillaries, followed by clearance to the liver and spleen. This kinetic behavior is expected in healthy patients and animals because the WBCs are comparable in size to the lung capillary size (roughly 6 microns). Overall, this preliminary test demonstrates that MPI is able to replicate cell tracking results from other modalities [31, 83] with excellent signal-to-noise and contrast-to-noise ratio.

Establishing a Mouse Model of Localized Inflammation with Lipopolysaccharides

Bacterial lipopolysaccharides (LPS) are commonly used for animal models of inflammation because of their potency [24, 1]. The toxin is the major component of the outer membrane of Gram-negative bacteria, but also is secreted from bacteria [113, 75]. However, LPS shows high batch-to-batch variability and mouse strains show high variability in response to LPS [146, 67]. Therefore, careful validation of LPS-induced inflammation is essential. The serotype O111:B4 was used as the inflammatory agent because it induces more rapid and severe inflammation compared to other LPS serotypes [93]. The luminol-based (5-amino-2,3-dihydro-1,4-phthalazinedione, sodium salt) Rediject Inflammation Probe and lucigenin (bis-N-methylacridinium nitrate) were used to visualize neutrophil and macrophage activity, respectively. Luminol bioluminescence results from a myeloperoxidase (MPO) mediated reaction, allowing for specific imaging of superoxide generated in the neutrophil phagosomes. Lucigenin bioluminescence results from the activity of phagocyte NADPH oxidase (Phox)

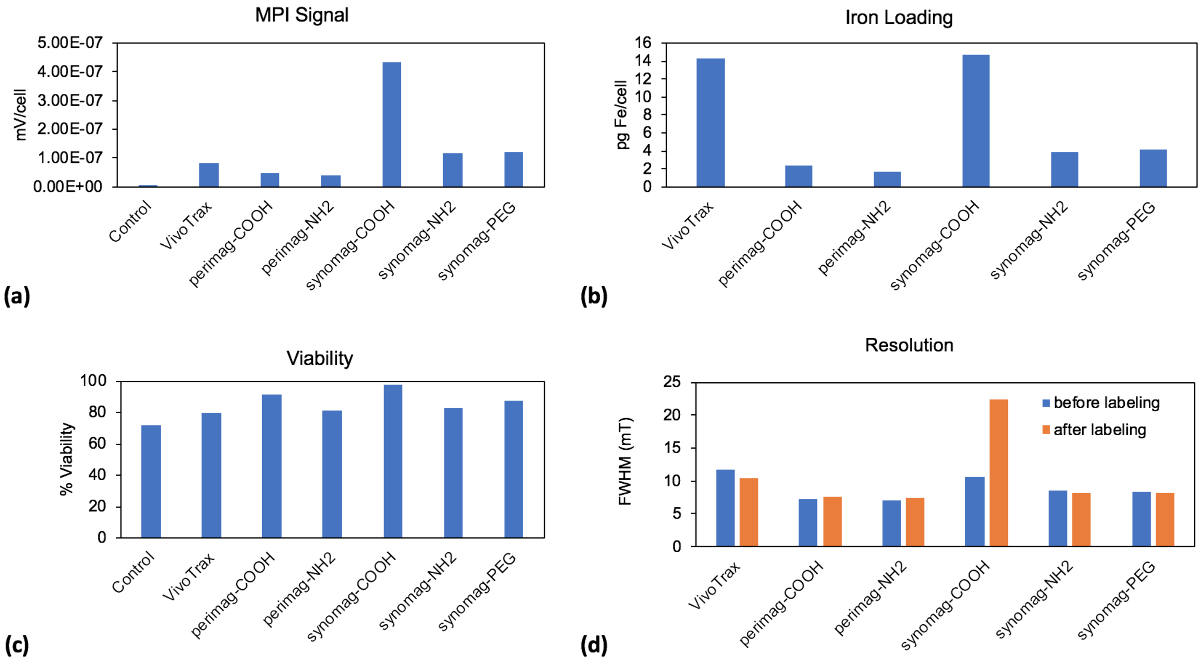

Figure 3.2: **Comparison of NR8383 cell labeling with different commercial MPI tracers.** (a) MPI signal of labelled cells, as measured on the arbitrary waveform relaxometer. (b) Iron content of labelled cells. The control cells are excluded from the analysis since the signal per gram iron is dependent on the SPIO type. Moreover, the raw MPI signal seen in the control is indistinguishable from noise and over an order of magnitude smaller than that of any labelled cells. (c) Cell viability, based on propidium iodide staining measured via flow cytometry. (d) Resolution of tracers before and after cell labeling.

in macrophages. As shown in Fig. 3.7, both 10 μg and 50 μg of LPS induce inflammation visible with luminol 24 hr after induction. However, 10 μg induces less inflammation and the associated neutrophil activity fades after the 24 hr time point. While luminol is useful to confirm the induction of acute inflammation, lucigenin can predict when our pre-labeled macrophages will track of the site of inflammation, since it visualizes macrophage activity. In Fig. 3.8, the higher and more persistent inflammatory response with 50 μg LPS as compared to 10 μg matches what was seen with the luminol. However, the response appears to higher up than the right flank location where LPS was injected, and in the case of 50 μg LPS, appears on both sides of the animal. We suspect that this may be due to uptake of LPS in the lymphatics and lucigenin may highlight corresponding macrophage activity there. We also compared three different vials of LPS of the same lot number from the same supplier, as shown in Fig. 3.9. While the center mouse shows both luminol (neutrophil) and lucigenin (macrophage) response at the site of inflammation, the other two mice either show luminol-only or lucigenin-only response. Qualitatively, the intensity of the responses also

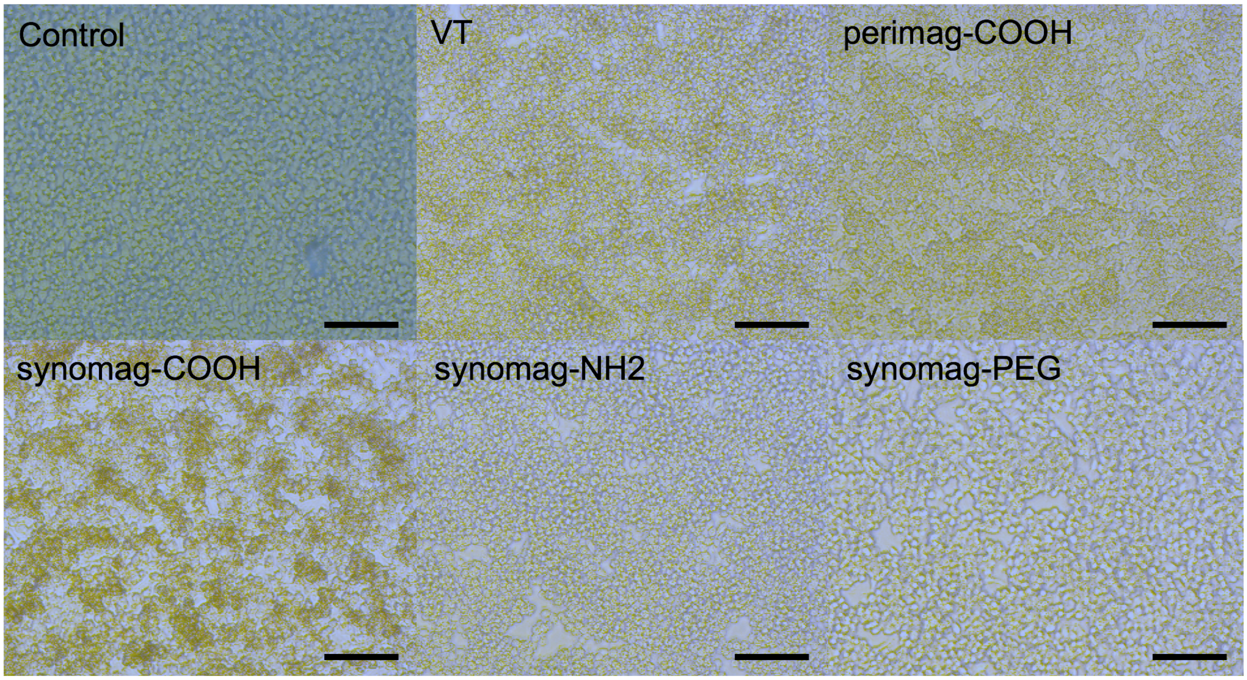

Figure 3.3: **Comparison of RAW 264.7 cell labeling under brightfield light microscopy.** Cells were imaged on the Zeiss Axio Observer inverted microscope after incubation with SPIOs overnight. The iron oxide nanoparticles appear as a brown color without the need for any other staining. Scale bar 100 μm.

varies. Since all vials are endotoxin tested by the supplier, this variation is thought to result from the potency of the LPS changing in storage. As a result, we endeavored to use the same vial of LPS throughout experiments and to freeze down aliquots if the reconstituted vial had not be used within a month.

MPI Cell Tracking in a Mouse Model of Inflammation

RAW 264.7 cells labeled with perimag-NH2 at an iron loading of 1.4 pg/cell, with a viability of 85%, were infused into inflamed mice for MPI imaging. In Fig. 3.10, a similar clearance pattern as to the healthy mice is seen, with initial lung uptake at 6 hrs and clearance to the liver and spleen afterwards. No uptake is seen at the site of inflammation. MPI signal seen outside of the mouse is thought to be due to the poor resolution of MPI cell labeling SPIOs relative to the small size of the mouse, which is exacerbated by resolution degradation post-labeling.

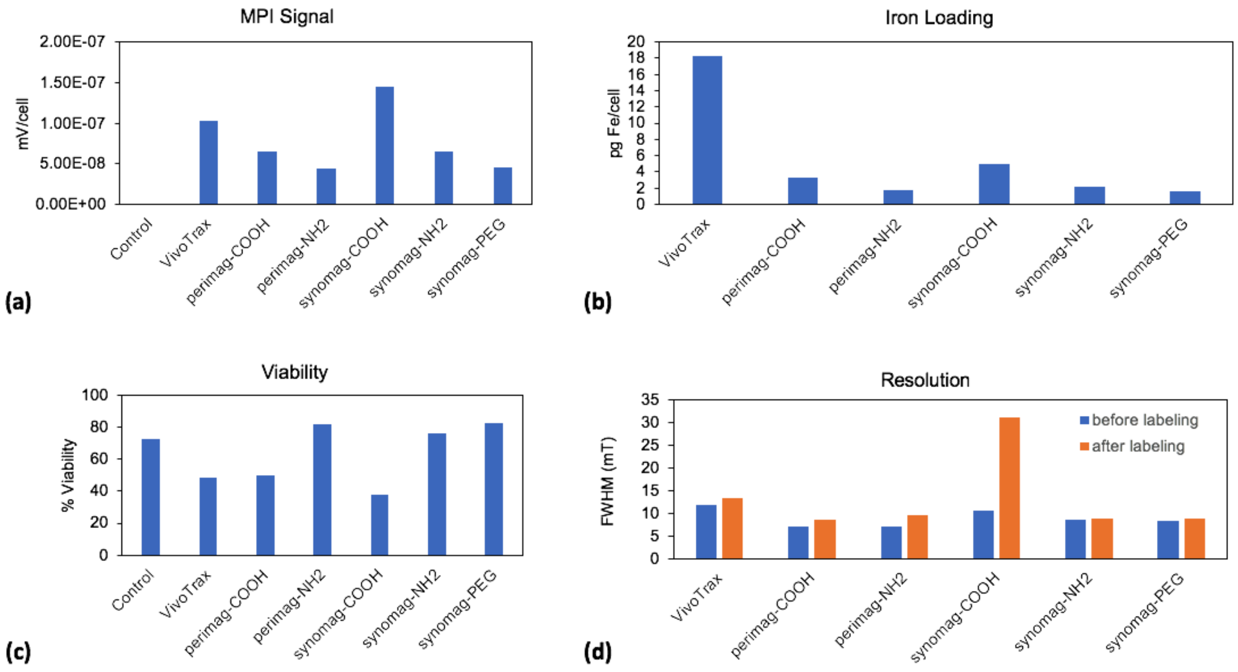

Figure 3.4: **Comparison of RAW 264.7 cell labeling with different commercial MPI tracers.** (a) MPI signal of labelled cells, as measured on the arbitrary waveform relaxometer. (b) Iron content of labelled cells. The control cells are excluded from the analysis since the signal per gram iron is dependent on the SPIO type. Moreover, the raw MPI signal seen in the control is indistinguishable from noise and over an order of magnitude smaller than that of any labelled cells. (c) Cell viability, based on propidium iodide staining measured via flow cytometry. (d) Resolution of tracers before and after cell labeling.

Optical Cell Tracking in a Mouse Model of Inflammation

Based on the MPI results, we wanted to evaluate whether the RAW 264.7 homing ability or the sensitivity of MPI was the source of the negative results. The peak macrophage influx may account for only 0.4-2% of the total injected cells [102]. Hence, we used VivoTrack 680, a commercial optical cell tracking reagent for IVIS imaging, which has been shown to have a sensitivity of < 20,000 cells. After inflammation was induced in the right flank of BALB/c mice, VivoTrack 680-labeled RAW 264.8 cells were infused into the mice. We also confirmed induction of inflammation as described previously (data not shown). At six hours after cell infusion, initial uptake is seen in the lungs as expected, and at the 24, 48, and 72 hour time points afterwards, varying uptake is seen in the liver and spleen. No uptake is seen at the site of uptake on the right flank. Given the known sensitivity of IVIS/VivoTrack 680 and the cell viability (82%), this suggests that RAW 264.7 may not be sufficiently macrophage-like to home to the LPS site of inflammation. Alternatively, macrophage activity may not localize to the distal LPS site until the inflammation resolution phase, as has been shown in other

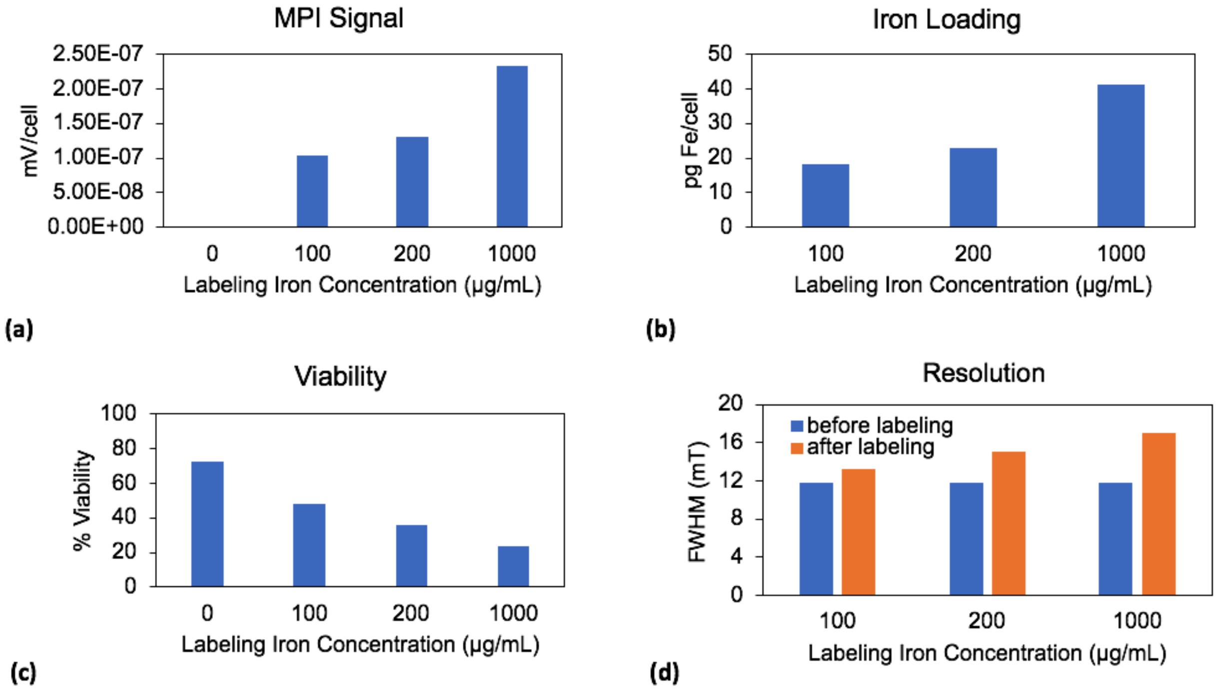

Figure 3.5: **Comparison of RAW264.7 cell labeling with different concentrations of VivoTrax.** (a) MPI signal of labeled cells, as measured on the arbitrary waveform relaxometer. (b) Iron content of labelled cells. The control cells are excluded from the analysis since the signal per gram iron is dependent on the SPIO type. The control cells are excluded from the analysis since the signal per gram iron is dependent on the SPIO type. Moreover, the raw MPI signal seen in the control is indistinguishable from noise and over an order of magnitude smaller than that of any labelled cells. (c) Cell viability, based on propidium iodide staining measured via flow cytometry. (d) Resolution of tracers before and after cell labeling.

work [1].

MPI Measurements of Cell Viability

In the cell tracking work shown above, it is unknown how long the cells remain viable post-injection. Poor viability may be one reason why the cells are not homing to the site of inflammation. Moreover, maintaining cell viability after administration *in vivo* is an important challenge for cell therapies [121]. Therefore, we examined the possibility of distinguishing cell viability based on the SPIO PSF. Previous work has shown that MPI can distinguish between viscosities in a biologically relevant range, and that intracellular viscosity increases after cell death [145, 74]. Intuitively, the nanoparticle would take longer to flip in a higher viscosity medium, resulting in a broader PSF.

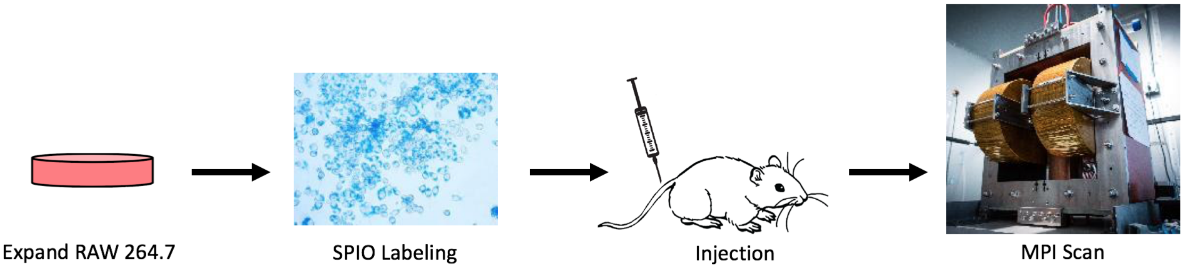

(a) MPI mouse macrophage scan procedure.

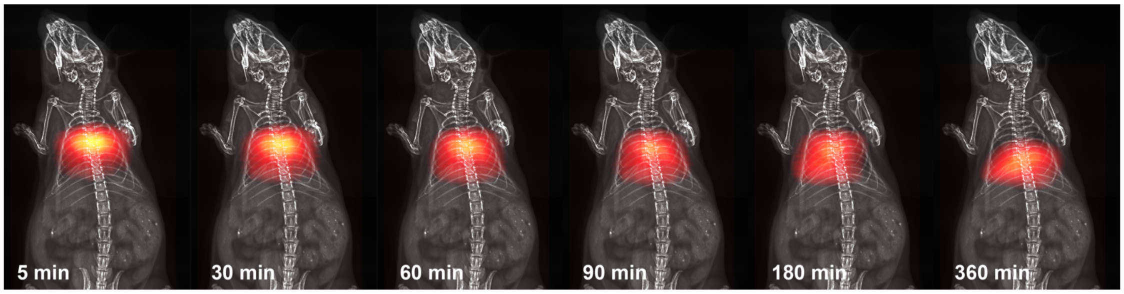

(b) MPI macrophage scans in a healthy mouse.

Figure 3.6: **MPI macrophage tracking in a healthy mouse:** (a) MPI mouse macrophage scan procedure. Similar to the procedure for clinical WBC scans, the macrophages are prelabeled with SPIOs with Prussian Blue stain confirmation of iron labeling (second image from left). The mouse is then injected with pre-labeled macrophages and imaged for six hours. (b) MPI macrophage scans of a healthy mouse (red colormap) overlaid onto X-ray anatomical reference. Initial localization in the lungs is observed, followed by a slow clearance to the liver and spleen.

Because there are many confounding factors that may influence the SPIO PSF, controls were run to evaluate the effect of the non-cell components of the experiment. As is evident from Fig. 3.12, certain components, such as dimethyl sulfoxide (DMSO), have a dramatic influence on the SPIO signal. The peak signal for the SPIO sample in DMSO is 30% that of the peak signal in PBS, and a broadening of the PSF is also seen. However, DMSO is only used for initial reconstitution of the etoposide used to induce cell death. Neither the presence of etoposide nor the lower concentration of DMSO present affect the SPIO signal in the etoposide sample, confirming that any changes in VivoTrax PSF in a population of dead cells as opposed to live ones would be due to changes in viability. A slight broadening and signal drop in the PSF of VivoTrax diluted in media are also observed.

Next, SPIO-labeled cells were treated with a chemotherapeutic agent to induce cell death and the resultant cell viability was quantified with propidium iodide staining (gold standard) and MPI (novel technique). Etoposide is a common chemotherapeutic agent that has previously been used to induce cell death in RAW 264.7 cells [147]. As shown in Fig. 3.13(b),

(a) 10 µg subcutaneous LPS injection

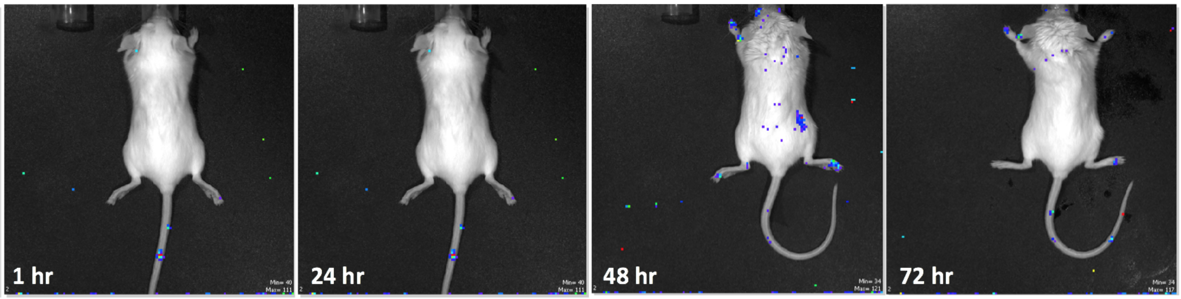

(b) 50 µg subcutaneous LPS injection

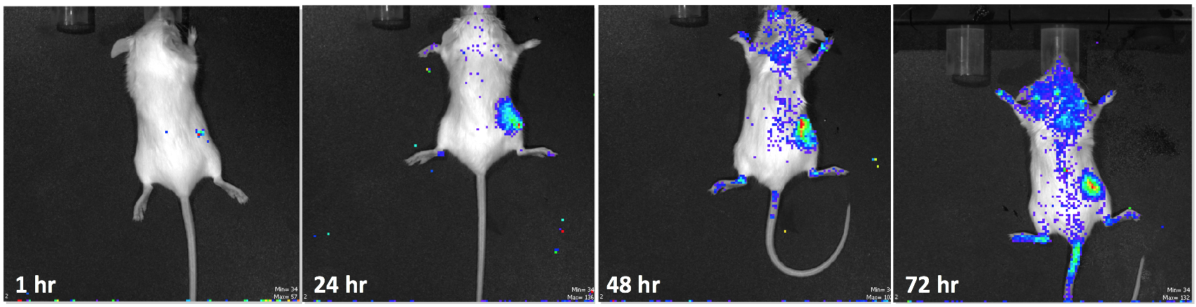

Figure 3.7: **Validation of Inflammation Model with Luminol.** (a) Response to 10 μg LPS over 72 hours. A response at the site of LPS administration is only seen at the 48 hour time point. (b) Response to 50 μg LPS over 72 hours. A mild response is seen 1 hour after LPS administration and a large response is seen thereafter.

while etoposide decreases cell viability, the effect is not dose-dependent at the concentrations tested. Moreover, SPIO labeling reduces absolute viability by about 20%. Therefore, we were only able to test if MPI could distinguish between viability differences of about 10%. As shown in Fig. 3.13(a) and 3.13(b), the PSF of the less viable cells appears to broaden very slightly, but it is unclear whether this effect is significant.

Successful SPIO labeling of a macrophage cell line and tracking of labeled cells in a healthy mouse were shown. Cell viability was $> 70\%$ with all commercial SPIOs tested, and iron loading was generally 5-15 pg Fe/cell. synomag-COOH showed extraordinarily high loading, but also a significant degradation of MPI resolution. Other SPIOs tested showed minimal ($< 10\%$) degradation in resolution (roughly 2X worse). In a healthy mouse, MPI imaging showed cell localization to the lungs and clearance through the liver and spleen over six hours, replicating a biodistribution pattern seen in other modalities. A mouse model of inflammation using a subcutaneous right flank injection of LPS serotype O111:B4 was validated in BALB/c mice with the optical inflammation activity agents luminol and lucigenin. However, MPI did not show any cells visible at the site of inflammation when SPIO-labeled RAW 264.7 cells were infused into a mouse with a site of LPS-induced inflammation. These results were confirmed in a higher sensitivity optical cell tracking study, suggesting that RAW

(a) 10 µg subcutaneous LPS injection

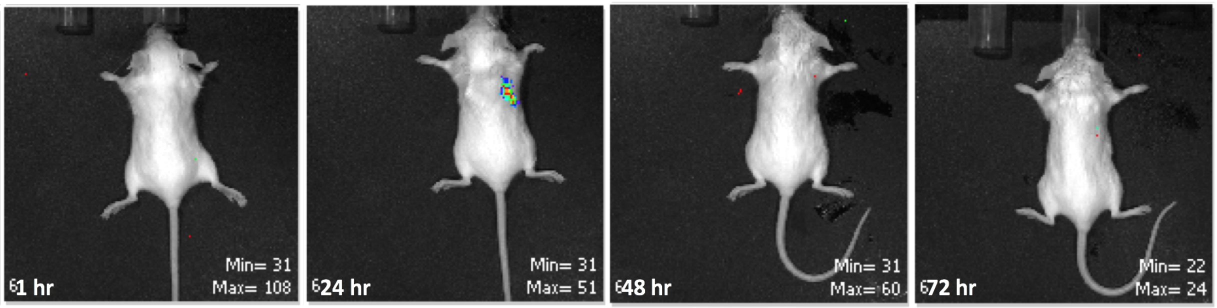

(b) 50 µg subcutaneous LPS injection

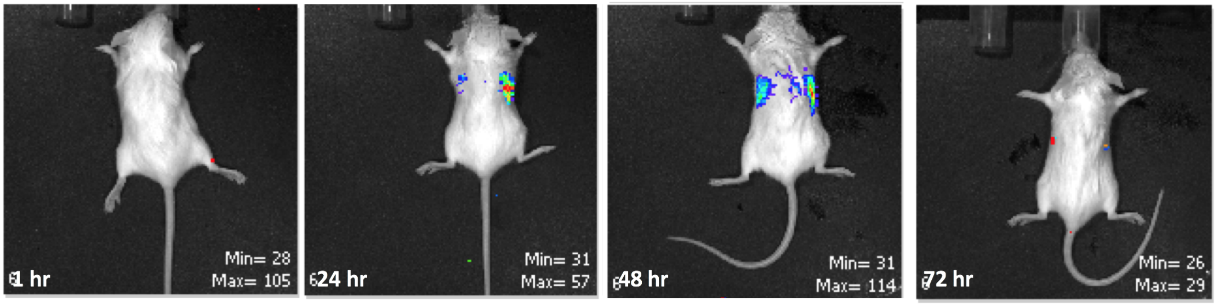

Figure 3.8: **Validation of Inflammation Model with Lucigenin.** (a) Response to 10 μg LPS. over 72 hours. A response is only seen at the 24 hour time point. (b) Response to 50 μg LPS over 72 hours. A response is seen at the 24 hr and 48 hr time points. Interestingly, the bioluminescence seen in both mice is higher up on the body than the site of LPS injection (right flank), and is seen on both sides of the animal in the 50 μg mouse, suggesting that lucigenin may be highlighting LPS uptake and macrophage activity in the lymphatic system.

264.7 cells may not home to sites of inflammation in the three days after LPS inflammation. We also assessed whether the PSF of SPIO-labeled cells correlated with cell viability. A chemotherapeutic agent, etoposide, was used to induce cell death. For a difference in absolute viability between treated and untreated cells of about 10%, very little change was seen in the PSF.

Future work will require longer monitoring of the animals to evaluate whether RAW 264.7 only localizes to the site of inflammation in the resolution phase of wound healing, as has been seen in other work [1]. To improve cell viability imaging of MPI, new SPIOs that show high uptake into cells and are highly sensitive to changes in viscosity are needed. Previous work has discussed these needs in more detail, but nanoparticles for this specific application are still in development [21].

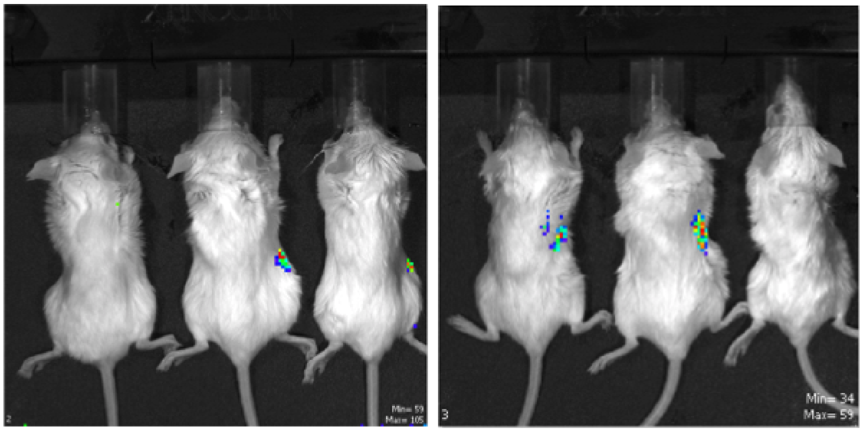

(a) Luminol Imaging **(b) Lucigenin Imaging**

Figure 3.9: **Batch-to-batch variation in LPS potency for inflammation induction.** (a) Neutrophil (luminol) response to 50 μg LPS from three different vials, 24 hours after LPS administration. (b) Macrophage (lucigenin) response to 50 μg LPS from different vials, 24 hours after LPS administration.

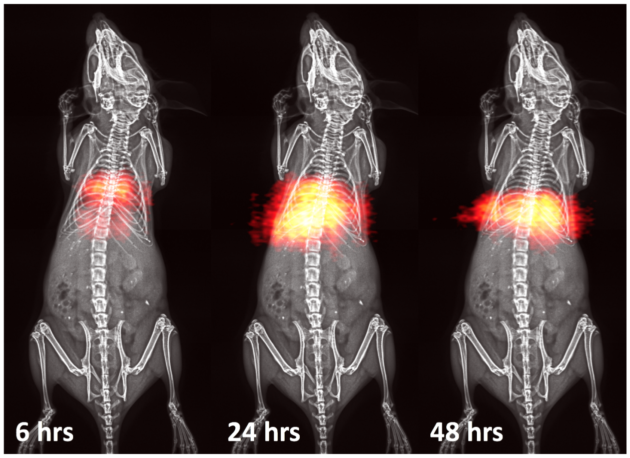

Figure 3.10: **MPI cell tracking in a mouse model of inflammation.** MPI projection images (hot colormap) are overlaid onto X-ray anatomical reference (grayscale). Six hours post cell infusion, mice show accumulation of RAW 264.7 in the lungs. At 24 hours and beyond, varying clearance to the liver and spleen is seen. No uptake is seen in the site of inflammation is on the right flank.

3.5 Discussion

Macrophages exhibit phagocytosis, but many other immune cells of interest, such as T-cells, are non-phagocytic [140]. Non-phagocytic cells uptake an order-of-magnitude less SPIOs

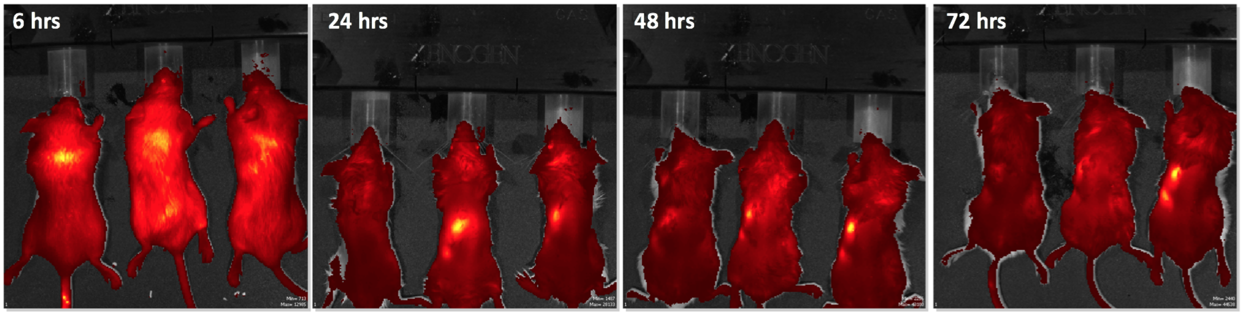

Figure 3.11: **Optical cell tracking in a mouse model of inflammation.** Six hours post cell infusion, mice show accumulation of RAW 264.7 in the lungs. At 24 hours and beyond, varying clearance to the liver and spleen is seen. No uptake is seen in the site of inflammation is on the right flank.

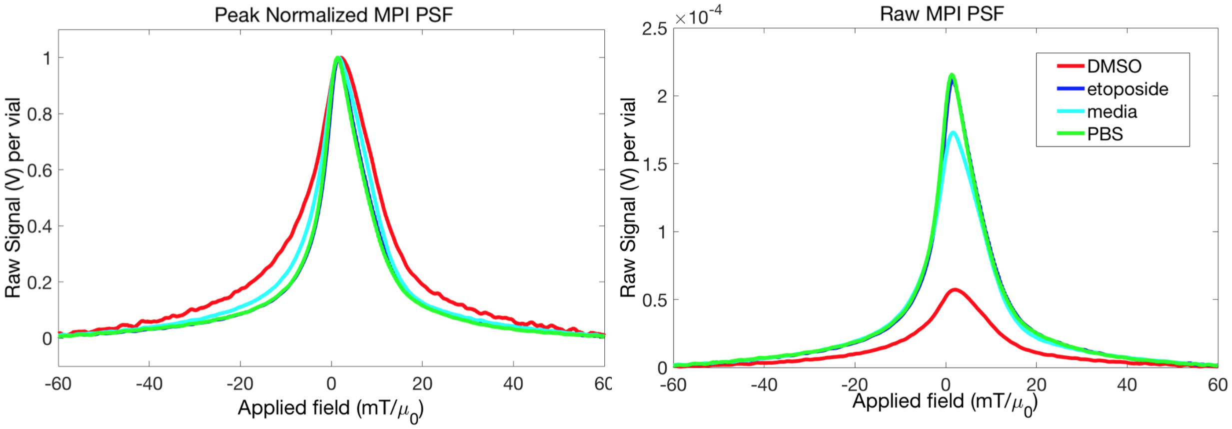

Figure 3.12: **Effect of Experimental Reagents on VivoTrax PSF.** AWR measurements of VivoTrax diluted in various reagents. Applied field is in units of milliTesla/vacuum permeability (mT/mu_0). Raw signal is in units of Volts (V). (LEFT) Peak normalized MPI PSF. Changes in the SPIO resolution can be easily observed in this graph. (RIGHT) Raw MPI PSF. Changes in the peak SPIO signal/mass of iron can be easily observed in this graph. VivoTrax in DMSO: FWHM = 16.7 mT, peak signal = 0.05671 mV. VivoTrax in etoposide: FWHM = 10.7 mT, peak signal = 0.21186 mV. VivoTrax in media: FWHM = 13.1 mT, peak signal = 0.17361 mV. VivoTrax in PBS: FWHM = 10.7 mT, peak signal = 0.21454 mV.

compared to phagocytic cells, greatly decreasing SNR. Moreover, autologous cells rather than allogenic cell lines are often preferred for both diagnostic and treatment applications due to the reduced immunogenicity [76]. While the increased immunogenic potential of allogenic cells may be desired for certain treatments, the alloimmunity mechanism – that is, that the host may recognize the donated cells as non-self and reject them – reduces the

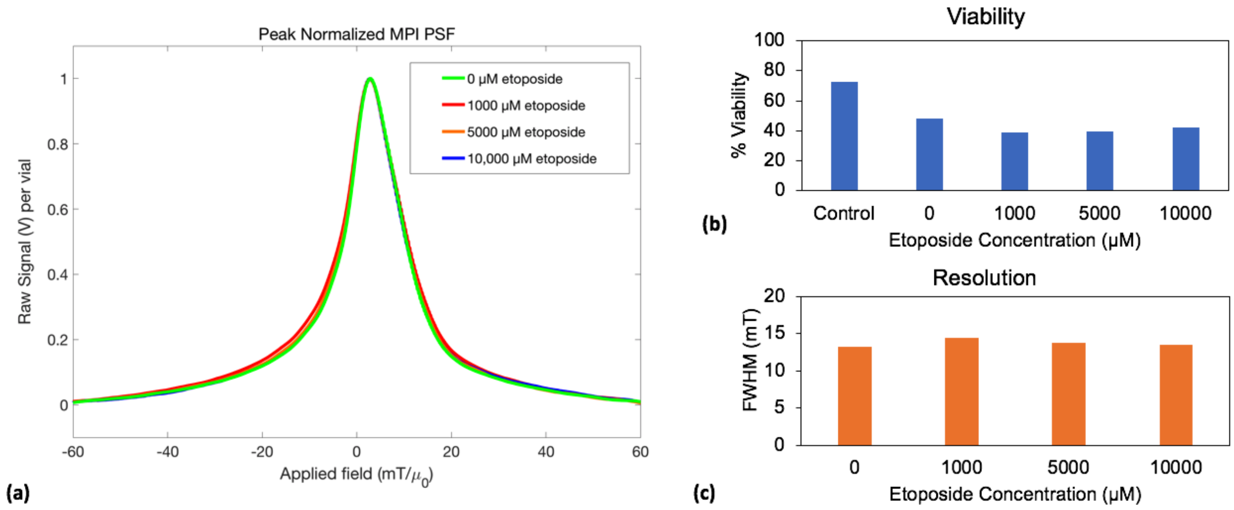

Figure 3.13: **Effect of Cell Viability on VivoTrax PSF.** (a) AWR measurements of labeled cells treated with different amounts of a chemotherapeutic agent (etoposide) to induce cell death. Applied field is in units of milliTesla/vacuum permeability (mT/mu_0). Raw signal is in units of Volts (V). (b) Viability (according to propidium iodide staining) of VivoTrax-labeled cells treated with etoposide. The control is not labeled with VivoTrax. (c) Resolution of labeled cells treated with different amounts of etoposide.

specificity of the response to the disease target. Additionally, the RAW 264.7 cells used in our studies are an immortalized macrophage-like cell line which has some cancerous characteristics and generally reduced resemblance to normal macrophage physiology [9]. Each step towards using immune cells that most closely resemble the animal or patient's own cells, from immortalized allogenic cell lines to finite allogenic cell lines to autologous cells in primary culture, increases the complexity of the process and the difficulty of acquiring a high number of cells [89]. Therefore, future work must contend with the challenges of acquiring sufficient physiologically relevant and safe cells and labeling for high SNR imaging in a realistic timeframe.

While we did attempt autologous cell isolation, we were only able to acquire about 150,000 monocytes from a single mouse spleen after a 30 minute isolation process, and about 200,000 neutrophils from 2 mL of mouse blood after a 4 hour isolation process, using magnetic bead isolation kits from Stem Cell Technologies (Vancouver, Canada) and Miltenyi Biotec (Bergisch Gladbach, Germany). Given that previous work showed that peak macrophage influx into a site of inflammation was only 0.4-2% of the total injected cells, only 600-4000 cells would be expected to home to the site of inflammation given our cell yields [102]. While our group has previously shown a 200 cell detection limit (SNR 1), that work was performed with stem cells that phagocytosed 2-10X more iron and refers to the sensitivity of a cell phantom concentrated in a single voxel volume of 750 μL [158]. In a live animal, a site of inflammation is unlikely to be concentrated into a single voxel and moreover exists in the context of clearance organs which uptake the majority of the injected cells, reducing the contrast. Increasing the sensitivity of MPI is therefore essential for the success of tracking pre-labeled WBCs to sites of inflammation.

In this work, the cell labeling techniques were limited to commercial SPIOs available. However, customized synthesis could include coatings (highly cationic or antibody-based) that would enable higher uptake for the cell type or interest, or iron oxide cores with higher MPI signal/Fe mass. For instance, the Krishnan group synthesized particles with 5X better signal-to-noise ratio compared to Resovist (also known as VivoTrax) and 2X better linear spatial resolution [29]. Alternatively, an *in situ* cell labeling technique – in which SPIOs are directly infused into the animal or patient and WBCs bind or uptake the SPIOs inside the body – would obviate the need for cell isolation and greatly speed up the process. Different antibody-based coatings can enable SPIO binding to specific WBC types. However, the specificity and safety of the antibody coatings are potentially of concern [131, 2, 151]. Both approaches require significant innovations in MPI nanoparticle technology.

Last, of note is that while bioluminescence and fluorescence was used in this work as a higher sensitivity modality which has commercial tracers available both to monitor metabolic activity and to label cells, the extraordinarily properties of optical imaging are only applicable for preclinical imaging in rodents. The depth penetration of light into biological tissue is merely several millimeters, so even in this mouse study the inflammation site had to be placed close to the surface of the animal [3]. At the low frequency magnetic fields used in MPI (20 kHz), there is no signal attenuation from tissue. Hence, while further work must be done to improve the sensitivity of MPI – especially for this application in which the iron dose is severely limited by the nanoparticle uptake by cells – the fundamental physics of MPI are highly promising for its clinical translation.

Chapter 4

Phospholipase Detection via MPI Relaxometry

4.1 Attribution

This work was done in collaboration with Prashant Chandrasekharan, Zhi Wei Tay and Steven M. Conolly.

4.2 Motivation

Interest in the ability to visualize and measure the function of biological and cellular processes *in vivo* – i.e., molecular imaging – has grown as imaging technology has enabled more advanced probing of diseases beyond the anatomy [105]. This enables earlier and more accurate diagnosis of diseases such as cancer without invasive techniques, and a more tailored and effective approach to treatment. For instance, molecular imaging has been used to predict which chemotherapeutic drugs might be most efficacious based on the receptors on breast tumors, without an invasive biopsy. White blood cell imaging to visualize inflammation and infection, as discussed in an earlier chapter, is one such molecular imaging technique. However, one technique at the forefront of molecular imaging is the use of activatable or switchable contrast mechanisms [79]. These tracers will turn "on" or "off" contrast based on some condition, such as probe binding or enzymatic activation. The ON/OFF mechanism enables both molecular contrast not otherwise possible and especially high CNR imaging. Most of the probes have been developed for preclinical optical imaging, but recent work has pushed these techniques to clinically used modalities, such as position emission tomography (PET) [148].

The physics of MPI enables similar contrast through several mechanisms. First, while the tracer is thought of as a superparamagnetic SPIO that responds instantaneously to the applied field, in reality there are relaxation mechanisms that influence the response – and hence the point spread function (PSF) – of the tracer [21]. The two relaxation mechanisms are called Néel and Brownian, in which the former refers to the realignment of the magnetic moment within the SPIO and the latter refers to the physical rotation of the SPIO such that the magnetic moment aligns with the applied field. The Brownian mechanism is influenced by the viscosity of the medium, while the Néel mechanism is not. In general, smaller particles exhibit mainly Néel behavior and are unaffected by the media viscosity or by binding. Larger particles exhibit mainly Brownian behavior and are sensitive to media viscosity and/or to binding events. The Néel and Brownian behavior is seen in the tracer PSF even in the standard sinusoidal MPI scanning scheme, but the contrast can be amplified via color or pulsed MPI scanning techniques [108, 136].

For MPI tracers to exhibit different MPI physics based on some environmental condition, therefore, the SPIO must exhibit Brownian behavior and it must have an environmentally responsive coating or carrier. Extensive work on functionalization of SPIOs has been performed for a variety of applications including molecular imaging, but also for triggered drug-release nanoparticles or highly-sensitive, point-of-care biosensors [56, 77]. Phospholipase A2 (PLA2) is a water-soluble enzyme overexpressed in many conditions including atheroschlerosis, breast cancer and prostate cancer [12, 16, 59]. For instance, PLA2 is overexpressed up to 22X in prostate cancer. Therefore, a sensitive, high-contrast mechanism to image PLA2 could serve as a tool to diagnose and localize various pathologies. Such probes have been attempted for optical imaging and 19F MRI [18, 47]. As noted by the authors, the optical technique may be best suited for intraoperative tumor margin imaging due to the background fluorescence and penetration depth challenges in optical imaging. The 19F MRI technique is highly promising since MRI is already in use for full-body clinical scanning and 19F imaging allows for positive contrast cell tracking. Preliminary work has shown that MPI may be more sensitive than 19F imaging [55], but both techniques have different strengths, highlighting the value of multimodality imaging.

In this chapter, I discuss a concept for PLA2-responsive nanocarriers in MPI, and initial work fabricating and testing such nanocarriers. I demonstrate the phase transfer of hydrophobic oleic acid coated SPIOs into aqueous solution via liposomal encapsulation, and that the liposomes are enzymatically digested by PLA2, thereby influencing the resultant MPI signal.

4.3 Methods

Fabrication of Nanocarriers

25 nm core size oleic-acid coated SPIOs were purchased from Imagion Biosystems (San Diego, CA). 1,2-dipalmitoyl-sn-glycero-3-phosphocholine (DPPC) and cholesterol were purchased from Avanti Polar Lipids (Alabaster, AL). DPPC, cholesterol and SPIOs were combined at a molar ratio of 50:40 DPPC:cholesterol and 80:20 w/v ratio of lipids:oleic acid in 1 mL dichloromethane (Sigma-Aldrich, St. Louis, MO). These ratios were adapted from Peiris *et al* [101]. Nile Red (Sigma-Aldrich, St. Louis, MO) was also added to the mixture. The

mixture was evaporated via rotary evaporator at room temperature and vacuum. The dry film was hydrated with 1 mL DI water at 60 C to produce liposomes.

In Vitro PLA2-Triggered Nanocarrier Response

Liposomes were treated with Triton X-100 (ThermoFisher Scientific, Waltham, MA) or phopholipase-A2 (PLA2) from porcine pancrease (Sigma-Aldrich, St. Louis, MO). PLA2 was resuspended in 10 mM HEPES buffer with 2 mM $CaCl_2$, pH 7. Calcium is included as PLA2 activity is calcium ion dependent. Measurements of the MPI point-spread-function (PSF) were performed in the UCB arbitrary waveform relaxometer (AWR) [134]. All measurements were taken with a sinusoidal transmit (tx) field frequency of 20.225 kHz, an excitation strength of 40 mTpp. A bias field from -60 mT to 60 mT is applied throughout the scan. The resulting PSF, reconstructed via the x-space algorithm using the data corresponding to the positive slew direction of the tx field, mimics the line profile through the scan of a point source in a 2D or 3D scanner [41]. PSF measurements give the MPI signal strength, measured as the voltage at the peak, and MPI resolution, measured as the full-width-at-half-maximum (FWHM).

4.4 Concept

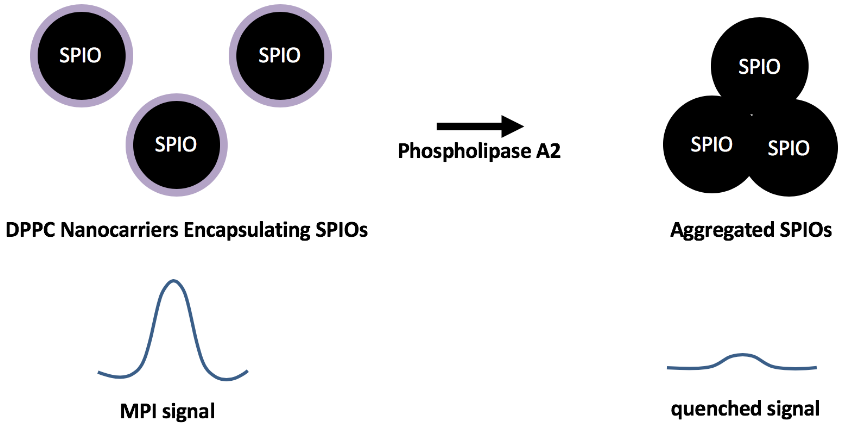

Figure 4.1: **Responsive Nanocarrier Concept.** DPPC micelles or liposomes encapsulating SPIOs exhibit high MPI signal. When phospholipase A2 cleaves DPPC, the hydrophobic SPIOs are released into aqueous media and aggregate, quenching the MPI signal.

The concept is shown in Fig. 4.1. Oleic acid coated nanoparticles can be encapsulated within DPPC, which is an amphiphilic phospholipid with hydrophobic and hydrophilic ends. DPPC can be cleaved by the enzyme phospholipid A2, at which point the the hydrophobic SPIOs are released into the aqueous media and therefore aggregate together. The aggregated nanoparticles will not exhibit the superparamagnetic properties ideal for MPI tracers, and therefore the signal will be quenched.

4.5 Results

SPIO Aggregation Induces SPIO Signal Quenching

As shown in Fig. 4.2, oleic acid SPIOs show a standard MPI PSF in toulene, but show a quenched signal in aqueous solution. Visibly, the solution in toluene was well-dispersed and stable, while the SPIOs appeared to be aggregated at the bottom of the tube in water. The SPIOs in water appear to flip around 17 mT instead of 0 mT, and the FWHM is increased to 24 mT from 12 mT, indicating increased Brownian relaxation of the aggregated particles. This can be intuitively understood as the aggregate takes a longer time to follow the AC excitation magnetic field compared to a singly-dispersed SPIO, resulting in both the lag and lower signal.

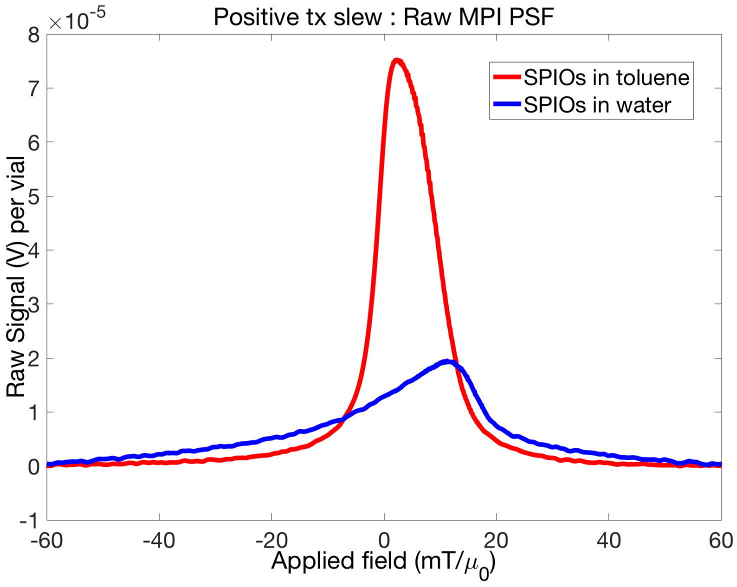

Figure 4.2: **SPIO Signal Quenching.** Oleic acid particles were stable and well-dispersed in toluene, resulting in an expected, high signal MPI PSF as seen on the AWR. In water, the SPIOs aggregated and the signal was quenched significantly.

Nanocarrier Fabrication

The fabrication process is shown in Fig. 4.3 and described earlier in the Methods section. Cholesterol is added to the mixture in order to improve the stability of the liposome [13].

Nile Red is added to the mixture to assess the success of liposomal encapsulation, as the dye is colored in nonpolar media and quenched in aqueous media. Therefore, that the liposomes remain red after hydration in aqueous media indicates successful stable liposome formation.

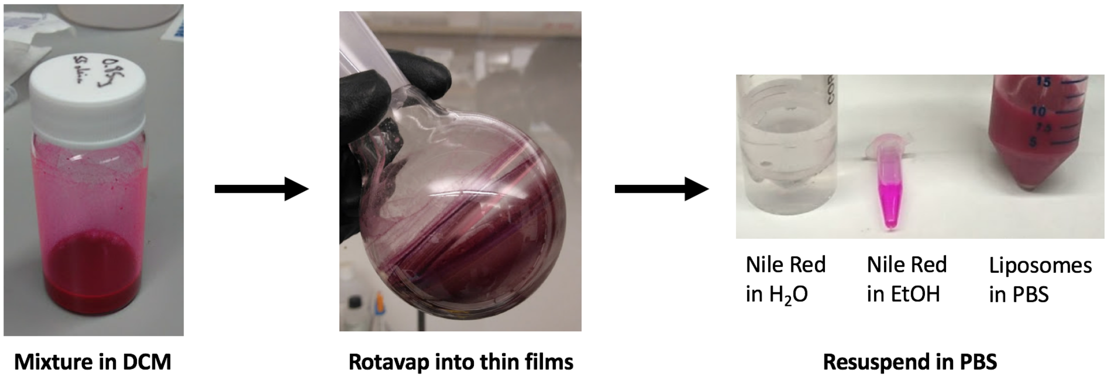

Figure 4.3: **Nanocarrier Fabrication.** (LEFT) DPPC, cholesterol, SPIOs and Nile Red mixture in DCM. (MIDDLE) Nanocarriers in thin films after rotary evaporation. (RIGHT) Liposomes in PBS. Note that Nile Red is colored in nonpolar ethanol but not in polar water. The red color of the liposomes therefore indicates that the Nile Red has been encapsulated into the polar phase.

Nanocarrier Response to PLA2

As shown in the photograph on the right in Fig. 4.4, the presence of PLA2 digests the liposomes into smaller, more compact parts in a dose-dependent manner. In the AWR measurement on the left, the surfactant Triton X disrupts the nanocarrier and results in a lower MPI signal, as expected. However, the PLA2 response is unpredictable; 2 μL of PLA2 resulted in a lower MPI signal, but 1 μL of PLA2 resulted in a higher MPI signal. The maximum MPI signal intensity change is roughly 10%, with a similar FWHM across all samples.

4.6 Conclusion and Discussion

We were able to demonstrate the SPIO aggregation resulted in signal quenching as expected, and that hydrophobic oleic acid coated SPIOs could be encapsulated into nanocarriers and dispersed stably in aqueous solution. However, minimal differences were seen in nanocarriers hydrolyzed with either PLA2 or Triton X compared to control. Compared to single SPIOs stably dispersed in toluene, the PSF of liposomes before and after lysis more closely resembles that of SPIOs aggregated in water (FWHM 24-26 mT). Hence, we suspect that

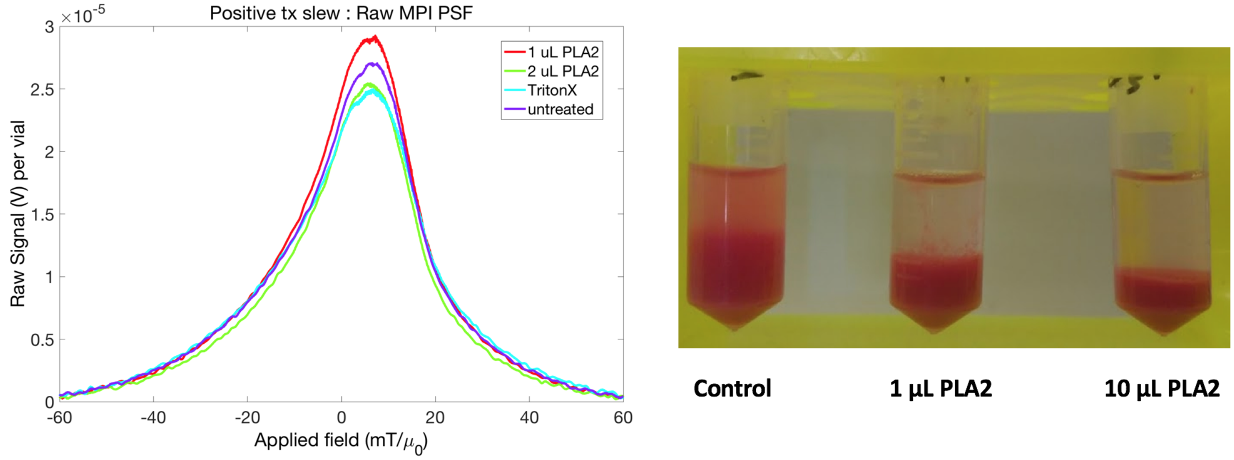

Figure 4.4: **Nanocarrier Response to PLA2.** (LEFT) AWR measurements of liposomes after disruption by TritonX or digestion by PLA2. (RIGHT) Liposomes are digested by PLA2 in a dose-dependent manner.

SPIO aggregates formed during the phase transfer process, significantly quenching the signal before the addition of PLA2 and thereby limiting the achievable contrast.

4.7 Future Work

Alternate fabrication methods, such as those using high-power sonication, may reduce aggregates and thereby allow for responsive SPIO nanocarriers with higher initial MPI signal and hence a more dramatic quenching effect post-enzymatic digestion. This high contrast would also allow translation of these 1D results to a 2D or 3D imaging format.

While we have focused on the potential to build an ON/OFF type biosensor, in some applications it is desirable to be able to track both an "ON" and "OFF" status. For instance, in the cell tracking application discussed in Chapter 3, the location of both living and dead cells are of interest. By generating differences in the shape of the point-spread-function without changing the peak signal, it could be possible to both visualize and distinguish between live and dead cells.

In the traditional sinusoidal MPI scanning and reconstruction regime used above, changes in PSF shape usually occur when a highly Brownian nanoparticle is used and the nanoparticle experiences a more or less viscous medium. In the example of a more viscous medium, the physical rotation of the Brownian particle results in a signal that lags behind the 0 mT point. In Fig. 4.2, we can see that the PSF has both broadened and shifted away from 0 mT. As a result, traditionally there have only been two knobs to turn in order to generate different types of contrast in MPI: signal strength and resolution. Neither is ideal, since in most imaging applications high sensitivity and high resolution is desired. However, we can envision particle behavior in which the PSF peak signal and FWHM is maintained, but different shifts away from 0 mT occur. Recently published techniques, such as pulsed MPI, show that high resolution images can be recovered from shifted data [136].

Future work in this space will combine efforts in nanoparticle synthesis and functionalization with new MPI scanning sequences and reconstruction algorithms, enabling high sensitivity and high resolution MPI imaging with novel contrast modes.

Chapter 5

Conclusion

In this dissertation, I describe the development of several novel applications of magnetic particle imaging (MPI), each of which takes advantage of the unique physics of MPI. First, I demonstrate kidney-safe imaging of the lung capillaries and airways with MPI, which takes advantage of the clearance mechanisms of the SPIO tracer and the MPI gradients, respectively. Next, I demonstrate time course white blood cell tracking with MPI, which takes advantage of the stable signal of the SPIO (as compared to a radionuclide tracer exhibiting radioactive decay). This is particularly important in this application because WBCs take several hours to a day to track to sites of inflammation. Last, I demonstrate proof-of-concept work on an enzyme-responsive nanocarrier towards a MPI tracer that quenches in response to the enzyme phospholipase A2, which is overexpressed in many cancers. Together, these applications highlight the advantages of MPI and cover several main categories of applications development in MPI: vascular imaging, cell tracking, and tracer development. Future work must demonstrate that these proof-of-concept tracers and cell-labeling mechanisms allow for MPI imaging of disease pathologies in relevant mouse and rat models.

Bibliography

[1] Amin Aalipour, Hui-Yen Chuang, Surya Murty, Aloma L. D'Souza, Seung-min Park, Gunsagar S. Gulati, Chirag B. Patel, Corinne Beinat, Federico Simonetta, Ivana Martinić, Gayatri Gowrishankar, Elise R. Robinson, Eamon Aalipour, Zahra Zhian, and Sanjiv S. Gambhir. "Engineered immune cells as highly sensitive cancer diagnostics". In: *Nature Biotechnology* 37.5 (May 2019), pp. 531–539. ISSN: 1087-0156. DOI: 10.1038/s41587-019-0064-8. URL: http://www.nature.com/articles/s41587-019-0064-8.

[2] H Abdel-Nabi, R J Doerr, H W Chan, D Balu, R F Schmelter, and R T Maguire. "In-111-labeled monoclonal antibody immunoscintigraphy in colorectal carcinoma: safety, sensitivity, and preliminary clinical results." In: *Radiology* 175.1 (Apr. 1990), pp. 163–171. ISSN: 0033-8419. DOI: 10.1148/radiology.175.1.2315476. URL: http://pubs.rsna.org/doi/10.1148/radiology.175.1.2315476.

[3] Ammar Abdo and Mesut Sahin. "NIR Light Penetration Depth in the Rat Peripheral Nerve and Brain Cortex". In: *2007 29th Annual International Conference of the IEEE Engineering in Medicine and Biology Society*. IEEE, Aug. 2007, pp. 1723–1725. ISBN: 978-1-4244-0787-3. DOI: 10.1109/IEMBS.2007.4352642. URL: http://ieeexplore.ieee.org/document/4352642/.

[4] Hamed Arami, R M Ferguson, Amit P Khandhar, and Kannan M Krishnan. "Size-dependent ferrohydrodynamic relaxometry of magnetic particle imaging tracers in different environments". en. In: *Med. Phys.* 40.7 (July 2013), p. 071904. ISSN: 0094-2405, 2473-4209. DOI: 10.1118/1.4810962.

[5] Hamed Arami, Eric Teeman, Alyssa Troksa, Haydin Bradshaw, Katayoun Saatchi, Asahi Tomitaka, Sanjiv Sam Gambhir, Urs O Häfeli, Denny Liggitt, and Kannan M Krishnan. "Tomographic magnetic particle imaging of cancer targeted nanoparticles". en. In: *Nanoscale* 9.47 (Dec. 2017), pp. 18723–18730. ISSN: 2040-3364, 2040-3372. DOI: 10.1039/c7nr05502a.

[6] Natsuo Banura and Kenya Murase. "Magnetic particle imaging for aerosol-based magnetic targeting". en. In: *Jpn. J. Appl. Phys.* 56.8 (June 2017), p. 088001. ISSN: 1347-4065. DOI: 10.7567/JJAP.56.088001.

[7] Edwin J R van Beek, Jim M Wild, Christian Fink, Alan R Moody, Hans-Ulrich Kauczor, and Matthijs Oudkerk. "MRI for the diagnosis of pulmonary embolism". en. In: *J. Magn. Reson. Imaging* 18.6 (Dec. 2003), pp. 627–640. ISSN: 1053-1807. DOI: 10.1002/jmri.10421.

[8] Klaas Bente, Matthias Weber, Matthias Graeser, Timo F. Sattel, Marlitt Erbe, and Thorsten M. Buzug. "Electronic Field Free Line Rotation and Relaxation Deconvolution in Magnetic Particle Imaging". In: *IEEE Transactions on Medical Imaging* 34.2 (Feb. 2015), pp. 644–651.

[9] Londa J Berghaus, James N Moore, David J Hurley, Michel L Vandenplas, Barbara P Fortes, Margreet A Wolfert, and Geert-Jan Boons. "Innate immune responses of primary murine macrophage-lineage cells and RAW 264.7 cells to ligands of Toll-like receptors 2, 3, and 4." In: *Comparative immunology, microbiology and infectious diseases* 33.5 (Sept. 2010), pp. 443–54. ISSN: 1878-1667. DOI: 10.1016/j.cimid.2009.07.001. URL: http://www.ncbi.nlm.nih.gov/pubmed/19732955.

[10] D R Biello, A G Mattar, R C McKnight, and B A Siegel. "Ventilation-perfusion studies in suspected pulmonary embolism." In: *AJR. American journal of roentgenology* 133.6 (Dec. 1979), pp. 1033–7.

[11] Challice L Bonifant, Hollie J Jackson, Renier J Brentjens, and Kevin J Curran. "Toxicity and management in CAR T-cell therapy". In: *Molecular Therapy - Oncolytics* 3 (Jan. 2016), p. 16011. ISSN: 2372-7705. DOI: 10.1038/MTO.2016.11. URL: https://www.sciencedirect.com/science/article/pii/S2372770516300353.

[12] Vesna Brglez, Gérard Lambeau, and Toni Petan. "Secreted phospholipases A2 in cancer: Diverse mechanisms of action". In: *Biochimie* 107 (Dec. 2014), pp. 114–123. ISSN: 03009084. DOI: 10.1016/j.biochi.2014.09.023. URL: http://www.ncbi.nlm.nih.gov/pubmed/25286228.

[13] Maria-Lucia Briuglia, Chiara Rotella, Amber McFarlane, and Dimitrios A. Lamprou. "Influence of cholesterol on liposome stability and on in vitro drug release". In: *Drug Delivery and Translational Research* 5.3 (June 2015), pp. 231–242. ISSN: 2190-393X. DOI: 10.1007/s13346-015-0220-8. URL: http://www.ncbi.nlm.nih.gov/pubmed/25787731.

[14] J W M Bulte, P Walczak, M Janowski, K M Krishnan, H Arami, A Halkola, B Gleich, and J Rahmer. "Quantitative "Hot Spot" Imaging of Transplanted Stem Cells using Superparamagnetic Tracers and Magnetic Particle Imaging (MPI)". In: *Tomography* 1.2 (Dec. 2015), pp. 91–97. ISSN: 2379-1381. DOI: 10.18383/j.tom.2015.00172.

[15] Alison G Cahill, Molly J Stout, George A Macones, and Sanjeev Bhalla. "Diagnosing pulmonary embolism in pregnancy using computed-tomographic angiography or ventilation-perfusion". en. In: *Obstet. Gynecol.* 114.1 (July 2009), pp. 124–129.

[16] Hui Cai, Elena G. Chiorean, Michael V. Chiorean, Douglas K. Rex, Bruce W. Robb, Noah M. Hahn, Ziyue Liu, Patrick J. Loehrer, Marietta L. Harrison, and Yan Xu. "Elevated Phospholipase A2 Activities in Plasma Samples from Multiple Cancers". In: *PLoS ONE* 8.2 (Feb. 2013). Ed. by Mohammad O. Hoque, e57081. ISSN: 1932-6203. DOI: 10.1371/journal.pone.0057081. URL: https://dx.plos.org/10.1371/journal.pone.0057081.

[17] Diego Cecchin, Davide Poggiali, Lucia Riccardi, Paolo Turco, Franco Bui, and Stefano De Marchi. "Analytical and experimental FWHM of a gamma camera: theoretical and practical issues". en. In: *PeerJ* 3 (Mar. 2015), e722.

[18] Michael G. Chiorazzo, Hanna Maja Tunset, Anatoliy V. Popov, Berit Johansen, Siver Moestue, and E. James Delikatny. "Detection and Differentiation of Breast Cancer Sub-Types using a cPLA2α Activatable Fluorophore". In: *Scientific Reports* 9.1 (Dec. 2019), p. 6122. ISSN: 2045-2322. DOI: 10.1038/s41598-019-41626-y. URL: http://www.nature.com/articles/s41598-019-41626-y.

[19] Alexander T Cohen, Giancarlo Agnelli, Frederick A Anderson, Juan I Arcelus, David Bergqvist, Josef G Brecht, Ian A Greer, John A Heit, Julia L Hutchinson, Ajay K Kakkar, Dominique Mottier, Emmanuel Oger, Meyer-Michel Samama, Michael Spannagl, and VTE Impact Assessment Group in Europe (VITAE). "Venous thromboembolism (VTE) in Europe. The number of VTE events and associated morbidity and mortality". en. In: *Thromb. Haemost.* 98.4 (Oct. 2007), pp. 756–764.

[20] Jannette Collins and Eric J. Stern. *Chest radiology : the essentials*, p. 413. ISBN: 9781469888569. URL: http://eds.a.ebscohost.com/eds/detail/detail?vid=0%7B%5C&%7Dsid=2b9f72d6-023e-4533-8a97-8d3e2c1191ad%7B%5C%%7D40sessionmgr4008%7B%5C&%7Dbdata=JnNpdGU9ZWRzLWxpdmU%7B%5C%%7D3D.

[21] L. R. Croft, P. W. Goodwill, and S. M. Conolly. "Relaxation in X-Space Magnetic Particle Imaging". In: *IEEE Transactions on Medical Imaging* 31.12 (Dec. 2012), pp. 2335–2342. ISSN: 0278-0062. DOI: 10.1109/TMI.2012.2217979. URL: http://ieeexplore.ieee.org/document/6297476/.

[22] Robert L Duschka, Hanne Wojtczyk, Nikolaos Panagiotopoulos, Julian Haegele, Gael Bringout, Thorsten M Buzug, Joerg Barkhausen, and Florian M Vogt. "Safety measurements for heating of instruments for cardiovascular interventions in magnetic particle imaging (MPI) - first experiences". en. In: *J. Healthc. Eng.* 5.1 (2014), pp. 79–93. ISSN: 2040-2295. DOI: 10.1260/2040-2295.5.1.79.

[23] D Eberbeck, C L Dennis, N F Huls, K L Krycka, C Gruttner, and F Westphal. "Multicore Magnetic Nanoparticles for Magnetic Particle Imaging". In: *IEEE Trans. Magn.* 49.1 (Jan. 2013), pp. 269–274. ISSN: 0018-9464. DOI: 10.1109/TMAG.2012.2226438.

[24] Michel Eisenblätter, Jan Ehrchen, Georg Varga, Cord Sunderkötter, Walter Heindel, Johannes Roth, Christoph Bremer, and Alexander Wall. "In vivo optical imaging of cellular inflammatory response in granuloma formation using fluorescence-labeled macrophages." In: *Journal of nuclear medicine : official publication, Society of Nuclear Medicine* 50.10 (Oct. 2009), pp. 1676–82. ISSN: 1535-5667. DOI: 10.2967/jnumed.108.060707. URL: http://www.ncbi.nlm.nih.gov/pubmed/19759121.

[25] Peter F Fedullo and Victor F Tapson. "The Evaluation of Suspected Pulmonary Embolism". In: *N. Engl. J. Med.* 349.13 (2003), pp. 1247–1256.

[26] R Matthew Ferguson, Amit P Khandhar, Scott J Kemp, Hamed Arami, Emine U Saritas, Laura R Croft, Justin Konkle, Patrick W Goodwill, Aleksi Halkola, Jurgen Rahmer, Jorn Borgert, Steven M Conolly, and Kannan M Krishnan. "Magnetic particle imaging with tailored iron oxide nanoparticle tracers". In: *IEEE Trans. Med. Imaging* 34.5 (May 2015), pp. 1077–1084. ISSN: 0278-0062, 1558-254X. DOI: 10.1109/TMI.2014.2375065.

[27] R Matthew Ferguson, Amit P Khandhar, Scott J Kemp, Hamed Arami, Emine U Saritas, Laura R Croft, Justin Konkle, Patrick W Goodwill, Aleksi Halkola, Jurgen Rahmer, Jorn Borgert, Steven M Conolly, and Kannan M Krishnan. "Magnetic particle imaging with tailored iron oxide nanoparticle tracers". In: *IEEE Trans. Med. Imaging* 34.5 (May 2015), pp. 1077–1084.

[28] R Matthew Ferguson, Amit P Khandhar, and Kannan M Krishnan. "Tracer design for magnetic particle imaging". In: *J. Appl. Phys.* 111.7 (2012), 07B318.

[29] Richard Mathew Ferguson, Amit P Khandhar, Hamed Arami, Loc Hua, Ondrej Hovorka, and Kannan M Krishnan. "Tailoring the magnetic and pharmacokinetic properties of iron oxide magnetic particle imaging tracers." In: *Biomedizinische Technik. Biomedical engineering* 58.6 (Dec. 2013), pp. 493–507. ISSN: 1862-278X. DOI: 10.1515/bmt-2012-0058. URL: http://www.ncbi.nlm.nih.gov/pubmed/23787461.

[30] F Fidler, M Steinke, A Kraupner, C Grüttner, K H Hiller, A Briel, F Westphal, H Walles, and P M Jakob. "Stem Cell Vitality Assessment Using Magnetic Particle Spectroscopy". In: *IEEE Trans. Magn.* 51.2 (Feb. 2015), pp. 1–4. ISSN: 0018-9464. DOI: 10.1109/TMAG.2014.2337052.

[31] Uwe M Fischer, Matthew T Harting, Fernando Jimenez, Werner O Monzon-Posadas, Hasen Xue, Sean I Savitz, Glen a Laine, and Charles S Cox. "Pulmonary passage is a major obstacle for intravenous stem cell delivery: the pulmonary first-pass effect". In: *Stem Cells Dev.* 18.5 (June 2009), pp. 683–692.

[32] Leonard M Freeman and Linda B Haramati. "V/Q scintigraphy: alive, well and equal to the challenge of CT angiography". en. In: *Eur. J. Nucl. Med. Mol. Imaging* 36.3 (Mar. 2009), pp. 499–504.

[33] Sonu Gandhi, Hamed Arami, and Kannan M Krishnan. "Detection of Cancer-Specific Proteases Using Magnetic Relaxation of Peptide-Conjugated Nanoparticles in Biological Environment". en. In: *Nano Lett.* 16.6 (June 2016), pp. 3668–3674. ISSN: 1530-6984, 1530-6992. DOI: 10.1021/acs.nanolett.6b00867.

[34] Benoît Ghaye, Alexandre Ghuysen, Pierre-Julien Bruyere, Vincent D'Orio, and Robert F Dondelinger. "Can CT pulmonary angiography allow assessment of severity and prognosis in patients presenting with pulmonary embolism? What the radiologist needs to know". en. In: *Radiographics* 26.1 (Jan. 2006), 23–39, discussion 39–40.

[35] B Gleich, J Weizenecker, and J Borgert. "Experimental results on fast 2D-encoded magnetic particle imaging". en. In: *Phys. Med. Biol.* 53.6 (21 3 2008), N81–4.

[36] Bernhard Gleich. *Principles and Applications of Magnetic Particle Imaging.* Wiesbaden: Springer Fachmedien Wiesbaden, 2014.

[37] Bernhard Gleich and Jürgen Weizenecker. "Tomographic imaging using the nonlinear response of magnetic particles". en. In: *Nature* 435.7046 (June 2005), pp. 1214–1217. ISSN: 0028-0836, 1476-4687. DOI: 10.1038/nature03808.

[38] E W Goble and J A Abdulkarim. "CT pulmonary angiography using a reduced volume of high-concentration iodinated contrast medium and multiphasic injection to achieve dose reduction". en. In: *Clin. Radiol.* 69.1 (Jan. 2014), pp. 36–40. ISSN: 0009-9260, 1365-229X. DOI: 10.1016/j.crad.2013.07.023.

[39] Forrest Goodfellow, Gregory A Simchick, Luke J Mortensen, Steven L Stice, and Qun Zhao. "Tracking and Quantification of Magnetically Labeled Stem Cells using Magnetic Resonance Imaging." In: *Advanced functional materials* 26.22 (June 2016), pp. 3899–3915. ISSN: 1616-301X. DOI: 10.1002/adfm.201504444. URL: http://www.ncbi.nlm.nih.gov/pubmed/28751853.

[40] Patrick W Goodwill and Steven M Conolly. "Multidimensional x-space magnetic particle imaging". In: *IEEE Trans. Med. Imaging* 30.9 (Sept. 2011), pp. 1581–1590.

[41] Patrick W Goodwill and Steven M Conolly. "The X-space formulation of the magnetic particle imaging process: 1-D signal, resolution, bandwidth, SNR, SAR, and magnetostimulation". en. In: *IEEE Trans. Med. Imaging* 29.11 (Nov. 2010), pp. 1851–1859. ISSN: 0278-0062, 1558-254X. DOI: 10.1109/TMI.2010.2052284.

[42] Patrick W Goodwill, Laura R Croft, and Justin J Konkle. "A 7 T/M 3D X-Space MPI Mouse and Rat Scanner". In: *2013 International Workshop on Magnetic Particle Imaging (IWMPI)* (2013).

[43] Patrick W Goodwill, Justin J Konkle, Bo Zheng, Emine U Saritas, and Steven M Conolly. "Projection x-space magnetic particle imaging". In: *IEEE Trans. Med. Imaging* 31.5 (May 2012), pp. 1076–1085.

[44] Patrick W Goodwill, Emine Ulku Saritas, Laura Rose Croft, Tyson N Kim, Kannan M Krishnan, David V Schaffer, and Steven M Conolly. "X-space MPI: magnetic nanoparticles for safe medical imaging". In: *Adv. Mater.* 24.28 (2012), pp. 3870–3877.

[45] Matthias Graeser, Tobias Knopp, Patryk Szwargulski, Thomas Friedrich, Anselm von Gladiss, Michael Kaul, Kannan M Krishnan, Harald Ittrich, Gerhard Adam, and Thorsten M Buzug. "Towards Picogram Detection of Superparamagnetic Iron-Oxide Particles Using a Gradiometric Receive Coil". en. In: *Sci. Rep.* 7.1 (July 2017), p. 6872. ISSN: 2045-2322. DOI: 10.1038/s41598-017-06992-5.

[46] Mandy Grüttner, Tobias Knopp, Jochen Franke, Michael Heidenreich, Jürgen Rahmer, Aleksi Halkola, Christian Kaethner, Jörn Borgert, and Thorsten M. Buzug. "On the formulation of the image reconstruction problem in magnetic particle imaging". In: *Biomedizinische Technik/Biomedical Engineering* 58.6 (Jan. 2013), pp. 583–91.

[47] Chang Guo, Yangyang Zhang, Yawei Li, Suying Xu, and Leyu Wang. "19F MRI Nanoprobes for the Turn-On Detection of Phospholipase A2 with a Low Background". In: *Analytical Chemistry* (June 2019), acs.analchem.9b00435. ISSN: 0003-2700. DOI: 10.1021/acs.analchem.9b00435. URL: http://pubs.acs.org/doi/10.1021/acs.analchem.9b00435.

[48] Ajay Kumar Gupta and Mona Gupta. "Synthesis and surface engineering of iron oxide nanoparticles for biomedical applications". en. In: *Biomaterials* 26.18 (June 2005), pp. 3995–4021. ISSN: 0142-9612. DOI: 10.1016/j.biomaterials.2004.10.012.

[49] Julian Haegele, Jürgen Rahmer, Bernhard Gleich, Jörn Borgert, Hanne Wojtczyk, Nikolaos Panagiotopoulos, Thorsten M Buzug, Jörg Barkhausen, and Florian M Vogt. "Magnetic particle imaging: visualization of instruments for cardiovascular intervention". en. In: *Radiology* 265.3 (Dec. 2012), pp. 933–938. ISSN: 0033-8419, 1527-1315. DOI: 10.1148/radiol.12120424.

[50] P. V. Harper, K. A. Lathrop, F. Jiminez, R. Fink, and A. Gottschalk. "Technetium 99m as a Scanning Agent". In: *Radiology* 85.1 (July 1965), pp. 101–109. ISSN: 0033-8419. DOI: 10.1148/85.1.101.

[51] Chunbai He, Yiping Hu, Lichen Yin, Cui Tang, and Chunhua Yin. "Effects of particle size and surface charge on cellular uptake and biodistribution of polymeric nanoparticles". In: *Biomaterials* 31.13 (May 2010), pp. 3657–3666. ISSN: 0142-9612. DOI: 10.1016/J.BIOMATERIALS.2010.01.065. URL: https://www.sciencedirect.com/science/article/pii/S0142961210000979.

[52] J A Heit, M D Silverstein, D N Mohr, T M Petterson, W M O'Fallon, and L J Melton 3rd. "Risk factors for deep vein thrombosis and pulmonary embolism: a population-based case-control study". en. In: *Arch. Intern. Med.* 160.6 (27 3 2000), pp. 809–815.

[53] D Hensley, P Goodwill, L Croft, and S Conolly. "Preliminary experimental X-space color MPI". In: *Magnetic Particle Imaging (IWMPI), 2015 5th International Workshop on.* Mar. 2015, pp. 1–1.

[54] Daniel Hensley, Zhi Wei Tay, Rohan Dhavalikar, Bo Zheng, Patrick Goodwill, Carlos Rinaldi, and Steven Conolly. "Combining magnetic particle imaging and magnetic fluid hyperthermia in a theranostic platform". en. In: *Phys. Med. Biol.* 62.9 (May 2017), pp. 3483–3500. ISSN: 0031-9155, 1361-6560. DOI: 10.1088/1361-6560/aa5601.

[55] Friso G Heslinga, Steffen Bruns, Elaine Yu, Paul Keselman, Y Zhou, Bo Zheng, Sebastiaan Waanders, Patrick W Goodwill, M Wendland, Bennie Ten Haken, and Steven M Conolly. *Stem cell tracking potential of Magnetic Particle Imaging compared with 19F Magnetic Resonance Imaging.* Tech. rep. 2016, p. 1. URL: https://ris.utwente.nl/ws/portalfiles/portal/5541042/2016-03-16+IWMPI2016%7B%5C_%7Dabstract+-+Heslinga+et+al.pdf.

[56] Michael Holzinger, Alan Le Goff, and Serge Cosnier. "Nanomaterials for biosensing applications: a review." In: *Frontiers in chemistry* 2 (2014), p. 63. ISSN: 2296-2646. DOI: 10.3389/fchem.2014.00063. URL: http://www.ncbi.nlm.nih.gov/pubmed/25221775.

[57] A P Hunt, M Frier, R A Johnson, S Berezenko, and A C Perkins. "Preparation of Tc-99m-macroaggregated albumin from recombinant human albumin for lung perfusion imaging". In: *Eur. J. Pharm. Biopharm.* 62.1 (Jan. 2006), pp. 26–31.

[58] Hollie J. Jackson, Sarwish Rafiq, and Renier J. Brentjens. "Driving CAR T-cells forward". In: *Nature Reviews Clinical Oncology* 13.6 (June 2016), pp. 370–383. ISSN: 1759-4774. DOI: 10.1038/nrclinonc.2016.36. URL: http://www.nature.com/articles/nrclinonc.2016.36.

[59] Kent Jørgensen, Jesper Davidsen, and Ole G Mouritsen. "Biophysical mechanisms of phospholipase A2 activation and their use in liposome-based drug delivery". In: *FEBS Letters* 531.1 (Oct. 2002), pp. 23–27. ISSN: 0014-5793. DOI: 10.1016/S0014-5793(02)03408-7. URL: https://www.sciencedirect.com/science/article/pii/S0014579302034087.

[60] Jubilant DraxImage Inc. *Kit for the Preparation of Technetium Tc 99m Albumin Aggregated Injection.*

[61] Carl H June, Roddy S O'Connor, Omkar U Kawalekar, Saba Ghassemi, and Michael C Milone. "CAR T cell immunotherapy for human cancer." In: *Science (New York, N.Y.)* 359.6382 (Mar. 2018), pp. 1361–1365. ISSN: 1095-9203. DOI: 10.1126/science.aar6711. URL: http://www.ncbi.nlm.nih.gov/pubmed/29567707.

[62] Paul Keselman, Elaine Yu, Xinyi Y. Zhou, Patrick Goodwill, Matt R. Ferguson, Scott Kemp, Amit P. Khandhar, Kannan Krishnan, Bo Zheng, and Steve Conolly. "Magnetic Particle Imaging as a Tool for Tracking in vivo Biodistribution and Long-term Tracking of Iron Oxide Nanoparticle Tracers and Therapeutics." In: *2016 World Molecular Imaging Congress (WMIC 2016): Imaging Biology... Improving Therapy.* World Molecular Imaging Society (WMIS). 2016.

[63] Paul Keselman, Elaine Yu, Xinyi Zhou, Patrick Goodwill, Prashant Chandrasekharan, R Matthew Ferguson, Amit Khandhar, Scott Kemp, Kannan Krishnan, Bo Zheng, and Steven Conolly. "Tracking short-term biodistribution and long-term clearance of SPIO tracers in magnetic particle imaging". en. In: *Phys. Med. Biol.* 62.9 (Feb. 2017), p. 3440. ISSN: 0031-9155, 1361-6560. DOI: 10.1088/1361-6560/aa5f48.

[64] Katja Kettler, Karin Veltman, Dik van de Meent, Annemarie van Wezel, and A Jan Hendriks. "Cellular uptake of nanoparticles as determined by particle properties, experimental conditions, and cell type". In: *Environ. Toxicol. Chem.* 33.3 (Mar. 2014), pp. 481–492.

[65] Khun Visith Keu, Timothy H Witney, Shahriar Yaghoubi, Jarrett Rosenberg, Anita Kurien, Rachel Magnusson, John Williams, Frezghi Habte, Jamie R Wagner, Stephen Forman, Christine Brown, Martin Allen-Auerbach, Johannes Czernin, Winson Tang, Michael C Jensen, Behnam Badie, and Sanjiv S Gambhir. "Reporter gene imaging of targeted T cell immunotherapy in recurrent glioma." In: *Science translational medicine* 9.373 (Jan. 2017), eaag2196. ISSN: 1946-6242. DOI: 10.1126/scitranslmed.aag2196. URL: http://www.ncbi.nlm.nih.gov/pubmed/28100832.

[66] Amit P Khandhar, R Matthew Ferguson, Hamed Arami, and Kannan M Krishnan. "Monodisperse magnetite nanoparticle tracers for in vivo magnetic particle imaging". en. In: *Biomaterials* 34.15 (May 2013), pp. 3837–3845. ISSN: 0142-9612, 1878-5905. DOI: 10.1016/j.biomaterials.2013.01.087.

[67] Dorien Kiers, Guus P. Leijte, Jelle Gerretsen, Jelle Zwaag, Matthijs Kox, and Peter Pickkers. "Comparison of different lots of endotoxin and evaluation of in vivo potency over time in the experimental human endotoxemia model". In: *Innate Immunity* 25.1 (Jan. 2019), pp. 34–45. ISSN: 1753-4259. DOI: 10.1177/1753425918819754. URL: http://journals.sagepub.com/doi/10.1177/1753425918819754.

[68] Moritz F Kircher, Sanjiv S Gambhir, and Jan Grimm. "Noninvasive cell-tracking methods". In: *Nat. Rev. Clin. Oncol.* 8.11 (Nov. 2011), pp. 677–688. ISSN: 1759-4774.

[69] Sayumi Kobayashi, Akiko Ohki, Minori Tanoue, Yoshimi Inaoka, and Kenya Murase. "Comparative Study of Extracellular and Intracellular Magnetic Hyperthermia Treatments Using Magnetic Particle Imaging". In: *Open Journal of Applied Sciences* 7.12 (2017), p. 647. DOI: 10.4236/ojapps.2017.712047.

[70] Justin J Konkle, Patrick W Goodwill, Emine Ulku Saritas, Bo Zheng, Kuan Lu, and Steven M Conolly. "Twenty-fold acceleration of 3D projection reconstruction MPI". In: *Biomed. Tech.* 58.6 (Dec. 2013), pp. 565–576.

[71] Stavros Konstantinides. "Acute Pulmonary Embolism". In: *N. Engl. J. Med.* 359.26 (2008), pp. 2804–2813.

[72] T Kuboyabu, M Yamawaki, M Aoki, A Ohki, and K Murase. "Quantitative Evaluation of Tumor Early Response to Magnetic Hyperthermia combined with Vascular Disrupting Therapy using Magnetic Particle Imaging". In: *Int J Nanomed Nanosurg* 2.3 (2016), pp. 1–7. ISSN: 2470-3206. DOI: 10.16966/2470-3206.114.

[73] Tomomi Kuboyabu, Isamu Yabata, Marina Aoki, Natsuo Banura, Kohei Nishimoto, Atsushi Mimura, and Kenya Murase. "Magnetic Particle Imaging for Magnetic Hyperthermia Treatment: Visualization and Quantification of the Intratumoral Distribution and Temporal Change of Magnetic Nanoparticles in Vivo". In: *OJMI* 06.01 (2016), pp. 1–15. ISSN: 2164-2788, 2164-2796. DOI: 10.4236/ojmi.2016.61001.

[74] Marina K. Kuimova, Stanley W. Botchway, Anthony W. Parker, Milan Balaz, Hazel A. Collins, Harry L. Anderson, Klaus Suhling, and Peter R. Ogilby. "Imaging intracellular viscosity of a single cell during photoinduced cell death". In: *Nature Chemistry* 1.1 (Apr. 2009), pp. 69–73. ISSN: 1755-4330. DOI: 10.1038/nchem.120. URL: http://www.nature.com/articles/nchem.120.

[75] Adam Kulp and Meta J Kuehn. "Biological functions and biogenesis of secreted bacterial outer membrane vesicles." In: *Annual review of microbiology* 64 (2010), pp. 163–84. ISSN: 1545-3251. DOI: 10.1146/annurev.micro.091208.073413. URL: http://www.ncbi.nlm.nih.gov/pubmed/20825345.

[76] J. Kuruvilla. "The role of autologous and allogeneic stem cell transplantation in the management of indolent B-cell lymphoma". In: *Blood* 127.17 (Apr. 2016), pp. 2093–2100. ISSN: 0006-4971. DOI: 10.1182/blood-2015-11-624320. URL: http://www.ncbi.nlm.nih.gov/pubmed/26989206.

[77] Sophie Laurent, Delphine Forge, Marc Port, Alain Roch, Caroline Robic, Luce Vander Elst, and Robert N. Muller. "Magnetic Iron Oxide Nanoparticles: Synthesis, Stabilization, Vectorization, Physicochemical Characterizations, and Biological Applications". In: *Chemical Reviews* 108.6 (June 2008), pp. 2064–2110. ISSN: 0009-2665. DOI: 10.1021/cr068445e. URL: https://pubs.acs.org/doi/10.1021/cr068445e.

[78] Michel Leblanc and Narinder Paul. "V/Q SPECT and computed tomographic pulmonary angiography". en. In: *Semin. Nucl. Med.* 40.6 (Nov. 2010), pp. 426–441.

[79] Seulki Lee, Jin Xie, and Xiaoyuan Chen. "Activatable molecular probes for cancer imaging." In: *Current topics in medicinal chemistry* 10.11 (2010), pp. 1135–44. ISSN: 1873-4294. URL: http://www.ncbi.nlm.nih.gov/pubmed/20388112.

[80] Jeanne E Lemaster, Fang Chen, Taeho Kim, Ali Hariri, and Jesse V Jokerst. "Development of a Trimodal Contrast Agent for Acoustic and Magnetic Particle Imaging of Stem Cells". In: *ACS Appl. Nano Mater.* 1.3 (Mar. 2018), pp. 1321–1331. DOI: 10.1021/acsanm.8b00063.

[81] Michael Levy, Nathalie Luciani, Damien Alloyeau, Dan Elgrabli, Vanessa Deveaux, Christine Pechoux, Sophie Chat, Guillaume Wang, Nidhi Vats, François Gendron, Cécile Factor, Sophie Lotersztajn, Alain Luciani, Claire Wilhelm, and Florence Gazeau. "Long term in vivo biotransformation of iron oxide nanoparticles". In: *Biomaterials* 32.16 (June 2011), pp. 3988–3999.

[82] S. S. Lewis, G. M. Cox, and J. E. Stout. "Clinical Utility of Indium 111-Labeled White Blood Cell Scintigraphy for Evaluation of Suspected Infection". In: *Open Forum Infectious Diseases* 1.2 (Sept. 2014), ofu089–ofu089. ISSN: 2328-8957. DOI: 10.1093/ofid/ofu089. URL: http://www.ncbi.nlm.nih.gov/pubmed/25734155.

[83] Charito Love, Patrick Opoku-Agyemang, Maria B. Tomas, Paul V. Pugliese, Kuldeep K. Bhargava, and Christopher J. Palestro. "Pulmonary Activity on Labeled Leukocyte Images: Physiologic, Pathologic, and Imaging Correlation". In: *RadioGraphics* 22.6 (Nov. 2002), pp. 1385–1393. ISSN: 0271-5333. DOI: 10.1148/rg.226025038. URL: http://www.ncbi.nlm.nih.gov/pubmed/12432109.

[84] Charito Love and Christopher J. Palestro. "Radionuclide Imaging of Inflammation and Infection in the Acute Care Setting". In: *Seminars in Nuclear Medicine* 43.2 (Mar. 2013), pp. 102–113. ISSN: 0001-2998. DOI: 10.1053/J.SEMNUCLMED.2012.11.003. URL: https://www.sciencedirect.com/science/article/pii/S0001299812001377?via%7B%5C%%7D3Dihub.

[85] Kuan Lu, Patrick W Goodwill, Emine U Saritas, Bo Zheng, and Steven M Conolly. "Linearity and shift invariance for quantitative magnetic particle imaging". In: *IEEE Trans. Med. Imaging* 32.9 (Sept. 2013), pp. 1565–1575.

[86] Min Lu, Martin H Cohen, Dwaine Rieves, and Richard Pazdur. "FDA report: Ferumoxytol for intravenous iron therapy in adult patients with chronic kidney disease". In: *Am. J. Hematol.* 85.5 (May 2010), pp. 315–319.

[87] Peter Ludewig, Nadine Gdaniec, Jan Sedlacik, Nils D Forkert, Patryk Szwargulski, Matthias Graeser, Gerhard Adam, Michael G Kaul, Kannan M Krishnan, R Matthew Ferguson, Amit P Khandhar, Piotr Walczak, Jens Fiehler, Götz Thomalla, Christian Gerloff, Tobias Knopp, and Tim Magnus. "Magnetic Particle Imaging for Real-Time Perfusion Imaging in Acute Stroke". en. In: *ACS Nano* 11.10 (Oct. 2017), pp. 10480–10488. ISSN: 1936-0851, 1936-086X. DOI: 10.1021/acsnano.7b05784.

[88] Ashley V. Makela and Paula J. Foster. "Preclinical 19F MRI cell tracking at 3 Tesla". In: *Magnetic Resonance Materials in Physics, Biology and Medicine* 32.1 (Feb. 2019), pp. 123–132. ISSN: 0968-5243. DOI: 10.1007/s10334-018-0715-7. URL: http://www.ncbi.nlm.nih.gov/pubmed/30421247.

[89] Nafees Malik. "Allogeneic Versus Autologous Stem-Cell Therapy". In: (). URL: http://www.biopharminternational.com/allogeneic-versus-autologous-stem-cell-therapy.

[90] Mallinckrodt Inc. *Kit for the Preparation of Technetium Tc 99m Albumin Aggregated.*

[91] D E Markov, H Boeve, B Gleich, J Borgert, A Antonelli, C Sfara, and M Magnani. "Human erythrocytes as nanoparticle carriers for magnetic particle imaging". en. In: *Phys. Med. Biol.* 55.21 (Nov. 2010), pp. 6461–6473. ISSN: 0031-9155, 1361-6560. DOI: 10.1088/0031-9155/55/21/008.

[92] Robert J. McDonald, Jennifer S. McDonald, David F. Kallmes, Mark E. Jentoft, David L. Murray, Kent R. Thielen, Eric E. Williamson, and Laurence J. Eckel. "Intracranial Gadolinium Deposition after Contrast-enhanced MR Imaging". In: *Radiology* 275.3 (June 2015), pp. 772–782.

[93] Roberta Migale, Bronwen R Herbert, Yun S Lee, Lynne Sykes, Simon N Waddington, Donald Peebles, Henrik Hagberg, Mark R Johnson, Phillip R Bennett, and David A MacIntyre. "Specific Lipopolysaccharide Serotypes Induce Differential Maternal and Neonatal Inflammatory Responses in a Murine Model of Preterm Labor." In: *The American journal of pathology* 185.9 (Sept. 2015), pp. 2390–401. ISSN: 1525-2191. DOI: 10.1016/j.ajpath.2015.05.015. URL: http://www.ncbi.nlm.nih.gov/pubmed/26212908.

[94] Michelle Mujoomdar, Erin Russell, François Dionne, Kristen Moulton, Christine Murray, Sarah McGill, and Kimberlee Lambe. *Detection of Acute Pulmonary Embolism.* Canadian Agency for Drugs and Technologies in Health, 2012.

[95] Patricia K Nguyen, Johannes Riegler, and Joseph C Wu. "Stem cell imaging: from bench to bedside". en. In: *Cell Stem Cell* 14.4 (Apr. 2014), pp. 431–444. ISSN: 1934-5909, 1875-9777. DOI: 10.1016/j.stem.2014.03.009.

[96] Kohei Nishimoto, Atsushi Mimura, Marina Aoki, Natsuo Banura, and Kenya Murase. "Application of Magnetic Particle Imaging to Pulmonary Imaging Using Nebulized Magnetic Nanoparticles". In: *OJMI* 05.02 (2015), pp. 49–55.

[97] Nycomed Inc. *Kit for the Preparation of Technetium Tc 99m Albumin Aggregated.*

[98] Ryan Orendorff, Mihir Patil, Justin J. Konkle, Daniel Hensley, Patrick Goodwill, and Steve Conolly. "Fast x-space MPI DC reconstruction using matrix-free operators with code generation". In: *2016 World Molecular Imaging Congress (WMIC 2016): Imaging Biology... Improving Therapy.* World Molecular Imaging Society (WMIS). 2016.

[99] Ryan Orendorff, Austin J Peck, Bo Zheng, Shawn N Shirazi, R Matthew Ferguson, Amit P Khandhar, Scott J Kemp, Patrick Goodwill, Kannan M Krishnan, George A Brooks, Daniela Kaufer, and Steven Conolly. "First in vivo traumatic brain injury imaging via magnetic particle imaging". en. In: *Phys. Med. Biol.* 62.9 (May 2017), pp. 3501–3509. ISSN: 0031-9155, 1361-6560. DOI: 10.1088/1361-6560/aa52ad.

[100] Nikolaos Panagiotopoulos, Robert L Duschka, Mandy Ahlborg, Gael Bringout, Christina Debbeler, Matthias Graeser, Christian Kaethner, Kerstin Lüdtke-Buzug, Hanne Medimagh, Jan Stelzner, Thorsten M Buzug, Jörg Barkhausen, Florian M Vogt, and Julian Haegele. "Magnetic particle imaging: current developments and future directions". en.

In: *Int. J. Nanomedicine* 10 (Apr. 2015), pp. 3097–3114. ISSN: 1176-9114, 1178-2013. DOI: 10.2147/IJN.S70488.

[101] Pubudu M. Peiris, Lisa Bauer, Randall Toy, Emily Tran, Jenna Pansky, Elizabeth Doolittle, Erik Schmidt, Elliott Hayden, Aaron Mayer, Ruth A. Keri, Mark A. Griswold, and Efstathios Karathanasis. "Enhanced Delivery of Chemotherapy to Tumors Using a Multicomponent Nanochain with Radio-Frequency-Tunable Drug Release". In: *ACS Nano* 6.5 (May 2012), pp. 4157–4168. ISSN: 1936-0851. DOI: 10.1021/nn300652p. URL: http://pubs.acs.org/doi/10.1021/nn300652p.

[102] PerkinElmer and Inc. *VivoTrack 680 Fluorescent Imaging Agent Application note.* Tech. rep. URL: https://www.perkinelmer.com/lab-solutions/resources/docs/APP%7B%5C_%7D010935%7B%5C_%7D01%7B%5C_%7DVivoTrack680.pdf.

[103] Christopher T Petersen, Mojibade Hassan, Anna B Morris, Jasmin Jeffery, Kunhee Lee, Neera Jagirdar, Ashley D Staton, Sunil S Raikar, Harold T Spencer, Todd Sulchek, Christopher R Flowers, and Edmund K Waller. "Improving T-cell expansion and function for adoptive T-cell therapy using ex vivo treatment with PI3Kδ inhibitors and VIP antagonists." In: *Blood advances* 2.3 (2018), pp. 210–223. ISSN: 2473-9537. DOI: 10.1182/bloodadvances.2017011254. URL: http://www.ncbi.nlm.nih.gov/pubmed/29386194.

[104] T L Phillips. "An ultrastructural study of the development of radiation injury in the lung". en. In: *Radiology* 87.1 (July 1966), pp. 49–54.

[105] M A Pysz, S S Gambhir, and J K Willmann. "Molecular imaging: current status and emerging strategies." In: *Clinical radiology* 65.7 (July 2010), pp. 500–16. ISSN: 1365-229X. DOI: 10.1016/j.crad.2010.03.011. URL: http://www.ncbi.nlm.nih.gov/pubmed/20541650%20http://www.pubmedcentral.nih.gov/articlerender.fcgi?artid=PMC3150531.

[106] J Rahmer, A Antonelli, C Sfara, B Tiemann, B Gleich, M Magnani, J Weizenecker, and J Borgert. "Nanoparticle encapsulation in red blood cells enables blood-pool magnetic particle imaging hours after injection". In: *Phys. Med. Biol.* 58.12 (21 2013), pp. 3965–3977.

[107] J. Rahmer, B. Gleich, B. David, C. Bontus, I. Schmale, J. Schmidt, J. Weizenecker, O. Mende, O. Woywode, C. Vollertsen, T. Sattel, J. Gressmann, M. Heinrich, and J. Borgert. "3D line imaging on a clinical magnetic particle imaging demonstrator". In: *2015 5th International Workshop on Magnetic Particle Imaging (IWMPI).* Mar. 2015, pp. 1–1.

[108] J Rahmer, A Halkola, B Gleich, I Schmale, and J Borgert. "First experimental evidence of the feasibility of multi-color magnetic particle imaging". In: *Phys. Med. Biol.* 60.5 (July 2015), pp. 1775–1791.

[109] J. Rahmer, J. Weizenecker, B. Gleich, and J. Borgert. “Analysis of a 3-D System Function Measured for Magnetic Particle Imaging”. In: *IEEE Transactions on Medical Imaging* 31.6 (June 2012), pp. 1289–1299.

[110] Jürgen Rahmer, Jürgen Weizenecker, Bernhard Gleich, and Jörn Borgert. “Signal encoding in magnetic particle imaging: properties of the system function”. en. In: *BMC Med. Imaging* 9 (Apr. 2009), p. 4. ISSN: 1471-2342. DOI: 10.1186/1471-2342-9-4.

[111] Jurgen Rahmer, Daniel Wirtz, Claas Bontus, Jorn Borgert, and Bernhard Gleich. “Interactive Magnetic Catheter Steering With 3-D Real-Time Feedback Using Multi-Color Magnetic Particle Imaging”. en. In: *IEEE Trans. Med. Imaging* 36.7 (July 2017), pp. 1449–1456. ISSN: 0278-0062, 1558-254X. DOI: 10.1109/TMI.2017.2679099.

[112] Peter Reimer and Thomas Balzer. “Ferucarbotran (Resovist): a new clinically approved RES-specific contrast agent for contrast-enhanced MRI of the liver: properties, clinical development, and applications”. en. In: *Eur. Radiol.* 13.6 (June 2003), pp. 1266–1276. ISSN: 0938-7994. DOI: 10.1007/s00330-002-1721-7.

[113] E T Rietschel, T Kirikae, F U Schade, U Mamat, G Schmidt, H Loppnow, A J Ulmer, U Zähringer, U Seydel, and F Di Padova. “Bacterial endotoxin: molecular relationships of structure to activity and function.” In: *The FASEB Journal* 8.2 (Feb. 1994), pp. 217–225. ISSN: 0892-6638. DOI: 10.1096/fasebj.8.2.8119492. URL: http://www.ncbi.nlm.nih.gov/pubmed/8119492.

[114] Paul J Roach, Geoffrey P Schembri, and Dale L Bailey. “V/Q scanning using SPECT and SPECT/CT.” In: *Journal of nuclear medicine* 9 (Sept. 2013), pp. 1588–96. DOI: 10.2967/jnumed.113.124602. URL: https://www.ncbi.nlm.nih.gov/pubmed/23907760.

[115] Matthew D Robson, Peter D Gatehouse, Mark Bydder, and Graeme M Bydder. “Magnetic resonance: an introduction to ultrashort TE (UTE) imaging”. en. In: *J. Comput. Assist. Tomogr.* 27.6 (Nov. 2003), pp. 825–846.

[116] M Rodger and P S Wells. “Diagnosis of pulmonary embolism”. en. In: *Thromb. Res.* 103.6 (15 9 2001), pp. 225–38.

[117] Mohammad M. Sajadi, Wengen Chen, and Vasken Dilsizian. “Targeted Bacteria-Specific 18F-Fluoro-Maltohexaose But Not FDG PET Distinguishes Infection From Inflammation”. In: *JACC: Cardiovascular Imaging* 12.5 (May 2019), pp. 887–889. ISSN: 1936878X. DOI: 10.1016/j.jcmg.2018.03.008. URL: https://linkinghub.elsevier.com/retrieve/pii/S1936878X18302833.

[118] K M Sajid, M Akhtar, I Ahmed, R A Waheed, and F Ahmed. “Local preparation, standardization and quality control of technetium labelled macroaggregated albumin for lung perfusion studies”. en. In: *J. Pak. Med. Assoc.* 41.7 (July 1991), pp. 167–171.

[119] Johannes Salamon, Martin Hofmann, Caroline Jung, Michael Gerhard Kaul, Franziska Werner, Kolja Them, Rudolph Reimer, Peter Nielsen, Annika Vom Scheidt, Gerhard Adam, Tobias Knopp, and Harald Ittrich. “Magnetic Particle / Magnetic Resonance Imaging: In-Vitro MPI-Guided Real Time Catheter Tracking and 4D Angioplasty Using a Road Map and Blood Pool Tracer Approach”. en. In: *PLoS One* 11.6 (June 2016), e0156899. ISSN: 1932-6203. DOI: 10.1371/journal.pone.0156899.

[120] Emine U Saritas, Patrick W Goodwill, Laura R Croft, Justin J Konkle, Kuan Lu, Bo Zheng, and Steven M Conolly. “Magnetic particle imaging (MPI) for NMR and MRI researchers”. In: *J. Magn. Reson.* 229 (Apr. 2013), pp. 116–126. ISSN: 1090-7807, 1096-0856. DOI: 10.1016/j.jmr.2012.11.029.

[121] Lauren Scarfe, Nathalie Brillant, J. Dinesh Kumar, Noura Ali, Ahmed Alrumayh, Mohammed Amali, Stephane Barbellion, Vendula Jones, Marije Niemeijer, Sophie Potdevin, Gautier Roussignol, Anatoly Vaganov, Ivana Barbaric, Michael Barrow, Neal C. Burton, John Connell, Francesco Dazzi, Josefina Edsbagge, Neil S. French, Julie Holder, Claire Hutchinson, David R. Jones, Tammy Kalber, Cerys Lovatt, Mark F. Lythgoe, Sara Patel, P. Stephen Patrick, Jacqueline Piner, Jens Reinhardt, Emanuelle Ricci, James Sidaway, Glyn N. Stacey, Philip J. Starkey Lewis, Gareth Sullivan, Arthur Taylor, Bettina Wilm, Harish Poptani, Patricia Murray, Chris E. P. Goldring, and B. Kevin Park. “Preclinical imaging methods for assessing the safety and efficacy of regenerative medicine therapies”. In: *npj Regenerative Medicine* 2.1 (Dec. 2017), p. 28. ISSN: 2057-3995. DOI: 10.1038/s41536-017-0029-9. URL: http://www.nature.com/articles/s41536-017-0029-9.

[122] Geoffrey P Schembri, Anne E Miller, and Richard Smart. “Radiation dosimetry and safety issues in the investigation of pulmonary embolism”. en. In: *Semin. Nucl. Med.* 40.6 (Nov. 2010), pp. 442–454.

[123] A C Short, M L Montoya, S A Gebb, R G Presson Jr, W W Wagner Jr, and R L Capen. “Pulmonary capillary diameters and recruitment characteristics in subpleural and interior networks”. en. In: *J. Appl. Physiol.* 80.5 (May 1996), pp. 1568–1573.

[124] Alberto Signore. “About inflammation and infection.” In: *EJNMMI research* 3.1 (Feb. 2013), p. 8. ISSN: 2191-219X. DOI: 10.1186/2191-219X-3-8. URL: http://www.ncbi.nlm.nih.gov/pubmed/23374699.

[125] Dmitri Simberg, Ji-Ho Park, Priya P Karmali, Wan-Ming Zhang, Sergei Merkulov, Keith McCrae, Sangeeta N Bhatia, Michael Sailor, and Erkki Ruoslahti. “Differential proteomics analysis of the surface heterogeneity of dextran iron oxide nanoparticles and the implications for their in vivo clearance.” In: *Biomaterials* 30.23-24 (Aug. 2009), pp. 3926–33.

[126] Guosheng Song, Min Chen, Yanrong Zhang, Liyang Cui, Haibo Qu, Xianchuang Zheng, Max Wintermark, Zhuang Liu, and Jianghong Rao. “Janus Iron Oxides @ Semiconducting Polymer Nanoparticle Tracer for Cell Tracking by Magnetic Particle

Imaging". en. In: *Nano Lett.* 18.1 (Jan. 2018), pp. 182–189. ISSN: 1530-6984, 1530-6992. DOI: 10.1021/acs.nanolett.7b03829.

[127] H. Dirk Sostman, Paul D. Stein, Alexander Gottschalk, Fadi Matta, Russell Hull, and Larry Goodman. "Acute Pulmonary Embolism: Sensitivity and Specificity of Ventilation-Perfusion Scintigraphy in PIOPED II Study". In: *Radiology* 246.3 (Mar. 2008), pp. 941–946. ISSN: 0033-8419. DOI: 10.1148/radiol.2463070270.

[128] Mangala Srinivas, Arend Heerschap, Eric T Ahrens, Carl G Figdor, and I Jolanda M de Vries. "(19)F MRI for quantitative in vivo cell tracking." In: *Trends in biotechnology* 28.7 (July 2010), pp. 363–70. ISSN: 1879-3096. DOI: 10.1016/j.tibtech.2010.04.002. URL: http://www.ncbi.nlm.nih.gov/pubmed/20427096.

[129] Paul D Stein, Afzal Beemath, and Ronald E Olson. "Obesity as a risk factor in venous thromboembolism". en. In: *Am. J. Med.* 118.9 (Sept. 2005), pp. 978–980.

[130] Y Takeuchi, H Suzuki, H Sasahara, J Ueda, I Yabata, K Itagaki, S Saito, and K Murase. "Encapsulation of Iron Oxide Nanoparticles into Red Blood Cells as a Potential Contrast Agent for Magnetic Particle Imaging". In: *Advanced Biomedical Engineering* 3 (2014), pp. 37–43. DOI: 10.14326/abe.3.37.

[131] Yukinori Tanaka, Yasuhiro Nagai, Toshinobu Kuroishi, Yasuo Endo, and Shunji Sugawara. "Stimulation of Ly-6G on neutrophils in LPS-primed mice induces platelet-activating factor (PAF)-mediated anaphylaxis-like shock". In: *Journal of Leukocyte Biology* 91.3 (Mar. 2012), pp. 485–494. ISSN: 07415400. DOI: 10.1189/jlb.1210697. URL: http://doi.wiley.com/10.1189/jlb.1210697.

[132] Zhi Wei Tay, Prashant Chandrasekharan, Andreina Chiu-Lam, Daniel W Hensley, Rohan Dhavalikar, Xinyi Y Zhou, Elaine Y Yu, Patrick W Goodwill, Bo Zheng, Carlos Rinaldi, and Steven M Conolly. "Magnetic Particle Imaging-Guided Heating in Vivo Using Gradient Fields for Arbitrary Localization of Magnetic Hyperthermia Therapy". en. In: *ACS Nano* Article ASAP (Mar. 2018). ISSN: 1936-0851, 1936-086X. DOI: 10.1021/acsnano.8b00893.

[133] Zhi Wei Tay, Prashant Chandrasekharan, Xinyi Yedda Zhou, Elaine Yu, Bo Zheng, and Steven Conolly. "In vivo tracking and quantification of inhaled aerosol using magnetic particle imaging towards inhaled therapeutic monitoring." In: *Theranostics* 8.13 (2018), pp. 3676–3687. ISSN: 1838-7640. DOI: 10.7150/thno.26608. URL: http://www.ncbi.nlm.nih.gov/pubmed/30026874.

[134] Zhi Wei Tay, Patrick W Goodwill, Daniel W Hensley, Laura A Taylor, Bo Zheng, and Steven M Conolly. "A High-Throughput, Arbitrary-Waveform, MPI Spectrometer and Relaxometer for Comprehensive Magnetic Particle Optimization and Characterization". en. In: *Sci. Rep.* 6 (Sept. 2016), p. 34180. ISSN: 2045-2322. DOI: 10.1038/srep34180.

[135] Zhi Wei Tay, Daniel W Hensley, Erika C Vreeland, Bo Zheng, and Steven M Conolly. "The relaxation wall: experimental limits to improving MPI spatial resolution by increasing nanoparticle core size". en. In: *Biomed. Phys. Eng. Express* 3.3 (Apr. 2017), p. 035003. ISSN: 2057-1976. DOI: 10.1088/2057-1976/aa6ab6.

[136] Zhi Wei Tay, Daniel Hensley, Jie Ma, Prashant Chandrasekharan, Bo Zheng, Patrick Goodwill, and Steven Conolly. "Pulsed Excitation in Magnetic Particle Imaging". In: *IEEE Transactions on Medical Imaging* (2019), pp. 1–1. ISSN: 0278-0062. DOI: 10.1109/TMI.2019.2898202. URL: https://ieeexplore.ieee.org/document/8638846/.

[137] Kolja Them, J Salamon, P Szwargulski, S Sequeira, M G Kaul, C Lange, H Ittrich, and Tobias Knopp. "Increasing the sensitivity for stem cell monitoring in system-function based magnetic particle imaging". In: *Phys. Med. Biol.* 61.9 (Jan. 2016), pp. 3279–3290.

[138] Marc Thill, Andrzej Kurylcio, Rebekka Welter, Viviana van Haasteren, Britta Grosse, Gilles Berclaz, Wojciech Polkowski, and Nik Hauser. "The Central-European SentiMag study: sentinel lymph node biopsy with superparamagnetic iron oxide (SPIO) vs. radioisotope". en. In: *Breast* 23.2 (Apr. 2014), pp. 175–179. ISSN: 0960-9776, 1532-3080. DOI: 10.1016/j.breast.2014.01.004.

[139] B Taylor Thompson. *Clinical presentation, evaluation, and diagnosis of the adult with suspected acute pulmonary embolism.* Ed. by Ted. W. Post. Waltham, MA: UpToDate, 2016.

[140] Daniel L J Thorek and Andrew Tsourkas. "Size, charge and concentration dependent uptake of iron oxide particles by non-phagocytic cells." In: *Biomaterials* 29.26 (Sept. 2008), pp. 3583–90. ISSN: 0142-9612. DOI: 10.1016/j.biomaterials.2008.05.015. URL: http://www.ncbi.nlm.nih.gov/pubmed/18533252.

[141] Asahi Tomitaka, Hamed Arami, Sonu Gandhi, and Kannan M Krishnan. "Lactoferrin conjugated iron oxide nanoparticles for targeting brain glioma cells in magnetic particle imaging". In: *Nanoscale* 7.40 (Oct. 2015), pp. 16890–16898. ISSN: 2040-3364, 2040-3372. DOI: 10.1039/c5nr02831k.

[142] Asahi Tomitaka, Hamed Arami, Zaohua Huang, Andrea Raymond, Elizette Rodriguez, Yong Cai, Marcelo Febo, Yasushi Takemura, and Madhavan Nair. "Hybrid magneto-plasmonic liposomes for multimodal image-guided and brain-targeted HIV treatment". en. In: *Nanoscale* 10.1 (Dec. 2017), pp. 184–194. ISSN: 2040-3364, 2040-3372. DOI: 10.1039/c7nr07255d.

[143] Mary I Townsley. "Structure and composition of pulmonary arteries, capillaries, and veins". In: *Compr. Physiol.* 2.1 (Jan. 2012), pp. 675–709.

[144] Jen-Chieh Tseng and Andrew L Kung. "In vivo imaging method to distinguish acute and chronic inflammation." In: *Journal of visualized experiments : JoVE* 78 (Aug. 2013). ISSN: 1940-087X. DOI: 10.3791/50690. URL: http://www.ncbi.nlm.nih.gov/pubmed/23978851.

[145] M Utkur, Y Muslu, and E U Saritas. "Relaxation-based viscosity mapping for magnetic particle imaging". In: *Physics in Medicine and Biology* 62.9 (May 2017), pp. 3422–3439. ISSN: 0031-9155. DOI: 10.1088/1361-6560/62/9/3422. URL: http://www.ncbi.nlm.nih.gov/pubmed/28378707%20http://stacks.iop.org/0031-9155/62/i=9/a=3422?key=crossref.6b1f631c9bb3770a1683fc90b748b12c.

[146] M W Verghese and R Snyderman. *Differential anti-inflammatory effects of LPS*. Tech. rep. 2019. URL: http://www.jimmunol.org/content/127/1/288.

[147] Andreas Von Knethen, Alfredo Lotero, and Bernhard Bruè Ne. *Etoposide and cis-platin induced apoptosis in activated RAW 264.7 macrophages is attenuated by cAMP-induced gene expression*. Tech. rep. 1998. URL: http://www.stockton-press.co.uk/onc.

[148] Cuihua Wang, Edmund Keliher, Matthias W G Zeller, Gregory R Wojtkiewicz, Aaron D Aguirre, Leonard Buckbinder, Hye-Yeong Kim, Jianqing Chen, Kevin Maresca, Maaz S Ahmed, Negin Jalali Motlagh, Matthias Nahrendorf, and John W Chen. "An activatable PET imaging radioprobe is a dynamic reporter of myeloperoxidase activity in vivo." In: *Proceedings of the National Academy of Sciences of the United States of America* 116.24 (June 2019), pp. 11966–11971. ISSN: 1091-6490. DOI: 10.1073/pnas.1818434116. URL: http://www.ncbi.nlm.nih.gov/pubmed/31123149.

[149] Ping Wang, Patrick W Goodwill, Prachi Pandit, Jeff Gaudet, Alana Ross, Junfeng Wang, Elaine Yu, Daniel W Hensley, Timothy C Doyle, Christopher H Contag, et al. "Magnetic particle imaging of islet transplantation in the liver and under the kidney capsule in mouse models". In: *Quant. Imaging Med. Surg.* 8.2 (2018), pp. 114–122. ISSN: 2223-4292.

[150] Yi-Xiang J Wang. "Superparamagnetic iron oxide based MRI contrast agents: Current status of clinical application". In: *Quant. Imaging Med. Surg.* 1.1 (Dec. 2011), pp. 35–40. ISSN: 2223-4292, 2223-4306. DOI: 10.3978/j.issn.2223-4292.2011.08.03.

[151] Jason M Warram, Esther de Boer, Anna G Sorace, Thomas K Chung, Hyunki Kim, Rick G Pleijhuis, Gooitzen M van Dam, and Eben L Rosenthal. "Antibody-based imaging strategies for cancer." In: *Cancer metastasis reviews* 33.2-3 (Sept. 2014), pp. 809–22. ISSN: 1573-7233. DOI: 10.1007/s10555-014-9505-5. URL: http://www.ncbi.nlm.nih.gov/pubmed/24913898.

[152] Yuranga Weerakkody and Frank Gaillard. *Osteomyelitis*. URL: https://radiopaedia.org/articles/osteomyelitis?lang=us.

[153] Volkmar Weissig, Tracy K Pettinger, and Nicole Murdock. "Nanopharmaceuticals (part 1): products on the market". en. In: *Int. J. Nanomedicine* 9 (Sept. 2014), pp. 4357–4373. ISSN: 1176-9114, 1178-2013. DOI: 10.2147/IJN.S46900.

[154] J Weizenecker, B Gleich, J Rahmer, H Dahnke, and J Borgert. "Three-dimensional real-time in vivo magnetic particle imaging". en. In: *Phys. Med. Biol.* 54.5 (July 2009), pp. L1–L10.

[155] Elaine Y Yu, Mindy Bishop, Bo Zheng, R Matthew Ferguson, Amit P Khandhar, Scott J Kemp, Kannan M Krishnan, Patrick W Goodwill, and Steven M Conolly. "Magnetic Particle Imaging: A Novel in Vivo Imaging Platform for Cancer Detection". en. In: *Nano Lett.* 17.3 (Feb. 2017), pp. 1648–1654. ISSN: 1530-6984, 1530-6992. DOI: 10.1021/acs.nanolett.6b04865.

[156] Elaine Y Yu, Prashant Chandrasekharan, Ran Berzon, Zhi Wei Tay, Xinyi Y Zhou, Amit P Khandhar, R Matthew Ferguson, Scott J Kemp, Bo Zheng, Patrick W Goodwill, Michael F Wendland, Kannan M Krishnan, Spencer Behr, Jonathan Carter, and Steven M Conolly. "Magnetic Particle Imaging for Highly Sensitive, Quantitative, and Safe in Vivo Gut Bleed Detection in a Murine Model". en. In: *ACS Nano* 11.12 (Dec. 2017), pp. 12067–12076. ISSN: 1936-0851, 1936-086X. DOI: 10.1021/acsnano.7b04844.

[157] Bo Zheng, Marc P von See, Elaine Yu, Beliz Gunel, Kuan Lu, Tandis Vazin, David V Schaffer, Patrick W Goodwill, and Steven M Conolly. "Quantitative Magnetic Particle Imaging Monitors the Transplantation, Biodistribution, and Clearance of Stem Cells In Vivo". en. In: *Theranostics* 6.3 (Jan. 2016), pp. 291–301. ISSN: 1838-7640. DOI: 10.7150/thno.13728.

[158] Bo Zheng, Tandis Vazin, Patrick W Goodwill, Anthony Conway, Aradhana Verma, Emine Ulku Saritas, David Schaffer, and Steven M Conolly. "Magnetic Particle Imaging tracks the long-term fate of in vivo neural cell implants with high image contrast". en. In: *Sci. Rep.* 5 (Sept. 2015), p. 14055. ISSN: 2045-2322. DOI: 10.1038/srep14055.

[159] Xinyi Y Zhou, Kenneth E Jeffris, Elaine Y Yu, Bo Zheng, Patrick W Goodwill, Payam Nahid, and Steven M Conolly. "First in vivo magnetic particle imaging of lung perfusion in rats". en. In: *Phys. Med. Biol.* 62.9 (May 2017), pp. 3510–3522. ISSN: 0031-9155, 1361-6560. DOI: 10.1088/1361-6560/aa616c.

[160] Xinyi Y. Zhou, Zhi Wei Tay, Prashant Chandrasekharan, Elaine Y. Yu, Daniel W. Hensley, Ryan Orendorff, Kenneth E. Jeffris, David Mai, Bo Zheng, Patrick W. Goodwill, and Steven M. Conolly. *Magnetic particle imaging for radiation-free, sensitive and high-contrast vascular imaging and cell tracking.* Aug. 2018. DOI: 10.1016/j.cbpa.2018.04.014.

[161] Harvey A. Ziessman, Janis P. O'Malley, James H. Thrall, and Frederic H. Fahey. *Nuclear medicine : the requisites.* Elsevier Inc., 2013, p. 452. ISBN: 9780323082990. URL: https://jhu.pure.elsevier.com/en/publications/nuclear-medicine-fourth-edition-4.